NASA/TM-2006-214277

Application of the ASP3D Computer Program to Unsteady Aerodynamic and Aeroelastic Analyses

John T. Batina
Langley Research Center, Hampton, Virginia

February 2006

The NASA STI Program Office . . . in Profile

Since its founding, NASA has been dedicated to the advancement of aeronautics and space science. The NASA Scientific and Technical Information (STI) Program Office plays a key part in helping NASA maintain this important role.

The NASA STI Program Office is operated by Langley Research Center, the lead center for NASA's scientific and technical information. The NASA STI Program Office provides access to the NASA STI Database, the largest collection of aeronautical and space science STI in the world. The Program Office is also NASA's institutional mechanism for disseminating the results of its research and development activities. These results are published by NASA in the NASA STI Report Series, which includes the following report types:

- TECHNICAL PUBLICATION. Reports of completed research or a major significant phase of research that present the results of NASA programs and include extensive data or theoretical analysis. Includes compilations of significant scientific and technical data and information deemed to be of continuing reference value. NASA counterpart of peer-reviewed formal professional papers, but having less stringent limitations on manuscript length and extent of graphic presentations.

- TECHNICAL MEMORANDUM. Scientific and technical findings that are preliminary or of specialized interest, e.g., quick release reports, working papers, and bibliographies that contain minimal annotation. Does not contain extensive analysis.

- CONTRACTOR REPORT. Scientific and technical findings by NASA-sponsored contractors and grantees.

- CONFERENCE PUBLICATION. Collected papers from scientific and technical conferences, symposia, seminars, or other meetings sponsored or co-sponsored by NASA.

- SPECIAL PUBLICATION. Scientific, technical, or historical information from NASA programs, projects, and missions, often concerned with subjects having substantial public interest.

- TECHNICAL TRANSLATION. English-language translations of foreign scientific and technical material pertinent to NASA's mission.

Specialized services that complement the STI Program Office's diverse offerings include creating custom thesauri, building customized databases, organizing and publishing research results ... even providing videos.

For more information about the NASA STI Program Office, see the following:

- Access the NASA STI Program Home Page at ***http://www.sti.nasa.gov***

- E-mail your question via the Internet to help@sti.nasa.gov

- Fax your question to the NASA STI Help Desk at (301) 621-0134

- Phone the NASA STI Help Desk at (301) 621-0390

- Write to:
  NASA STI Help Desk
  NASA Center for AeroSpace Information
  7121 Standard Drive
  Hanover, MD 21076-1320

NASA/TM-2006-214277

Application of the ASP3D Computer Program to Unsteady Aerodynamic and Aeroelastic Analyses

John T. Batina
Langley Research Center, Hampton, Virginia

National Aeronautics and
Space Administration

Langley Research Center
Hampton, Virginia 23681-2199

February 2006

Available from:

NASA Center for AeroSpace Information (CASI)
7121 Standard Drive
Hanover, MD 21076-1320
(301) 621-0390

National Technical Information Service (NTIS)
5285 Port Royal Road
Springfield, VA 22161-2171
(703) 605-6000

Application of the ASP3D Computer Program to Unsteady Aerodynamic and Aeroelastic Analyses

John T. Batina[ϕ]
NASA Langley Research Center
Hampton, Virginia 23681

Abstract

A new computer program has been developed called ASP3D (Advanced Small Perturbation – 3D), which solves the small perturbation potential flow equation in an advanced form including mass-consistent surface and trailing wake boundary conditions, and entropy, vorticity, and viscous effects. The purpose of the program is for unsteady aerodynamic and aeroelastic analyses, especially in the nonlinear transonic flight regime. The program exploits the simplicity of stationary Cartesian meshes with the movement or deformation of the configuration under consideration incorporated into the solution algorithm through a planar surface boundary condition. The ASP3D code is the result of a decade of developmental work on improvements to the small perturbation formulation, performed while the author was employed as a Senior Research Scientist in the Configuration Aerodynamics Branch at the NASA Langley Research Center. The ASP3D code is a significant improvement to the state-of-the-art for transonic aeroelastic analyses over the CAP-TSD code (Computational Aeroelasticity Program – Transonic Small Disturbance), which was developed principally by the author in the mid-1980s. The paper presents unsteady aerodynamic and aeroelastic applications of ASP3D to assess the time dependent capability and demonstrate various features of the code. The cases considered include: (1) the NACA 0012 airfoil undergoing a forced harmonic pitching motion about the quarter chord at transonic conditions, (2) a thickening-thinning parabolic arc airfoil at a transonic Mach number, (3) an investigation of wave propagation characteristics with emphasis on high wave number applications, (4) aeroelastic transient calculations for the NACA 0012 airfoil at values of the dynamic pressure below, near, and above the flutter value, and (5) the F-5 fighter wing undergoing a rigid pitching motion about the wing root midchord axis. The results compare well with alternative methods and experimental data, and thus demonstrate the efficiency and utility of the ASP3D code for various unsteady aerodynamic and aeroelastic applications.

Introduction

Over the years research has been conducted by several organizations including the NASA Langley Research Center to assess the general applicability and accuracy of transonic small perturbation (TSP) computer programs in numerous unsteady aerodynamic and aeroelastic applications.[1-4] A notable example of such a computer

---

[ϕ] Retired Research Consultant; Associate Fellow, American Institute of Aeronautics and Astronautics; formerly employed as a Senior Research Scientist, Configuration Aerodynamics Branch, NASA Langley Research Center, Hampton, Virginia.

program is the CAP-TSD code[5] developed by a team of researchers at NASA Langley Research Center in the mid-1980s. The CAP-TSD code solves the transonic small disturbance (TSD) equation with a time-accurate approximate factorization (AF1) algorithm[6,7] and couples the flow equations with the structural equations of motion for simultaneous time integration for aeroelastic analyses. The code exploits the simplicity of stationary Cartesian meshes with the movement or deformation of the configuration under consideration incorporated into the solution algorithm through a planar surface boundary condition. However, applications with the code have revealed various inaccuracies inherent in the underlying small perturbation theory[8] including accuracy limitations near the leading edge and wing tip regions,[1] shock waves that are inaccurately captured in terms of strength or location,[4] and convergence difficulties attributable to certain computational and mathematical complications such as non-uniqueness of the potential flow equation.[9,10] Consequently, the author conducted research over the last decade to examine the applicability of the small perturbation concept in general and the accuracy of the CAP-TSD code in specific. The author is the principal developer[6,7,11,12] of the CAP-TSD code and is therefore in a unique position to make a critical assessment of the methodology contained therein. The objective of the effort was to identify the sources of the inaccuracies and determine if improvements could be made to alleviate or eliminate them.

Subsequently, a new advanced small perturbation (ASP) potential flow theory[13] was developed by methodically determining the essential elements required to produce accurate solutions with the small perturbation approach on a Cartesian grid. The ASP theory involves a higher-order streamwise flux in the governing equation, mass-consistent surface boundary conditions for flow tangency, mass-conserving entropy and vorticity effects including second-order terms in the trailing wake boundary condition, and viscous effects modeled using integral boundary layer equations[14,15] solved simultaneously with the governing small perturbation potential flow equation with turbulent closure given by the dissipation integral relations of Drela.[16] The ASP theory was shown to be mathematically more appropriate and computationally more accurate than the classical TSP theories.[13] Therefore, the ASP theory was used as the basis for a new computer program called ASP3D[17] (Advanced Small Perturbation – 3D), which involves either AF1- or AF2-type approximate factorization algorithms and a FAS (full approximation scheme) multigrid procedure for the solution of the ASP potential flow equation and associated boundary conditions. The purpose of the program is for unsteady aerodynamic and aeroelastic analyses, especially in the nonlinear transonic flight regime. The ASP3D code can treat aircraft configurations involving multiple lifting surfaces with leading and trailing edge control surfaces and a fuselage. Steady-state aerodynamic results obtained using the ASP3D code were presented by Batina,[17] thus demonstrating various options and the general utility of the new program. Comparisons were made with alternative calculations and experimental data to demonstrate the accuracy of the ASP approach for steady-state applications. The purpose of the present paper, though, is to present unsteady aerodynamic and aeroelastic applications obtained using the ASP3D code. Several cases were considered to assess the time-dependent capability and demonstrate additional features of ASP3D. Comparisons are made with alternative calculations and experimental data to evaluate the accuracy and utility of the code.

Overview of the ASP3D Program

The ASP3D[17] code was developed over the last decade by the author during his employment as a Senior Research Scientist within the Configuration Aerodynamics Branch at NASA Langley Research Center. The development of the code resulted from a research study to determine the specific causes of the inaccuracies and inefficiencies inherent to CAP-TSD. That work revealed that the underlying small perturbation potential flow theory in CAP-TSD was deficient in several respects. An advanced small perturbation theory[13] was developed to alleviate or eliminate the inaccuracies identified in CAP-TSD. The ASP theory was shown subsequently to be mathematically more appropriate and computationally more accurate than the classical TSP theories such as that embodied within CAP-TSD. Consequently, the ASP theory was used as the basis for the new ASP3D program, which in contrast with CAP-TSD involves modern computational fluid dynamics concepts such as a finite volume spatial discretization, sharper shock capture, dissipation integral boundary layer modeling, alternative AF2-type approximate factorization algorithm, and FAS (full approximation scheme) multigrid solution convergence acceleration.

The ASP3D Computer Program

The ASP3D computer program involves either AF1- or AF2-type approximate factorization algorithms and a FAS multigrid procedure for the solution of the advance small perturbation potential flow equation and associated boundary conditions. The ASP3D code can treat aircraft configurations involving multiple lifting surfaces with leading and trailing edge control surfaces, and a fuselage. The new code is described briefly here along with relevant equations. The interested reader is referred to References 13 and 17 for further details of the program.

- **Governing Equation**

The three-dimensional general small perturbation equation may be written in Cartesian coordinates as

$$\frac{\partial f_0}{\partial t} + \frac{\partial f_1}{\partial x} + \frac{\partial f_2}{\partial y} + \frac{\partial f_3}{\partial z} = 0$$

where the Cartesian fluxes are defined as

$$f_0 = -A\phi_t - B\phi_x$$

$$f_1 = C + D\phi_x + E\phi_x^2 + F\phi_x^3 + G\phi_y^2 + \frac{H}{2}\phi_x\phi_y^2$$

$$f_2 = \left(1 + H\phi_x + \frac{H}{2}\phi_x^2\right)\phi_y + F\phi_y^3$$

$$f_3 = \phi_z$$

with the constants defined as

$$A = M_\infty^2 \qquad B = 2M_\infty^2 \qquad C = 1 \qquad D = 1 - M_\infty^2$$

$$E = -\frac{1}{2}(\gamma+1)M_\infty^2 \qquad F = -\frac{1}{6}(\gamma+1)M_\infty^2 \qquad G = \frac{1}{2}(\gamma-3)M_\infty^2 \qquad H = -(\gamma-1)M_\infty^2$$

The ASP3D code though solves the governing equation written in computational coordinates as

$$\frac{\partial \hat{f}_0}{\partial t} + \frac{\partial \hat{f}_1}{\partial \xi} + \frac{\partial \hat{f}_2}{\partial \eta} + \frac{\partial \hat{f}_3}{\partial \zeta} = 0$$

where the computational fluxes are defined as

$$\hat{f}_0 = -\frac{A}{J}\phi_t - \frac{B}{J}\xi_x \phi_\xi$$

$$\hat{f}_1 = \frac{|\nabla \xi|}{J}\left[\frac{\xi_x}{|\nabla \xi|}(f_1) + \frac{\xi_y}{|\nabla \xi|}(f_2)\right]$$

$$\hat{f}_2 = \frac{|\nabla \eta|}{J}\left[\frac{\eta_y}{|\nabla \eta|}(f_2)\right]$$

$$\hat{f}_3 = \frac{|\nabla \zeta|}{J}\left[\frac{\zeta_z}{|\nabla \zeta|}(f_3)\right]$$

The various geometric quantities used in these equations are computed using the exact formulas given by Batina.[17]

- **Entropy and Vorticity Effects**

Shock-generated entropy effects are incorporated within small perturbation codes such as CAP-TSD by first using the Prandtl relation[18] (shock jump condition) to determine the velocity downstream of the shock wave from the upstream and sonic velocities. The upstream and downstream velocities are then used in the Rankine-Hugoniot shock relation[18] to determine the change in entropy across the shock wave.[19] The resulting change in entropy is subsequently used in a Clebsch formulation[20] to determine the vorticity downstream of the shock wave.[21,22] The vorticity modifies the calculation of the velocity field in the downstream region. This is a common procedure that has been used in various computer codes especially at the full-potential equation level. However, the approach as applied to the small perturbation equation, with any of the available definitions for the streamwise mass flux f_1 including that of Williams,[23] does not conserve mass.

In contrast, the approach developed for the ASP3D program conserves mass by using a ratio of the streamwise flux evaluated using the upstream and downstream velocities. Specifically, the downstream perturbation velocity is first computed using the Prandtl relation (shock jump relation) given by

$$(\phi_x)_2 = \frac{\left[1+(\phi_x)_{sonic}\right]^2}{1+(\phi_x)_1} - 1$$

where the subscripts 1 and 2 represent stations that are upstream and downstream of the shock wave, respectively. The change in entropy across the shock is then computed using

$$\Delta s = (\gamma-1)\left\{1 - f_1\left[(\phi_x)_1\right] / f_1\left[(\phi_x)_2\right]\right\}$$

For steady flows the entropy is held constant along gridlines downstream of shock waves. For unsteady flows the entropy is convected downstream using

$$\frac{\partial}{\partial t}\Delta s + \frac{\partial}{\partial x}\Delta s = 0$$

The fluxes downstream of the shock are subsequently modified according to

$$(f_1)_{nonisentropic} = \left[1 - \frac{\Delta s}{(\gamma-1)}\right](f_1)_{isentropic}$$

which conserves mass across the shock wave by design.

The ASP3D code uses a Clebsch formulation[20] to compute the shock-generated vorticity. In brief, the streamwise velocities downstream of shocks are computed using

$$(\phi_x)_{rotational} = (\phi_x)_{irrotational} - \frac{\Delta s}{\gamma(\gamma-1)M_\infty^2}$$

Also, the second-order terms in the trailing wake boundary condition were found to be not insignificant, and thus, they were incorporated into the ASP3D solution procedure.[17]

- **Viscous Effects**

The ASP3D viscous method involves solving the unsteady boundary layer equations simultaneously with the outer potential flow solution so that no interaction law coupling the inner and outer solutions is required. The combined solution procedure involves an implicit block tridiagonal inversion for all of the cells along the surface and trailing wake. Unlike the CAP-TSD viscous capability,[24-26] the ASP capability uses exact formulas for edge quantities and exact boundary conditions along surfaces and wakes. Smoothing of

edge quantities and limiters are not required for stability, and no arbitrary or free parameters are necessary to tune the procedure.

Specifically in the ASP3D viscous capability, the exact edge quantities are used for the calculation of velocity u_e, density ρ_e, temperature T_e, local Mach number M_e, and the coefficient of viscosity μ_e defined by

$$u_e = 1 + \phi_x$$

$$\rho_e = \left[1 - \frac{\gamma - 1}{2} M_\infty^2 \left(2\phi_x + \phi_x^2 \right) \right]^{\frac{1}{\gamma - 1}}$$

$$T_e = \left[1 - \frac{\gamma - 1}{2} M_\infty^2 \left(2\phi_x + \phi_x^2 \right) \right]$$

$$M_e = \frac{M_\infty (1 + \phi_x)}{\left[1 - \frac{\gamma - 1}{2} M_\infty^2 \left(2\phi_x + \phi_x^2 \right) \right]^{1/2}}$$

$$\mu_e = (T_e)^{3/2} \frac{1 + (S/T_\infty)}{(T_e) + (S/T_\infty)}$$

where S is Sutherland's coefficient and T_∞ is the freestream temperature.

For the ASP3D capability, the time-dependent integral boundary layer (IBL) and lag equations may be written as a system of equations in the form

$$[A] \frac{\partial}{\partial t} \begin{Bmatrix} \theta \\ H_k \\ c_\tau^{1/2} \end{Bmatrix} + [B] \frac{\partial}{\partial x} \begin{Bmatrix} \theta \\ H_k \\ c_\tau^{1/2} \end{Bmatrix} + [C] \begin{Bmatrix} \phi_{xx} \\ \phi_{xt} \\ \phi_{tt} \end{Bmatrix} + \{S\} = \{0\}$$

where the independent variables are the momentum thickness θ, the incompressible shape parameter H_k, and the square root of the shear stress coefficient c_τ.

For solution, the integral boundary layer and lag equations are first premultiplied by $[A]^{-1}$ to diagonalize the time term as

$$\frac{\partial}{\partial t} \begin{Bmatrix} \theta \\ H_k \\ c_\tau^{1/2} \end{Bmatrix} + [D] \frac{\partial}{\partial x} \begin{Bmatrix} \theta \\ H_k \\ c_\tau^{1/2} \end{Bmatrix} + [E] \begin{Bmatrix} \phi_{xx} \\ \phi_{xt} \\ \phi_{tt} \end{Bmatrix} + \{F\} = \{0\}$$

The resulting IBL system is then linearized in a simple way and cast into the so-called delta-form for implicit solution as

$$\Delta x \begin{Bmatrix} \Delta\theta \\ \Delta H_k \\ \Delta c_\tau^{1/2} \end{Bmatrix} + \Delta t [G] \begin{Bmatrix} \Delta\theta \\ \Delta H_k \\ \Delta c_\tau^{1/2} \end{Bmatrix} = -\Delta x \Delta t \{R\}$$

where the viscous residual is defined as

$$\{R\} = [D] \frac{\partial}{\partial x} \begin{Bmatrix} \theta \\ H_k \\ c_\tau^{1/2} \end{Bmatrix} + [E] \begin{Bmatrix} \phi_{xx} \\ \phi_{xt} \\ \phi_{tt} \end{Bmatrix} + \{F\}$$

The system of equations is directly coupled with the ASP equation for the outer potential flow for simultaneous implicit solution using a block tridiagonal matrix inversion procedure. This is done only for the cells adjacent to the upper and lower sides of the lifting surfaces and their wakes where the boundary layer is located. All other cells do not involve the boundary layer, and hence, only the ASP equation is solved in those cells. Dissipation integral relations are used for turbulent closure, similar to those reported by Drela.[16]

- **Surface Boundary Condition**

In ASP3D the complete mass-consistent surface boundary condition including entropy, vorticity, and viscous effects is given by

$$\phi_z = \frac{f}{g}(b_x - \alpha) + \phi_y b_y \pm \frac{1}{g}\left(f\delta^*\right)_x + b_t + \delta_t^*$$

where

$$f = C + D(\phi_x)_{rotational} + E\left(\phi_x^2\right)_{rotational} + F\left(\phi_x^3\right)_{rotational}$$
$$-A\phi_y^2 + \frac{H}{2}\phi_y^2(\phi_x)_{rotational}$$

and

$$g = 1 + H\left(\phi_x\right)_{rotational} + \frac{H}{2}\left(\phi_x^2\right)_{rotational} + \frac{H}{2}\left(\phi_y^2\right)$$

The surface is represented by

$$b(x,y,t) \pm \delta^*(x,t) - x\alpha = 0$$

where the ± is for the upper and lower surfaces, respectively, since the boundary layer displacement thickness δ^* is defined as a positive quantity on both surfaces.

Note that the spanwise slopes b_y are included in the complete surface boundary condition for three-dimensional applications, which may be important for swept wings near the leading edge and also in the wing tip region. Furthermore, the streamwise and spanwise slopes are computed internal to ASP3D from the ordinates of the wing geometry by simple second-order accurate central finite differences, effectively the same as is done in advanced codes with body fitted meshes. This eliminates the differentiation of the spline of the wing geometry normally performed as a preprocessing step to determine the airfoil slopes. It thus makes the input to the ASP3D code simpler than most other small perturbation codes such as CAP-TSD.

- **Wake Boundary Condition**

Viscous effects are included in the wake modeling in ASP3D through the boundary condition

$$\Delta\phi_z = \pm\frac{1}{g}\left(f\delta^*\right)_x + \delta_t^*$$

across the wake where f and g were defined previously. The boundary condition is incorporated numerically using

$$\left(\phi_z\right)_{upper} = \frac{\phi_k - \left(\phi_{k-1} + \Gamma\right)}{z_k - z_{k-1}} + \frac{1}{2}\left[\frac{1}{g}\left(f\delta^*\right)_x + \delta_t^*\right]$$

and

$$\left(\phi_z\right)_{lower} = \frac{\left(\phi_k - \Gamma\right) - \phi_{k-1}}{z_k - z_{k-1}} - \frac{1}{2}\left[\frac{1}{g}\left(f\delta^*\right)_x + \delta_t^*\right]$$

- **Shock Capturing**

The AF1 and AF2 algorithms of the ASP3D code use one of three approaches to model supersonic regions of the flow including: (1) Godunov,[27] (2) Engquist-Osher[28] (E-O), and (3) Murman-Cole[29] (M-C) type-dependent switches. The first two switches satisfy an entropy inequality by design. This means that their use precludes the possibility of computing nonphysical expansion shocks that can occur with the Murman-Cole switch, especially in two-dimensional applications. With Godunov[27] switching, shocks are captured sharply, usually with only one interior state. Therefore, the Godunov switch is preferable over the E-O and M-C switches, and it is the default switch within the ASP3D code.

- **Solution Algorithm**

The ASP3D code involves a modern cell-centered finite-volume discretization, which allows exact planform treatment including leading edges, wing tips, and control surface edges. The advanced small perturbation equation is solved numerically using either an AF1 approximate factorization algorithm or an AF2-type[30] algorithm. The AF1

algorithm within the ASP3D code is the cell-centered finite-volume version of the AF1 algorithm developed for CAP-TSD, which is described by Batina.[7] However, the AF1 algorithm is susceptible to the so-called moving shock instability[30] if shock waves move more than one cell per time step.

The AF2 algorithm within the ASP3D code is described in general by

$$L_\zeta L_\eta L_\xi \Delta\phi = -R(\phi)$$

The general form of the AF2 algorithm appears to be similar to that of the AF1 algorithm but there are two fundamental differences. First, the operators are applied in the reverse order (here, vertical and spanwise sweeps are performed first, with the streamwise sweep performed last) and a streamwise implicit temporal damping term is included on the right hand side of the equation to eliminate the occurrence of the moving shock instability. The AF2 algorithm is defined specifically by

$$\left[\left(\frac{\overline{\alpha}}{J}\right) - \delta_\zeta \hat{g}_3 \delta_\zeta\right]\Delta\overline{\phi}_i = -\omega R + \frac{1}{J}\left(\frac{\xi_x}{\Delta\tau} + \psi\frac{3\xi_x}{2\Delta t}B\right)\Delta\overline{\overline{\phi}}_{i-1}$$

$$\left[\left(\frac{\overline{\alpha}}{J}\right) - \delta_\eta \hat{g}_2 \delta_\eta\right]\Delta\overline{\overline{\phi}}_i = \left(\frac{\overline{\alpha}}{J}\right)\Delta\overline{\phi}_i$$

$$\left[\left(\frac{\overline{\alpha}}{J}\right) - (\hat{g}_1)_{i+1/2}\vec{\delta}_\xi\right]\Delta\phi_i = \left(\frac{\overline{\alpha}}{J}\right)\Delta\overline{\overline{\phi}}_i$$

where the flux Jacobians are defined by Batina.[17] Although not obvious, the temporal damping term is treated implicitly since it involves information from the second intermediate sweep but at the previous grid plane *i* - 1, and

$$\overline{\alpha} = \frac{\xi_x}{\Delta\tau} + \psi\left(\frac{2}{\Delta t^2}A + \frac{3\xi_x}{2\Delta t}B\right)$$

The parameter ψ is set equal to zero for steady applications and set equal to unity for unsteady applications. The parameter ω is an over-relaxation factor. The AF2 algorithm involves both physical (Δt) and computational ($\Delta\tau$) time steps. The computational step is selected for rapid convergence and it is usually assigned a large value. Hence the solution can be advanced using either a constant computational time step or a constant CFL number (variable time step). The physical time step is used only for unsteady applications, and it is selected based on the physics of the problem being considered.

The AF2 approach is the preferred algorithm. The AF2 scheme is more robust than the AF1 scheme since it cannot fail due to the moving shock instability by design, because the temporal damping term eliminates the instability. Hence convergence to steady state is achieved with large time steps or large CFL numbers, independent of the

moving shock instability that plagues the AF1 algorithm. The AF2 scheme also may be used for unsteady calculations when local iteration is applied. Therefore, the physical time step may be selected based on the physics of the problem being solved, rather than on numerical stability considerations. In either steady or unsteady applications, the temporal damping term vanishes in the steady-state limit or within the convergence process of performing subiterations (for unsteady calculations).

- **Multigrid Implementation**

The AF1 algorithm is not appropriate for multigrid implementation because the rapid rate of convergence of the multigrid procedure would result in the moving shock instability. The AF2 algorithm of the ASP3D code is amenable to multigrid implementation because the temporal damping term prevents the moving shock instability from occurring. Therefore the multigrid procedure[31] may be used for steady or iterative unsteady applications with ASP3D. The procedure is implemented in FAS (full approximation scheme) form,[32] which is applicable to nonlinear governing equations. As with any multigrid procedure, high-frequency errors are damped on the fine mesh and low-frequency errors are damped on the coarser meshes. Either V- or W-cycles may be selected and full multigrid is available. W-cycles have been found to be slightly more effective for solution convergence, although W-cycles are slightly more expensive than V-cycles.[33]

Specifically, the calculation on the finest mesh (N) smoothes high frequency errors using the AF2 algorithm written in general form

$$L_N(\phi_N) = R_N$$

Subsequent calculations on the next coarser mesh (N-1) involve fine mesh residual injection

$$L_{N-1}(\phi_{N-1}) = R_{N-1} - \hat{I}_N^{N-1}(R_N) + L_{N-1} I_N^{N-1}(\phi_N)$$

where the I functions are restriction operators for transferring the velocity potential and residual from the fine mesh to the coarse mesh. The procedure is generally repeated for additional coarse meshes (N-2, N-3, …).

The restriction operator[33] for the velocity potential is a volume-weighted operator defined by

$$\phi_{N-1} = I_N^{N-1}\phi_N = \frac{\sum V\phi_N}{\sum V}$$

and the restriction operator[33] for residuals is defined by

$$\hat{I}_N^{N-1} R_N = \sum R_N$$

where the summations above are taken over all of the fine mesh cells that make up the coarse mesh cell. The interpolation operator for the velocity potential that is required to

transfer information back from coarse to fine mesh is a trilinear interpolation operator defined symbolically by

$$\phi_N \leftarrow \phi_N + I_{N-1}^{N}\phi_{N-1}$$

- **Numerical Accuracy**

In the ASP3D code geometric quantities such as areas, volumes, and direction cosines are computed using exact formulas.[17] The velocity components are computed using similar formulas as used in CAP-TSD, but in ASP3D, they are exact for a linear test function on a general grid. Generally speaking, the ASP3D algorithm is second-order-accurate within subsonic cells and first-order accurate within supersonic cells, although a second-order-accurate supersonic capability is available as a user-selected option.

Also in CAP-TSD the ϕ_{xt} term in the governing equation is computed using first-order-accurate backward differencing for stability reasons. However, for unsteady applications at higher reduced frequencies encountered with control surfaces or higher wave number phenomena such as Kutta waves, this differencing may be too dispersive. In contrast, first-, second-, and third-order-accurate backward differencing operators are available for the ϕ_{xt} term in ASP3D as user-selected options to improve the accuracy for such applications.

- **Structural Equations of Motion**

Similar to the CAP-TSD code, the flow equations of ASP3D are coupled with the structural equations of motion for simultaneous time-integration for aeroelastic analysis. Specifically, such analysis involves the coupling of the aerodynamics with the structural characteristics of the configuration under consideration.[2] The resulting equations of motion for a time domain or time-marching aeroelastic solution are based on the aircraft natural vibration modes. These equations are integrated in time along with the finite volume solution of the flow field in ASP3D. Initial conditions for each structural mode are specified and free decay transients are computed. Initial velocities in one or more modes, rather than displacements, have been found to be superior in avoiding nonphysical, strictly numerical transients and their possibly associated instabilities. Aeroelastic stability is then deduced from the free decay records or time histories. This is a fairly standard procedure for aeroelastic analyses with the small perturbation computer codes, and thus, the interested reader is referred to Cunningham, et al.[2] or Bennett, et al.[3] for further details including equations and representative calculations.

Results and Discussion

Results computed using the ASP3D computer program are presented for several unsteady aerodynamic and aeroelastic cases to assess the time-dependent capability and demonstrate various features of the code. The cases considered include: (1) the NACA 0012 airfoil undergoing a forced harmonic pitching motion about the quarter chord at

transonic conditions,[34] (2) a thickening-thinning parabolic arc airfoil at a transonic Mach number,[35] (3) an investigation of wave propagation characteristics with emphasis on high wave number applications,[36,37] (4) aeroelastic transient calculations for the NACA 0012 airfoil at values of the dynamic pressure below, near, and above the flutter value,[38,39] and (5) the F-5 fighter wing undergoing a rigid pitching motion about the wing root mid-chord axis.[40] All of the calculations are inviscid applications of the code, in part, because the viscous capability was not implemented at the time.

Flow calculations for the two-dimensional cases were performed using a 193 x 129 Cartesian finite volume mesh as shown in Figure 1. The total mesh is shown in Figure 1(a) and a near field view is shown in Figure 1(b). The mesh had a twenty chord extent from the airfoil in both the *x*- and *z*-directions with a spacing at the leading and trailing edges of $\Delta x = 0.015c$. There is only one cell in the spanwise direction for airfoil applications, which effectively produces a two-dimensional solution. Multigrid calculations were performed using this mesh (termed Mesh 5) and four subsets of the mesh (Meshes 1 through 4) determined by simply deleting every other grid line. The coarser meshes contain 97 x 65 (Mesh 4), 49 x 33 (Mesh 3), 25 x 17 (Mesh 2), and 13 x 9 (Mesh 1) points in the x- and z-directions, respectively. This is done automatically within the ASP3D code and thus is not something that the user needs to do during mesh generation. Flow calculations for the F-5 fighter wing were performed using a 97 x 25 x 65 finite volume mesh as discussed below.

- **NACA 0012 Airfoil Harmonic Pitching Results**

The first case considered is that of the NACA 0012 airfoil at a mean angle of attack of $\alpha_0 = 0.016°$ and a freestream Mach number of $M_\infty = 0.755$.[34] The airfoil was forced to pitch harmonically about the quarter chord with an amplitude of $\alpha_1 = 2.51°$ at a reduced frequency based on semichord of $k = 0.0814$. This is a well-studied nonlinear unsteady transonic case[34] that involves moving shock waves on both the upper and lower surfaces of the airfoil produced by the relatively large amplitude of motion. The shock waves move approximately twenty-five percent chord and periodically appear and disappear during a cycle of motion. The case was chosen to demonstrate the superior numerical stability of the iterative multigrid capability of the ASP3D code for unsteady applications, whereby the computational time step is selected to be very large for rapid convergence and the physical time step is selected based on the physics of the problem (temporal accuracy). In fact the physical step size can be selected to be very large as well, without creating numerical difficulties.

To demonstrate the algorithm robustness, iterative multigrid calculations were performed for the NACA 0012 airfoil oscillating harmonically for four cycles of motion to ensure periodicity of the last cycle. The CFL number was selected to be 10 (which corresponds to a spatially varying computational step size) and the over-relaxation factor (ω) was set equal to 1.6. The convergence criteria on a per time step basis was selected as two orders of magnitude, which produced an L_2-norm of the residual of approximately 10^{-3} at each time step. Calculations were performed first using only 32 steps per cycle of motion corresponding to a relatively large physical step size of $\Delta t = 1.20608$. This step

size corresponds to more than one chord of airfoil travel per time step. The forced pitching motion $\alpha(t)$ is shown in Figure 2(a) and the lift and moment coefficient responses, $c_l(t)$ and $c_m(t)$, respectively, are shown together in Figure 2(b). The coefficients indicate that the lift is a relatively linear response that slightly lags the pitching motion and the moment is a highly nonlinear response that lags the motion much more than the lift. Figures 2(c) and 2(d) show the iterative multigrid residual history and the number of supersonic points, respectively, during the last cycle of motion. The residual history essentially represents thirty-two successive multigrid calculations, one per physical time step, wherein the multigrid procedure is used to rapidly reduce the solution residual to the desired level, thus preserving temporal accuracy. By iterating on the solution at each time step, the linearization and factorization errors inherent in the AF2 algorithm are reduced to an acceptable level ($\sim 10^{-3}$) to produce a time accurate solution. The technique is analogous to performing subiterations per time step with CAP-TSD to ensure time accuracy, but the iterative multigrid procedure in ASP3D is cheaper computationally because the iterations are performed on coarser grids within the overall multigrid capability. The ASP3D calculation required about 180 iterations of the multigrid procedure, but since most of the work is done on the coarser Meshes 1 through 4 using W-cycles, rather than on the finest Mesh 5, the total effort is less than iterating using only the finest mesh. The number of supersonic points during the last cycle of pitching motion (Figure 2(d)) is cyclic, as expected, with a larger value in the first half of the cycle than the value attained in the second half because of the small positive mean angle of attack ($\alpha_0 = 0.016°$).

To further test and demonstrate the algorithm robustness of the ASP3D code, calculations for the pitching NACA 0012 airfoil were successively repeated using multiples of the original physical step size including $\Delta t = 2.41216$, 4.82432, and 9.64864, which correspond to 16, 8, and 4 steps per cycle (s/c) of motion, respectively. These values represent huge step sizes that are not usually numerically stable with other TSP computer codes. Admittedly, 16 and 8 steps per cycle barely describe the pitching motion in discrete form, and 4 steps per cycle of motion is the smallest value possible, which actually corresponds to a saw tooth pitching motion rather than a sinusoidal motion. Be that as it may, all of the calculations were numerically stable, and the results for 16, 8, and 4 s/c are presented in Figures 3, 4, and 5. The results are presented in the same format as the results of Figure 2 computed using 32 steps per cycle. Specifically, the pitching motion, the lift and moment coefficient time responses, the last cycle multigrid residual history, and the last cycle number of supersonic points are given in sub-figures (a), (b), (c), and (d), respectively. Comparisons of the results from the 16 s/c calculation (Figure 3) with the results obtained using 32 s/c (Figure 2) indicate that the lift response is very similar and the moment response is not as smooth, possibly because it is difficult to plot the nonlinear moment time history with only 16 straight line segments per cycle. The last cycle residual history shows very similar convergence to the 32 s/c case but only 96 iterations of the multigrid procedure were required to obtain results for 16 s/c, which is approximately half the work required for the 32 s/c results.

Comparisons of the results obtained using 8 s/c (Figures 4(a) – 4(d)) and 4 s/c (Figures 5(a) – 5(d)) with those using 32 s/c (Figures 2(a) – 2(d)) indicate a degradation

in the accuracy of the responses, especially the moment coefficient, but the calculations are numerically stable even though the corresponding step sizes are huge. The number of multigrid iterations required to obtain results with 8 s/c and 4 s/c are 48 and 24, respectively, as indicated in Figures 4(c) and 5(c). These values are exactly half and one-quarter the work required to obtain the results with 16 s/c (96 iterations), which indicates that there is a linear relationship between the number of steps per cycle and the number of multigrid iterations required to obtain results. For example, halving the number of steps per cycle in the calculation cuts the total work in half.

Composite hysteresis plots of the responses in the last cycle of motion are plotted in Figure 6. Figure 6(a) shows the lift coefficient $c_l(t)$ versus the pitching motion $\alpha(t)$ and Figure 6(b) shows the moment coefficient $c_m(t)$ versus the pitching motion $\alpha(t)$. The results from all four sets of calculations are presented corresponding to 32, 16, 8, and 4 s/c of motion. The responses obtained using 32 and 16 s/c compare closely (the discrete points are connected with straight line segments) while the responses obtained using 8 and 4 s/c are less accurate because the corresponding step sizes are too large. However, for easier cases involving smaller amplitudes of motion and less shock motion including flutter onset calculations (due to a small perturbation of the flow) the larger time steps may produce solutions of acceptable accuracy at a fraction of the cost. In any case, use of larger time steps does not create numerical stability problems, and therefore the analyst must make a prudent selection of step size balancing accuracy and cost of calculation.

- **Thickening-Thinning Parabolic Arc Airfoil Results**

The second case considered is that of a parabolic arc airfoil with a time-varying midchord thickness at $M_\infty = 0.85$ and $\alpha_0 = 0°$.[35] The temporal variation in thickness is defined mathematically and graphically in Figure 7. For example, beginning as a flat plate at $t = 0$, the thickness of the parabolic arc airfoil increases smoothly until it reaches maximum thickness of 10% (maximum thickness to chord ratio) at $t = 15$. After $t = 15$ the airfoil thins until it reaches zero thickness at $t = 30$. This case is a simple two-dimensional helicopter rotor simulation that has been used by other researchers for code development purposes.[35] Similarly in the present study, the problem was solved using the ASP3D iterative multigrid procedure involving the five meshes discussed previously. The calculations were performed using a CFL number of 10 and a relatively large physical step size of $\Delta t = 1.0$ for a total of 32 steps. The step size of $\Delta t = 1.0$ corresponds to one chord of airfoil travel per time step. The convergence criteria on a per time step basis was selected as four orders of magnitude, which produced an L_2-norm of the residual of approximately 10^{-5} at each time step. The resulting residual history and number of supersonic points are shown in Figures 8(a) and 8(b), respectively. The residual history (Figure 8(a)) indicates that 184 iterations were required to advance the solution 32 time steps and that each time step required about the same amount of work (5 or 6 iterations) independent of whether the flow was subsonic or transonic. The number of supersonic points (Figure 8(b)) indicates that the solution goes from subsonic to transonic flow at time step 7, with a maximum of about 1250 supersonic points near time step 18 or 19, and back to subsonic flow at time step 27.

For comparison purposes the calculations were repeated with everything the same except for using only the finest Mesh 5. This calculation is referred to as an iterative unigrid calculation (no multigrid) to contrast it with the iterative multigrid calculation of Figure 8. The procedure then only iterates with the solution on the finest mesh, similar to that which is done in the CAP-TSD code when subiterations are applied on a per time step basis. The resulting residual history and number of supersonic points are presented in Figures 9(a) and 9(b), respectively. The residual history (Figure 9(a)) indicates that over 2400 unigrid iterations were required to achieve a similar convergence level as the iterative multigrid calculation (L_2-norm of the residual of approximately 10^{-5} at each time step) and clearly more work (number of iterations) is required when the flow is transonic than when the flow is subsonic. Thus the iterative multigrid calculation (184 total iterations) is far more efficient than the iterative unigrid calculation (over 2400 total iterations), because most of the iterative multigrid work is done on coarser meshes (Meshes 1 through 4). The number of supersonic points (Figure 9(b)) is similar to that shown from the multigrid calculation (Figure 8(b)), such as attaining a maximum of about 1250 supersonic points, since the two flow field solutions should be almost identical.

Instantaneous solutions from the iterative multigrid calculations at t = 8.5, 11.5, 18.25, 26.875, 29.0, and 32.0 are shown in Figures 10, 11, 12, 13, 14, and 15, respectively. These six points in time were selected for later comparison with the published results of Goorjian.[35] The top part (a) of each figure shows the surface pressure coefficient distribution and the bottom part (b) of each figure shows the near field pressure coefficient contour lines. For t = 29.0 and 32.0, the results were taken directly from the multigrid calculations discussed above since the step size was Δt = 1.0 (exactly 29 and 32 total time steps, respectively). To avoid solution interpolation to obtain the results for t = 8.5, 11.5, 18.25, and 26.875, the calculations were repeated four times with step sizes equal to Δt = 8.5/8, 11.5/11, 18.25/18, and 26.875/26, respectively, using 8, 11, 18, and 26 total time steps.

At t = 0 the airfoil has zero thickness (flat plate) so the undisturbed flow is the correct starting solution for the thickening-thinning airfoil problem. As the thickness of the parabolic arc airfoil increases in time the solution develops such that, for example at t = 8.5 (Figures 10(a) and 10(b)), the flow is relatively smooth with very small embedded supersonic regions forming on each side of the airfoil with weak shock waves beginning to develop near 76% chord. As the airfoil further thickens to t = 11.5 (Figures 11(a) and 11(b)) the shock waves grow to moderate strength near 83% chord. The airfoil reaches its maximum thickness of 10% at t = 15, so by t = 18.25 (Figures 12(a) and 12(b)), the embedded supersonic regions are approximately at their largest (1250 supersonic points) and the relatively strong shock waves are located near 91% chord. As the airfoil becomes thinner in time the flow becomes subsonic again and the upper and lower surface shock waves become upstream propagating pressure waves near midchord as indicated at t = 26.875 (Figures 13(a) and 13(b)). At t = 29.0 (Figures 14(a) and 14(b)) the pressure waves have traveled upstream to roughly the airfoil quarter-chord location and by t = 32.0 (Figures 15(a) and 15(b)), when the airfoil has zero thickness again, the pressure

waves on the upper and lower surfaces have moved forward of the airfoil leading edge thus forming a single wave.

Comparisons of surface pressure coefficients for the thickening-thinning parabolic arc airfoil case are presented in Figure 16. The ASP3D pressure distributions at t = 8.5, 11.5, and 18.25 are shown in Figure 16(a) with corresponding full-potential (FP) and TSD pressure distributions from Goorjian[35] shown in Figure 16(b). The FP and TSD results of Reference 35 were obtained using step sizes of 0.0625 and 0.125, respectively, whereas the ASP3D results were obtained using step sizes equal to or greater than 1.0. The ASP3D pressures (Figure 16(a)) are in good agreement with the pressures reported by Goorjjian,[35] (Figure 16(b)) especially in comparison with the full-potential pressure results. Specifically at t = 18.25 where the shock waves are strongest, the ASP3D shock location compares better with the FP result than the TSD result. Further pressure comparisons for t = 26.875, 29.0, and 32.0 are presented in Figure 16(c) from ASP3D and in Figure 16(d) from Reference 35. The ASP3D pressures again agree best with the full-potential pressure distributions, although all of the results indicate that the pressure waves are smeared as they propagate upstream off the airfoil leading edge.

- **Linear Wave Propagation Results**

To understand the importance of accurate wave propagation for unsteady aerodynamic flows, it is instructive to relate some of the work reported over thirty years ago by Tijdeman and Zwaan[36] at the NLR in Amsterdam. Reference 36 contains a discussion of the propagation of pressure waves in high subsonic and transonic flows. The authors looked at disturbance wave fronts generated by a harmonically pulsating source at the three-quarter-chord location (control surface hinge line) along an airfoil, presented here in Figure 17 taken from their report. Figure 17(a) shows upstream propagating wave fronts for a subsonic freestream Mach number of M_∞ = 0.8 and Figure 17(b) similarly shows wave fronts for a transonic Mach number of M_∞ = 0.875. The latter flow involves an embedded supersonic region on the airfoil terminated by a shock wave near midchord. In the upper parts of the two figures the positions of the wave fronts are drawn at equal time intervals for the slowly moving receding waves. The lower parts of the figures show the same wave fronts, but for a uniform flow (i.e., without the airfoil) as a reference. At the subsonic freestream Mach number of M_∞ = 0.8 (Figure 17(a)), the actual (upper) wave fronts move a little slower than the uniform flow (lower) as suggested by the closer spacing of the curves representing the fronts. The spacing of the wave fronts is a measure of the intensity of the local pressure gradients. Also the wave fronts incline forward slightly due to the vertical velocity gradient. At the transonic Mach number of M_∞ = 0.875 (Figure 17(b)), the lower part of the actual wave fronts coalesce into the shock wave. The upper parts of the wave fronts rotate about the top of the shock and enter the supersonic region at an oblique angle, inclined in comparison to the uniform flow. The waves are slowed significantly near the shock wave thus producing a strong pressure gradient there, as expected. Also, the longer time required for the wave fronts to travel around the shock wave leads to a significant time lag in the airfoil aerodynamic response. Although not demonstrated here, this time lag is generally regarded as the physical mechanism responsible for the so-called transonic flutter dip.

Tijdeman and Zwaan[36] also presented wind tunnel results in the form of shadowgraph photographs of high-speed flows about an airfoil reproduced here in Figure 18. The upstream propagating wave fronts are generated by vortex streets emanating from the aft end of the airfoil with its trailing edge control surface removed. Figure 18(a) shows the shadowgraph for the subsonic Mach number of $M_\infty = 0.8$ wherein the receding wave fronts have relatively uniform spacing and they are slightly inclined as in the diagram of Figure 17(a). Figure 18(b) shows the shadowgraph for the transonic Mach number of $M_\infty = 0.875$ wherein the lower parts of the receding wave fronts coalesce near the foot of the shock wave and the upper parts of the fronts rotate around the top of the shock to enter the supersonic region, similar to that diagrammed in Figure 17(b). These figures illustrate some of the flow field complexities for unsteady transonic aerodynamics that computational methods must be able to model accurately.

It also is instructive to examine the simpler linear theory wave propagation characteristics of the upstream and downstream propagating wave fronts in a uniform flow and the implications for resolving such waves using discrete computational methods. For example, Figures 19(a) and 19(b) show wave numbers for upstream and downstream propagating wave fronts, respectively, as a function of Mach number for various values of reduced frequency k. The wave number associated with upstream propagating wave fronts is defined by

$$\text{wave number} = \frac{M_\infty}{1 - M_\infty} k$$

and the wave number associated with downstream propagating wave fronts is defined by

$$\text{wave number} = \frac{M_\infty}{1 + M_\infty} k$$

According to Rowe and Cunningham,[37] "The wave number is a useful parameter for assessing the waviness of pressure distributions and estimating relative difficulties in predicting converged values of generalized forces." Computational fluid dynamics (CFD) methods such as CAP-TSD or ASP3D are typically capable of computing propagating wave fronts for wave numbers less than about 5.0 depending upon the density of the mesh and the size of the physical time step. Therefore the computation of most downstream propagating waves (shown in Figure 19(b)) with associated wave numbers less than about 2.0 is not difficult because the waves are moving very fast (with the freestream), although relatively small time steps may be required to accurately describe downstream running waves at higher reduced frequency. In contrast, the computation of upstream propagating wave fronts is difficult at higher reduced frequencies because the associated wave number is much higher, as shown in Figure 19(a). Pressure distributions with wave numbers higher than about 5.0 have significant waviness that can be difficult to capture with CFD methods as discussed below. As the Mach number increases toward unity from the subsonic side the problem is exacerbated, because the waves are moving increasingly slowly (against the freestream). The wave number curves in Figure 19(a) asymptote to infinity at Mach one because the wave fronts

there are theoretically standing waves. And for supersonic freestream there can be no upstream propagation.

Another way of looking at the linear theory wave propagation characteristics is by plotting the reduced frequency of the upstream and downstream propagating wave fronts as functions of Mach number for various values of the wavelength λ as presented in Figures 20(a) and 20(b), respectively. The upstream values are computed by

$$k = \frac{1 - M_\infty}{M_\infty} \frac{\pi}{\lambda}$$

and the downstream values are computed by

$$k = \frac{1 + M_\infty}{M_\infty} \frac{\pi}{\lambda}$$

For the upstream propagating wave fronts (Figure 20(a)) the reduced frequency and wavelength are inversely proportional. As the Mach number approaches unity from the subsonic side the reduced frequency is reduced for a given wavelength until the singular limit at Mach one is reached where a standing wave can occur. The small wavelength fronts that may be regarded as being outside the range of practical reduced frequencies for Mach numbers of, say, M_∞ = 0.8, are in fact within the range encountered in aeroelasticity (approximately $0 < k < 2$) at higher Mach numbers of 0.9 or 0.95. Therefore the accurate resolution of these small wavelength wave fronts should be of concern for CFD development. Of course for supersonic freestream there is no upstream wave propagation. For the downstream propagating wave fronts (Figure 20(b)) the reduced frequency is again inversely proportional to the wavelength. But here, wavelengths less than about 4.0 result in reduced frequencies that are outside the typical range encountered in aeroelasticity. Conversely, wavelengths greater than 4.0 correspond to reduced frequencies less than 2.0 for any Mach number, but since these wavelengths are so large, they can be represented easily with most CFD codes given a sufficient grid and appropriate step size. Therefore it is the upstream propagating waves where the performance of these codes needs to be tested.

Rowe and Cunningham[37] presented lifting pressure coefficient distributions for unsteady cases involving high wave numbers. Similarly, Figure 21 shows the effects of Mach number on the lifting pressure coefficient distributions for a flat plate airfoil oscillating in pitch about the leading edge at k = 0.9. Figure 21(a) shows the real or in-phase component of the pressure and Figure 21(b) shows the imaginary or out-of-phase component of the pressure. The results were computed using the two-dimensional assumed-pressure-mode kernel-function linear-aerodynamics program of Bland.[41] The figures clearly show that as the freestream Mach number increases from 0.75 to 0.95 more waves occur in the pressure distribution. For the Mach numbers of 0.75, 0.80, 0.85, 0.90, and 0.95, the corresponding upstream propagating wave numbers are 2.7, 3.6, 5.1, 8.1, and 19.0, respectively.

Figure 22(a) shows the lifting pressure coefficient distribution computed using the ASP3D code for the flat plate airfoil oscillating in pitch about the leading edge at $k = 0.9$. The freestream Mach number was selected as $M_\infty = 0.9$ and the linear theory results from the previous Figure 21 that had a relatively high wave number of 8.1 are repeated here for comparison purposes. It also is a case studied in Reference 37. Figure 22(a) shows the real and imaginary ASP3D pressures, which agree with the linear theory pressures near the trailing edge, but do not agree with linear theory as the waves propagate upstream toward the leading edge. The ASP3D results were obtained using a first-order-accurate backward difference formula to compute the ϕ_{xt} term. A backward difference formula is typically used to compute the ϕ_{xt} term in TSP codes for stability reasons, and similar erroneous results were obtained using CAP-TSD. However in ASP3D, second- and third-order-accurate formulas have been successfully implemented to improve the temporal accuracy of the results for higher wave number cases. The pressure distribution for this case computed using the second-order-accurate formula is presented in Figure 22(b). These results show a marked improvement in accuracy in comparison with the linear theory result. Results using the third-order-accurate formula are identical to plotting accuracy with the second-order-accurate results, and thus, they are not presented here.

- **NACA 0012 Airfoil Aeroelastic Transient Results**

To assess and demonstrate the aeroelasticity capability in ASP3D, calculations were performed for the NACA 0012 airfoil at $M_\infty = 0.8$ and $\alpha_0 = 0°$, a case considered by Robinson, et al.[38] using the CFL3D[42] code run in Euler mode. Steady-state calculations were performed first, using ASP3D including entropy and vorticity effects, to provide the initial conditions for aeroelastic computation upon restart. The resulting steady pressure coefficient distribution is presented in Figure 23(a) with the corresponding CFL3D (Euler) pressure distribution from Ref. 38 presented in Figure 23(b). The ASP3D pressure distribution is in very good agreement with the CFL3D pressure distribution whereby the shock waves on the upper and lower surfaces of the airfoil are predicted to be near midchord. In the ASP3D calculation the shock waves are captured sharply because of the use of the Godunov type-dependent switch and the pressure levels are well predicted including those near the airfoil leading edge (stagnation).

For aeroelastic analysis, the NACA 0012 airfoil was modeled structurally with two degrees of freedom, bending and torsion. The case considered is the much-studied Case "A" of Isogai[39] which has normal modes similar to those of a streamwise section of a sweptback wing. The wind-off bending and torsion natural frequencies are 71.33 and 535.65 rad/s, respectively. The pivot point for the bending mode is located 1.44 chordlengths upstream of the leading edge of the airfoil. The pivot point for the torsion mode is 0.068 chordlengths forward of midchord. These mode shapes and natural frequencies were determined by performing a free vibration analysis with the aeroelastic equations written in the traditional form of plunge and pitch degrees of freedom. In this analysis, the following structural parameter values were used: $a = -2.0$, $x_\alpha = 1.8$, $r_\alpha = 1.865$, $\omega_h = 100$ rad/s, and $\omega_\alpha = 100$ rad/s. Also, the airfoil mass ratio was $\mu = 60$. Generalized displacements corresponding to the bending and torsion modes are defined

as $q_1(t)$ and $q_2(t)$, respectively. Initial conditions for the time-marching aeroelastic calculations were $dq_1(0)/dt = 2.0$ and $dq_2(0)/dt = 1.0$.

Aeroelastic calculations were performed for the NACA 0012 airfoil at $M_\infty = 0.8$ and $\alpha_0 = 0°$ for several values of the nondimensional dynamic pressure including $Q = 0.2$, 0.5, and 0.8, where $Q = (U_\infty/b\omega_\alpha\sqrt{\mu})^2$. In these calculations a smaller value of the step size was selected than in previous unsteady calculations, $\Delta t = 0.1$, to ensure that the higher frequency torsion mode would be resolved in the aeroelastic integration. Also the multigrid procedure was not exercised because the computational benefit would not be as large for such a step size. The generalized displacements for $Q = 0.2$, 0.5, and 0.8 are presented in Figures 24, 25, and 26, respectively. For $Q = 0.2$ (Figure 24), the generalized displacements indicate that the aeroelastic system is stable because the transients are converging in time. The $q_1(t)$ generalized displacement is dominated by the lower frequency bending mode and the $q_2(t)$ generalized displacement contains both modes including the higher frequency torsion mode. Use of the step size of $\Delta t = 0.1$ resulted in approximately 133 s/c for the bending mode and only 20 s/c for the higher frequency torsion mode. Use of much larger time steps, although numerically stable, produces results that inaccurately describe the torsion mode.

For $Q = 0.5$ (Figure 25), the generalized displacements indicate that the aeroelastic system is near-neutrally stable (flutter) since the dominant bending mode in both $q_1(t)$ and $q_2(t)$ is not damped. This correlates well with the reported results from Ref. 38 wherein the transients computed using CFL3D (Euler) at $Q = 0.5$ were described as near-neutrally stable corresponding to flutter. Also the $q_2(t)$ generalized displacement indicates that the higher frequency torsion mode is more damped than at $Q = 0.2$. Finally for $Q = 0.8$ (Figure 26), the generalized displacements $q_1(t)$ and $q_2(t)$ are both diverging corresponding to an unstable aeroelastic system and the higher frequency torsion mode contained within $q_2(t)$ has even more damping than the $Q = 0.2$ and 0.5 transients.

- **F-5 Fighter Wing Harmonic Pitching Results**

The F-5 fighter wing[40] has a leading edge sweep of 31.92 degrees, an aspect ratio of 1.578, and a taper ratio of 0.283. The wing has a NACA 65A004.8 airfoil section that has a drooped leading edge. The wing was modeled for ASP3D applications using a 97 x 25 x 65 finite volume mesh as shown in Figure 27. A near field view of the 97 x 25 planform mesh is shown in Figure 27(a) and a near field view of the 97 x 65 root sectional mesh is shown in Figure 27(b). The meshes were generated using a program[43] that was created to construct meshes specifically for use by the ASP3D code, and as such, it can generate meshes for aircraft configurations with multiple lifting surfaces, with multiple leading and trailing edge controls, and a fuselage. The mesh generator automatically creates the input file for ASP3D by using an extension of the polynomial mesh generation procedure developed by Bland.[44] Here though, the equations were generalized to the physical domain rather than the computational domain, which allows the creation of three-dimensional meshes about swept tapered planforms with the ability to control the spacing along the leading and trailing edges. This is especially an issue in the outboard region of the wing near the tip. For example, Figures 28(a) and 28(b) show

near field views of the planform mesh near the wing tip leading and trailing edges, respectively, for the F-5 wing. The figures show that the mesh was generated with a uniform spacing about the leading and tailing edges in the streamwise direction, and in fact, the spacing is also uniform across the tip in the spanwise direction. The planform mesh also emphasizes that all edges of the lifting surface are modeled with grid lines for ASP3D application. This is in contrast with meshes generated for CAP-TSD application, which cannot have grid lines on leading edges or the edge of the wake (wing tip) because of singularities that occur along these lines. Details of the mesh generation procedures developed for the ASP3D computer program are presented by Batina.[43]

To demonstrate the multigrid procedures for a three dimensional case, calculations were performed using the 97 x 25 planform mesh (termed Mesh 4) and three subsets of the mesh (Meshes 1 through 3) determined by simply deleting every other grid line. This is done automatically within the ASP3D code and thus is not something that the user needs to do during mesh generation. The four planform meshes are shown in Figures 29(a) to 29(d) including the total number of points in each direction for each mesh. The smallest mesh, for example, is a very coarse 13 x 4 mesh, which has only a few cells on the surface of the wing. Similarly, near field views of the corresponding four sectional meshes at the root of the F-5 wing are shown in Figures 30(a) through 30(d) with the airfoil slit in the center of each plot. The individual figures illustrate the relative mesh density near the airfoil surface along the wing root.

To demonstrate the iterative multigrid capability for time-dependent applications in three dimensions, unsteady calculations were performed for the F-5 fighter wing pitching about the root midchord with an amplitude of $\alpha_1 = 0.109°$ and a reduced frequency based on root semichord of $k = 0.137$. In these calculations the freestream Mach number was $M_\infty = 0.899$ and the mean angle of attack was $\alpha_0 = -0.005°$. The wing was forced to oscillate harmonically in pitch for four cycles of motion as shown in Figure 31(a), to ensure periodicity of the flow field, with the resulting lift and moment coefficients shown in Figure 31(b). The calculations were performed using only sixteen steps per cycle of motion, corresponding to a very large time step of $\Delta t = 1.433$, wherein the multigrid procedure was used at each time step to reduce the solution residual by two orders of magnitude as shown in Figure 31(c). By iterating on the solution at each time step, the linearization and factorization errors inherent in the AF2 algorithm are reduced to an acceptable level ($\sim 10^{-4}$) to produce a time accurate solution. The technique is analogous to performing subiterations per time step with CAP-TSD to ensure time accuracy, but the iterative multigrid procedure in ASP3D is cheaper computationally because the iteration is performed on coarser grids within the overall multigrid capability. The corresponding number of supersonic points is presented in Figure 31(d).

The resulting unsteady pressure coefficient distributions, normalized by the amplitude of motion and interpolated to the span stations where the NLR experimental pressure data[40] were measured, are presented in Figure 32. The unsteady pressure distributions on the upper surface of the wing are shown in Figure 32(a) and the unsteady pressure distributions on the lower surface of the wing are shown in Figure 32(b). The ASP3D pressure distributions were computed from the fourth cycle of motion and the

real and imaginary parts of the pressures are the in-phase and out-of-phase components of the pressure time histories, respectively. The unsteady pressures on the upper surface of the wing agree reasonably well with the experimental data[40] except near the shock wave. Here the magnitude of the pressure pulse due to the movement of the shock wave is slightly over predicted in the ASP3D calculation because of the neglect of viscous effects. On the lower surface of the wing (Figure 32(b)) the unsteady pressures are in very good agreement with the experimental data, with relatively uniform agreement with the data from the wing root to the wing tip.

Conclusions

A new computer program has been developed called ASP3D (Advanced Small Perturbation – 3D), which solves the small perturbation potential flow equation in an advanced form including mass-consistent surface and trailing wake boundary conditions, and entropy, vorticity, and viscous effects. The purpose of the program is for unsteady aerodynamic and aeroelastic analyses, especially in the nonlinear transonic flight regime. The program exploits the simplicity of stationary Cartesian meshes with the movement or deformation of the configuration under consideration incorporated into the solution algorithm through a planar surface boundary condition. The ASP3D code is the result of a decade of developmental work on improvements to the small perturbation formulation, performed while the author was employed as a Senior Research Scientist in the Configuration Aerodynamics Branch at the NASA Langley Research Center. The ASP3D code is a significant improvement to the state-of-the-art for transonic aeroelastic analyses over the CAP-TSD code (Computational Aeroelasticity Program – Transonic Small Disturbance), which was developed principally by the author in the mid-1980s.

The ASP3D code involves a modern cell-centered finite-volume discretization, which allows exact planform treatment including leading edges, wing tips, and control surface edges. It can treat aircraft configurations involving multiple lifting surfaces with leading and trailing edge control surfaces, and a fuselage. The advanced-small-perturbation potential flow equation is solved numerically using either an AF1- or an AF2-type approximate factorization algorithm. The AF1 algorithm within the ASP3D code is the cell-centered finite-volume version of the AF1 finite-difference algorithm developed for CAP-TSD. However, the AF1 algorithm is susceptible to the so-called moving shock instability if shock waves move more than one grid point or cell per time step. In contrast, the AF2 scheme has a temporal damping term that eliminates the moving shock instability by design, and thus, the AF2 algorithm is more robust than the AF1 scheme. Thus, with the AF2 approach, convergence to steady state is achieved with large time steps or large CFL numbers. And because the moving shock instability does not occur, the AF2 algorithm of the ASP3D code is amenable to multigrid implementation. Therefore, a multigrid procedure was developed within ASP3D that may be used for steady or iterative unsteady applications. The procedure was implemented in FAS (full approximation scheme) form, which is applicable to nonlinear governing equations. The multigrid procedure may be used for unsteady calculations when local iteration is applied. Therefore, the physical time step may be selected for the accuracy of the problem under consideration independent of numerical stability issues,

and a large computational step size or CFL number may be selected for rapid convergence of the iterative procedure.

Unsteady aerodynamic and aeroelastic applications of ASP3D were presented to assess the time dependent capability and demonstrate various features of the code. The cases considered included: (1) the NACA 0012 airfoil undergoing a forced harmonic pitching motion about the quarter chord at transonic conditions, (2) a thickening-thinning parabolic arc airfoil at a transonic Mach number, (3) an investigation of wave propagation characteristics with emphasis on high wave number applications, (4) aeroelastic transient calculations for the NACA 0012 airfoil at values of the dynamic pressure below, near, and above the flutter value, and (5) the F-5 fighter wing undergoing a rigid pitching motion about the wing root midchord axis. The results compared well with alternative methods and experimental data, and thus demonstrated the efficiency and utility of the ASP3D code for various unsteady aerodynamic and aeroelastic applications.

Acknowledgments

The NASA Langley Research Center supported the work contained herein while the author was employed as a Senior Research Scientist in the Configuration Aerodynamics Branch. The author thanks Dr. David M. Schuster, Head, Structures and Thermal Systems Branch, formerly Chief Engineer, Research and Technology Directorate, for reviewing the original draft and help in getting the manuscript published.

References

1. Bennett, R. M.; Bland, S. R.; Batina, J. T.; Gibbons, M. D.; and Mabey, D. G.: Calculation of Steady and Unsteady Pressures on Wings at Supersonic Speeds with a Transonic Small-Disturbance Code, AIAA Paper No. 87-0851, April 1987.

2. Cunningham, H. J.; Batina, J. T.; and Bennett, R. M.: Modern Wing Flutter Analysis by Computational Fluid Dynamics Methods, ASME Paper No. 87-WA/Aero-9, December 13-18, 1987; also *Journal of Aircraft*, Vol. 25, October 1988, pp. 962-968.

3. Bennett, R. M.; Batina, J. T.; and Bland, S. R.: Wing-Flutter Calculations with the CAP-TSD Unsteady Transonic Small-Disturbance Program, AIAA Paper No. 88-2347, April 1988; also *Journal of Aircraft*, Vol. 26, September 1989, pp. 876-882.

4. Gibbons, M. D.: Aeroelastic Calculations using CFD for a Typical Business Jet Model, NASA CR-4753, September 1996.

5. Batina, J. T.; Seidel, D. A.; Bland, S. R.; and Bennett, R. M.: Unsteady Transonic Flow Calculations for Realistic Aircraft Configurations, AIAA Paper No. 87-0850, April 1987; also *Journal of Aircraft*, Vol. 26, January 1989, pp. 21-28.

6. Batina, J. T.: An Efficient Algorithm for Solution of the Transonic Small-Disturbance Equation, AIAA Paper No. 87-0109, January 1987; also *Journal of Aircraft*, Vol. 25, July 1988, pp. 598-605.

7. Batina, J. T.: A Finite-Difference Approximate-Factorization Algorithm for Solution of the Transonic Small-Disturbance Equation, NASA TP 3129, January 1992.

8. Gibbons, M. D.: personal communication, October 20, 1994.

9. Steinhoff, J.; and Jameson, A.: Multiple Solutions of the Transonic Potential Flow Equation, AIAA Paper No. 81-1019, June 1981.

10. Williams, M. H.; Bland, S. R.; and Edwards, J. W.: Flow Instabilities in Transonic Small Disturbance Theory, NASA TM 86251, January 1985.

11. Batina, J. T.: Unsteady Transonic Algorithm Improvements for Realistic Aircraft Applications, AIAA Paper No. 88-0105, January 1988; also *Journal of Aircraft*, Vol. 26, February 1989, pp. 131-139.

12. Batina, J. T.: Unsteady Transonic Small-Disturbance Theory Including Entropy and Vorticity Effects, AIAA Paper No. 88-2278, April 1988; also *Journal of Aircraft*, Vol. 26, June 1989, pp. 531-538.

13. Batina, J. T.: Advanced Small Perturbation Potential Flow Theory for Unsteady Aerodynamic and Aeroelastic Analyses, NASA/TM-2005-213908, November 2005.

14. Whitfield, D. L.: Analytical Description of the Complete Two-Dimensional Turbulent Boundary-Layer Velocity Profile, AEDC-TR-77-79, September 1977; also AIAA Paper No. 78-1158, July 1978.

15. Swafford, T. W.: Analytical Approximation of Two-Dimensional Separated Turbulent Boundary-Layer Velocity Profiles, AEDC-TR-79-99, October 1980.

16. Drela, M.: Two-Dimensional Transonic Aerodynamic Design and Analysis Using the Euler Equations, GTL Report No. 187, February 1986.

17. Batina, J.T.: Introduction to the ASP3D Computer Program for Unsteady Aerodynamic and Aeroelastic Analyses, NASA/TM-2005-213909, December 2005.

18. Kuethe, A. M.; and Chow, C.-Y.: *Foundations of Aerodynamics: Bases of Aerodynamic Design*, John Wiley and Sons, New York, Third Edition, 1976.

19. Hafez, M.; and Lovell, D.: Entropy and Vorticity Corrections for Transonic Flows, AIAA Paper No. 83-1926, July 1983.

20. Clebsch, A.: Uber die Integration der Hydrodynamischen Gleichungen, *J. Reine Angew. Math.,* Vol. 57, 1959, pp. 1-10.

21. Grossman, B.: The Computation of Inviscid Rotational Gasdynamic Flows Using an Alternate Velocity Decomposition, AIAA Paper No. 83-1900, July 1983.

22. Dang, T. Q.; and Chen, L. T.: An Euler Correction Method for Two- and Three-Dimensional Transonic Flows, AIAA Paper No. 87-0522, January 1987.

23. Fuglsang, D. F.; and Williams, M. H.: Non-Isentropic Unsteady Transonic Small Disturbance Theory, AIAA Paper 85-0600, April 1985.

24. Howlett, J. T.: Efficient Self-Consistent Viscous-Inviscid Solutions for Unsteady Transonic Flow, AIAA Paper No. 85-0482, January 1985.

25. Howlett, J. T.: Calculation of Unsteady Transonic Flows With Mild Separation by Viscous-Inviscid Interaction, NASA TP 3197, June 1992.

26. Edwards, J. W.: Transonic Shock Oscillations Calculated with a New Interactive Boundary Layer Coupling Method, AIAA Paper No. 93-0777, January 1993.

27. Godunov, S.: A Finite Difference Method for the Numerical Computation of Discontinuous Solutions of the Equations of Fluid Dynamics, *Mathematics of the USSR*, Sbornik, Vol. 47, 1959.

28. Engquist, B. E.; and Osher, S. J.: Stable and Entropy Satisfying Approximations for Transonic Flow Calculations, *Mathematics of Computation*, Vol. 34, No. 149, January 1980, pp. 45-75.

29. Murman, E. M.: Analysis of Embedded Shock Waves Calculated by Relaxation Methods, Proceeds of the AIAA Computational Fluid Dynamics Conference, July 1973, pp. 27-40.

30. Ballhaus, W. F.; Jameson, A.; and Albert, J.: Implicit Approximate-Factorization Schemes for Steady Transonic Flow Problems, *AIAA Journal*, Vol. 16, June 1978, pp. 573-579.

31. Jameson, A.: Acceleration of Transonic Potential Flow Calculations on Arbitrary Meshes by the Multiple Grid Method, AIAA Paper No. 79-1458, July 1979.

32. Brandt, A.: Multi-Level Adaptive Solutions to Boundary-Value Problems, *Mathematics of Computation*, Vol. 31, April 1977, pp. 333-390.

33. Anderson, W. K.: Implicit Multigrid Algorithms for the Three-Dimensional Flux Split Euler Equations, Doctoral Thesis, Mississippi State University, Mississippi, August 1986.

34. Landon, R. H.: "NACA 0012. Oscillating and Transient Pitching," Data Set 3 in AGARD-R-702, *Compendium of Unsteady Aerodynamic Measurements*, August 1982.

35. Goorjian, P. M.: Implicit Computations of Unsteady Transonic Flow Governed by the Full Potential Equation in Conservation Form, AIAA Paper No. 80-0150, January 1980.

36. Tijdeman, H.; and Zwaan, R. J.: On the Prediction of Aerodynamic Loads on Oscillating Wings in Transonic Flow, National Aerospace Laboratory, the Netherlands, NLR MP 73026 U, April 1973.

37. Rowe, W. S.; and Cunningham, H. J.: On the Convergence of Unsteady Generalized Aerodynamic Forces, *Journal of Aircraft*, Vol. 21, June 1984, pp.420-427.

38. Robinson, B. A.; Batina, J. T.; and Yang, H. T. Y.: Aeroelastic Analysis of Wings Using the Euler Equations with a Deforming Mesh, *Journal of Aircraft*, Vol. 28, November 1991, pp. 778-788.

39. Isogai, K.; and Suetsuga, K.: Numerical Simulation of Transonic Flutter of a Supercritical Wing, National Aerospace Laboratory, Japan, Report TR-276T, August 1982.

40. Tijdeman, H.; Van Nunen, J. W. G.; Kraan, A. N.; Persoon, A. J.; Poestkoke, R.; Roos, R.; Schippers, P.; and Siebert, C. M.: Transonic Wind Tunnel Tests on an Oscillating Wing with External Stores, AFFDL-TR-78-194, December 1978.

41. Bland, S. R.: Development of Low-Frequency Kernel-Function Aerodynamics for Comparison with Time-Dependent Finite-Difference Methods, NASA TM 83283, May 1982.

42. Anderson, W. K.; Thomas, J. L.; and van Leer, B.: Comparison of Finite-Volume Flux-Vector Splittings for the Euler Equations, AIAA Paper No. 85-0122, January 1985.

43. Batina, J. T.: Automated Mesh Generation for the ASP3D Computer Program, to be published.

44. Bland, S. R.: Interactive Grid Generation Program for CAP-TSD, NASA TM 102705, October 1990.

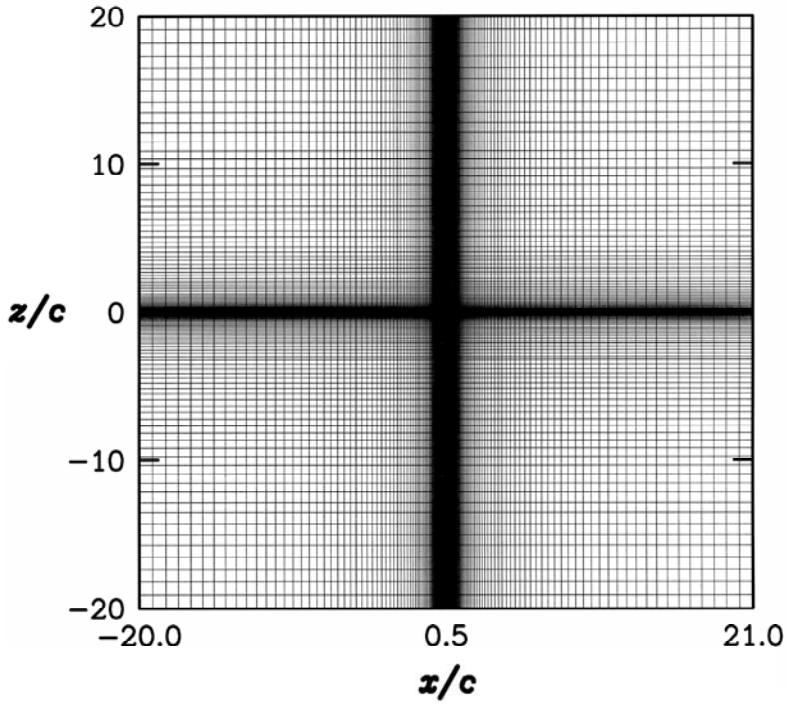

(a) Total mesh.

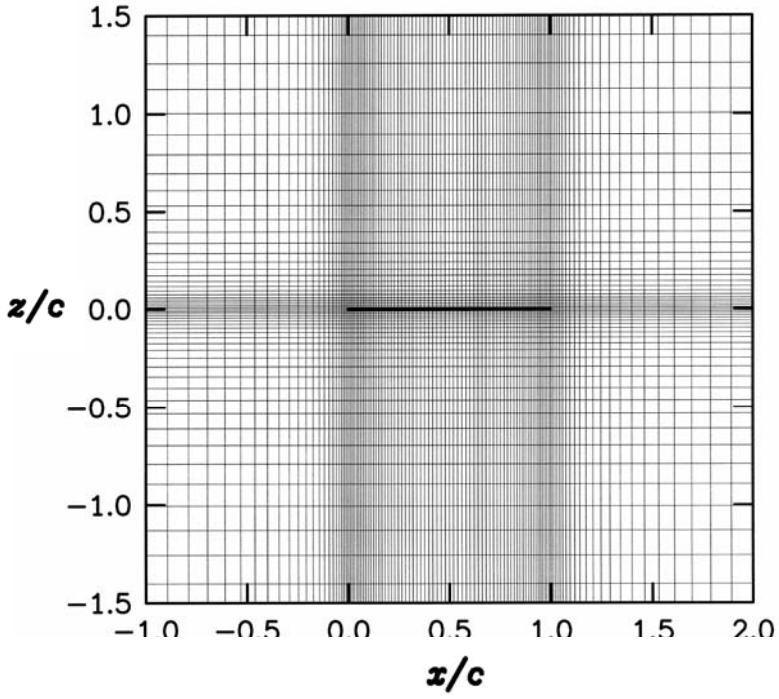

(b) Near field view.

Figure 1 – Cartesian finite-volume mesh (193 x 129) with twenty-chord extent for airfoil unsteady aerodynamic and aeroelastic applications with the ASP3D computer program.

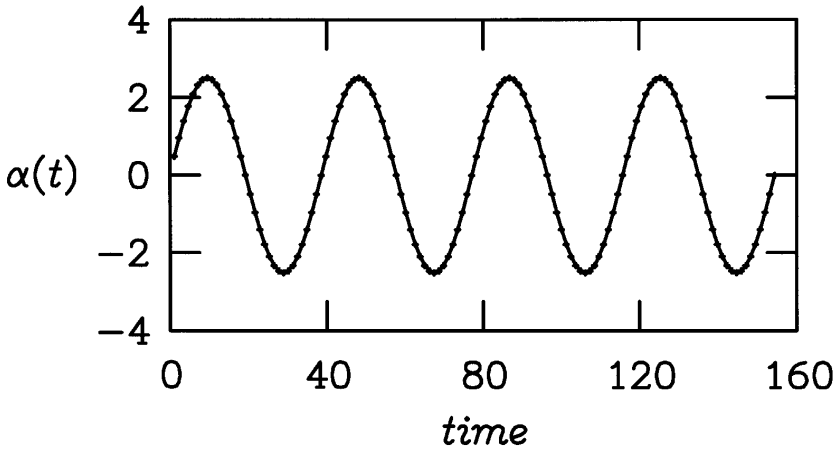

(a) Forced harmonic pitching for four cycles of motion.

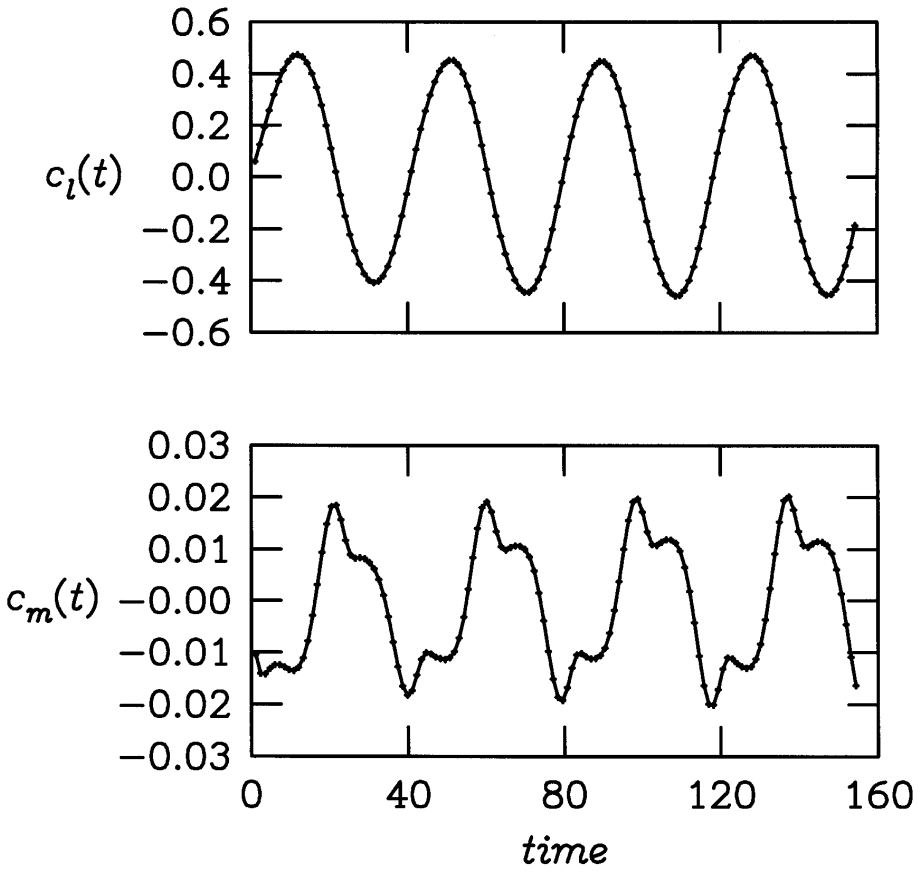

(b) Lift and moment coefficient responses.

Figure 2 – Iterative multigrid calculation using 32 steps per cycle of motion for the NACA 0012 airfoil oscillating harmonically in pitch about the quarter chord at M_∞ = 0.755, α_0 = 0.016°, α_1 = 2.51°, and k = 0.0814.

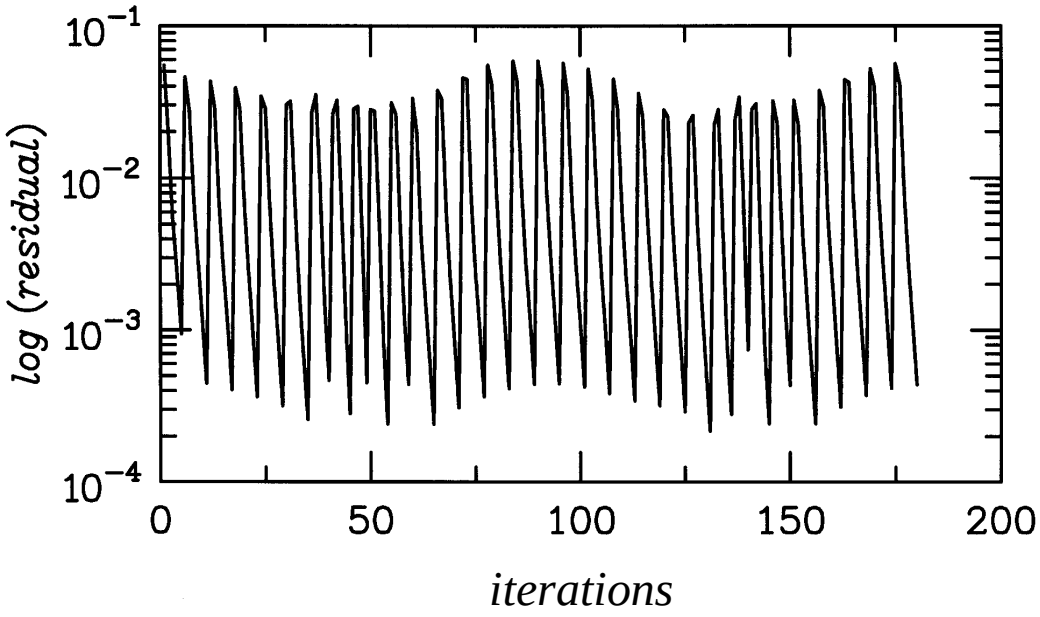

(c) Last cycle of the iterative multigrid residual history.

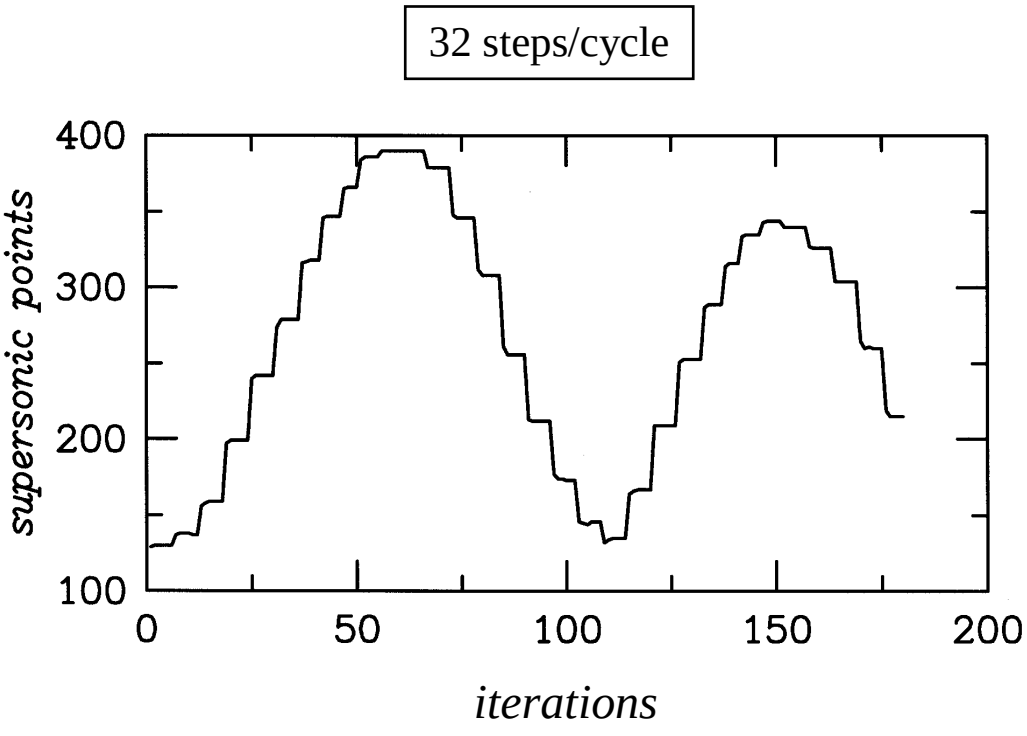

(d) Last cycle of the number of supersonic points.

Figure 2 – Concluded.

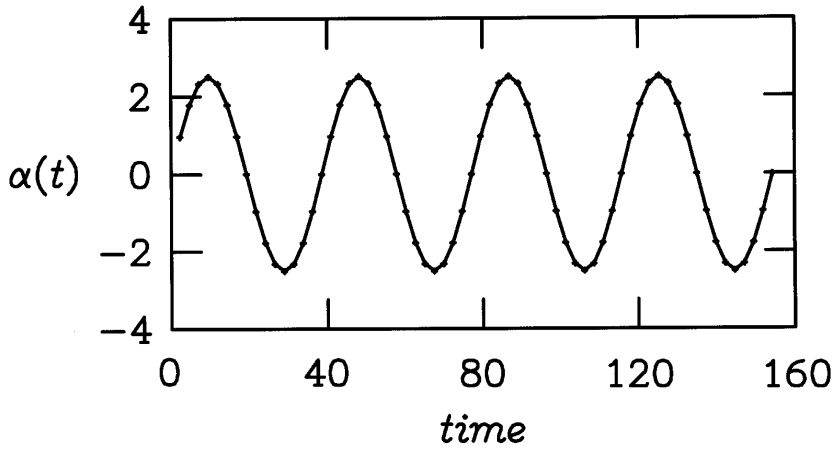

(a) Forced harmonic pitching for four cycles of motion.

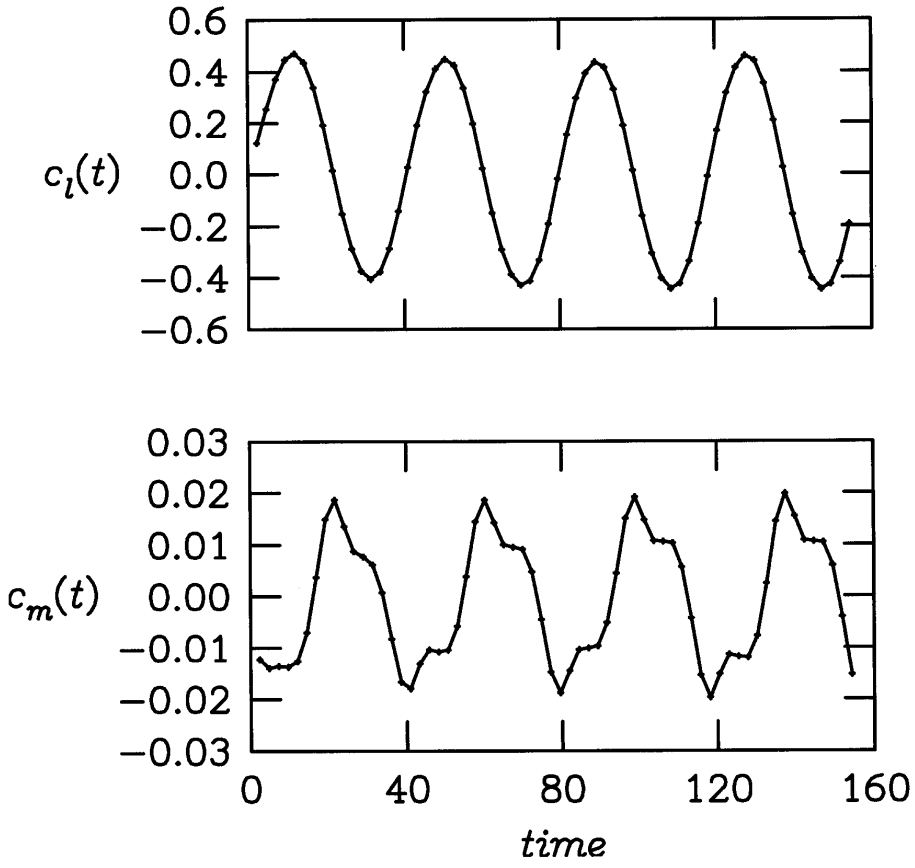

(b) Lift and moment coefficient responses.

Figure 3 – Iterative multigrid calculation using 16 steps per cycle of motion for the NACA 0012 airfoil oscillating harmonically in pitch about the quarter chord at M_∞ = 0.755, α_0 = 0.016°, α_1 = 2.51°, and k = 0.0814.

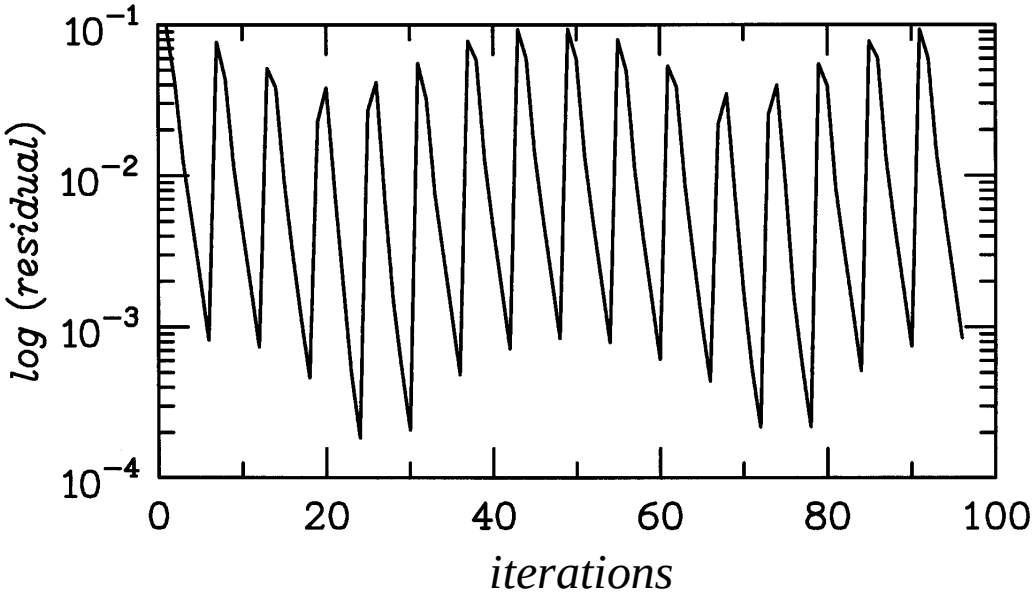

(c) Last cycle of the iterative multigrid residual history.

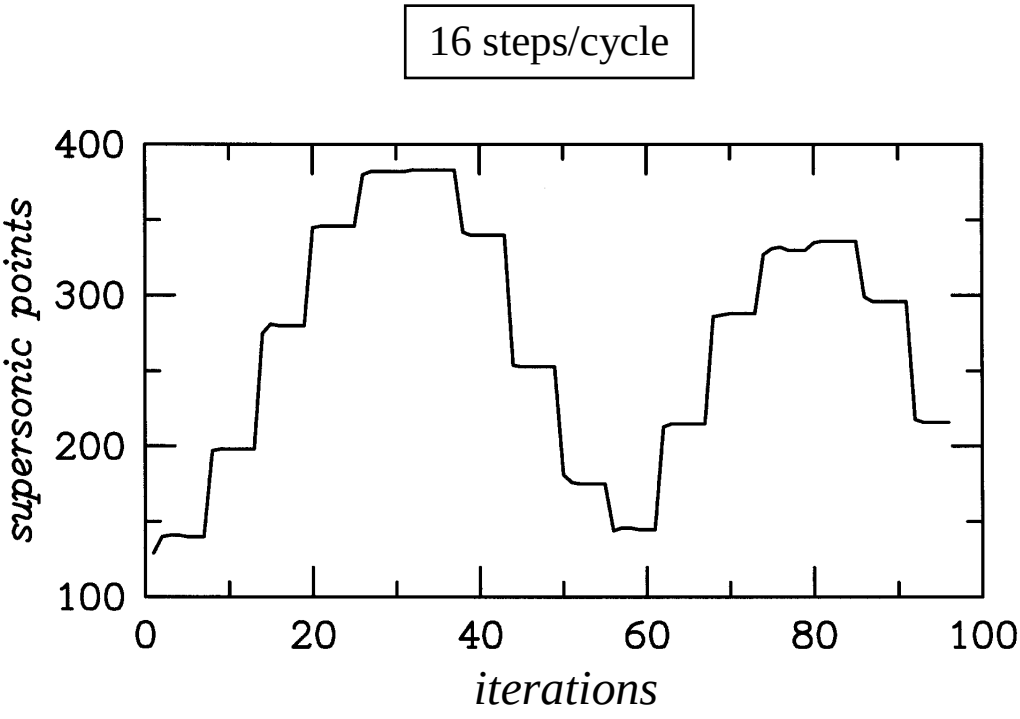

(d) Last cycle of the number of supersonic points.

Figure 3 – Concluded.

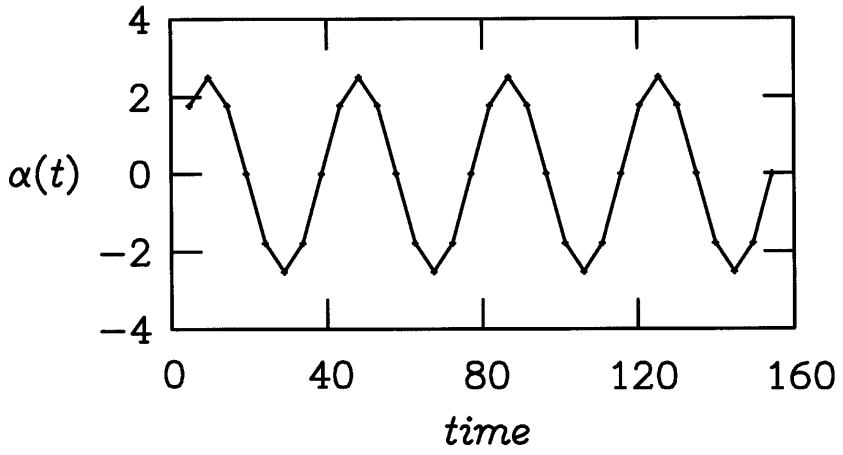

(a) Forced harmonic pitching for four cycles of motion.

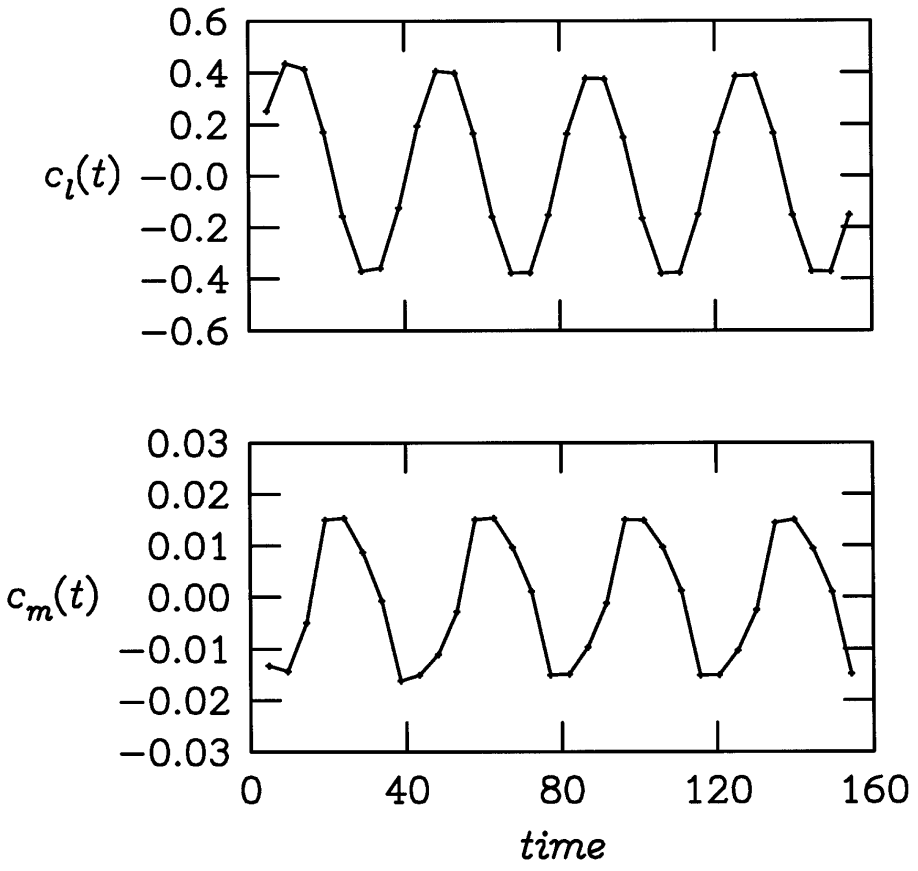

(b) Lift and moment coefficient responses.

Figure 4 – Iterative multigrid calculation using 8 steps per cycle of motion for the NACA 0012 airfoil oscillating harmonically in pitch about the quarter chord at M_∞ = 0.755, α_0 = 0.016°, α_1 = 2.51°, and k = 0.0814.

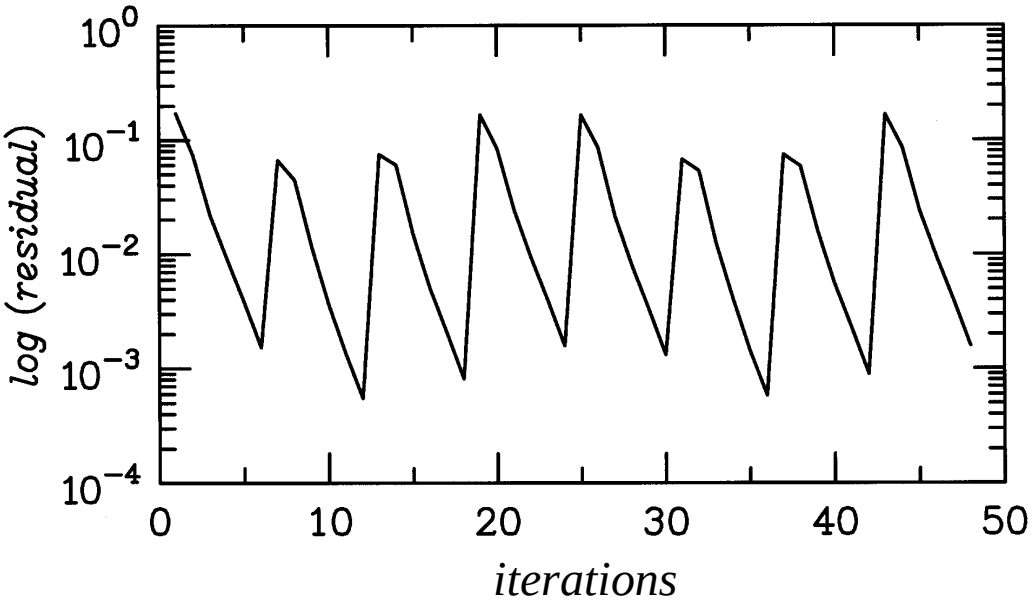

(c) Last cycle of the iterative multigrid residual history.

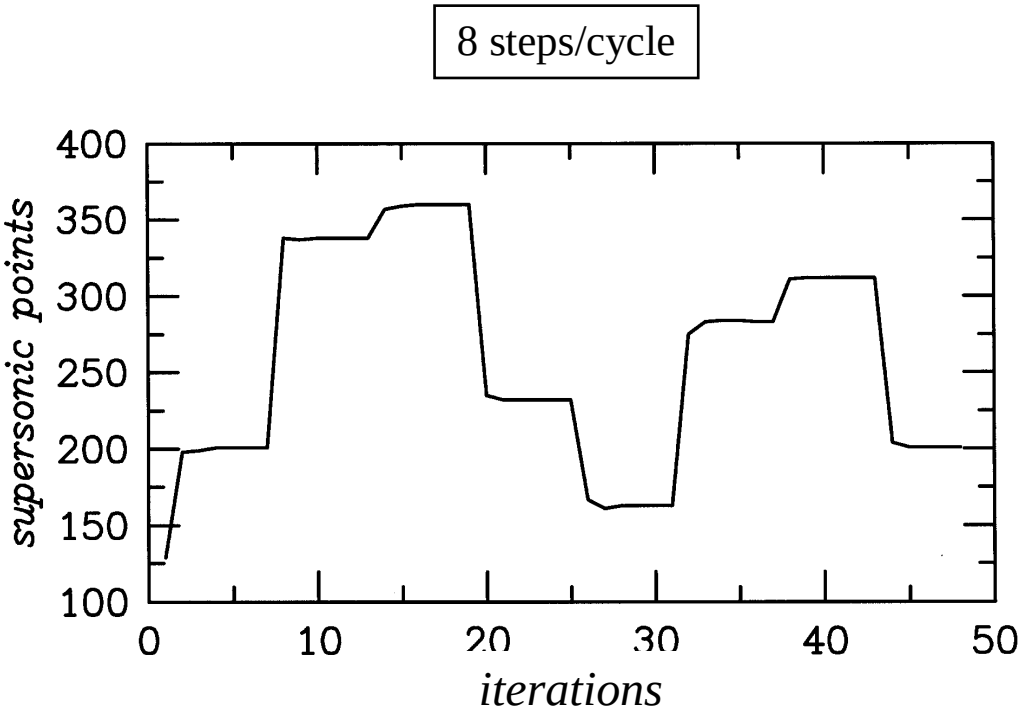

(d) Last cycle of the number of supersonic points.

Figure 4 – Concluded.

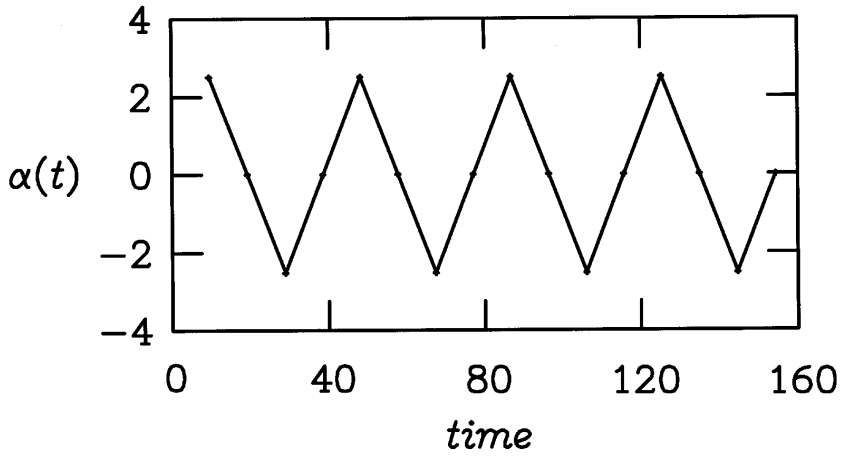

(a) Forced harmonic pitching for four cycles of motion.

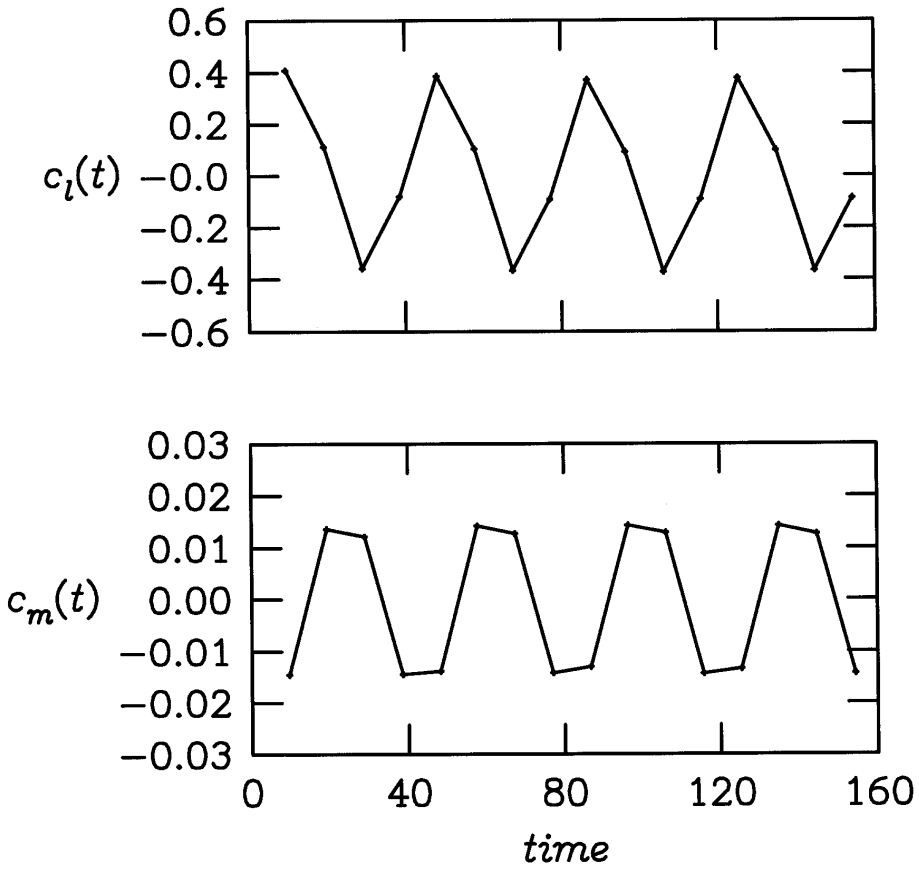

(b) Lift and moment coefficient responses.

Figure 5 – Iterative multigrid calculation using 4 steps per cycle of motion for the NACA 0012 airfoil oscillating harmonically in pitch about the quarter chord at M_∞ = 0.755, α_0 = 0.016°, α_1 = 2.51°, and k = 0.0814.

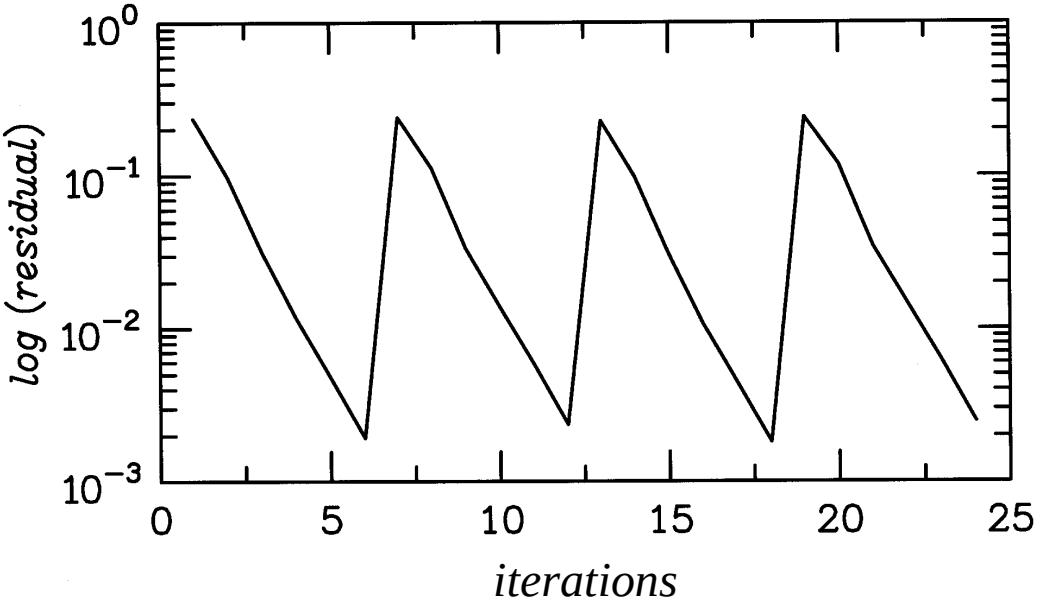

(c) Last cycle of the iterative multigrid residual history.

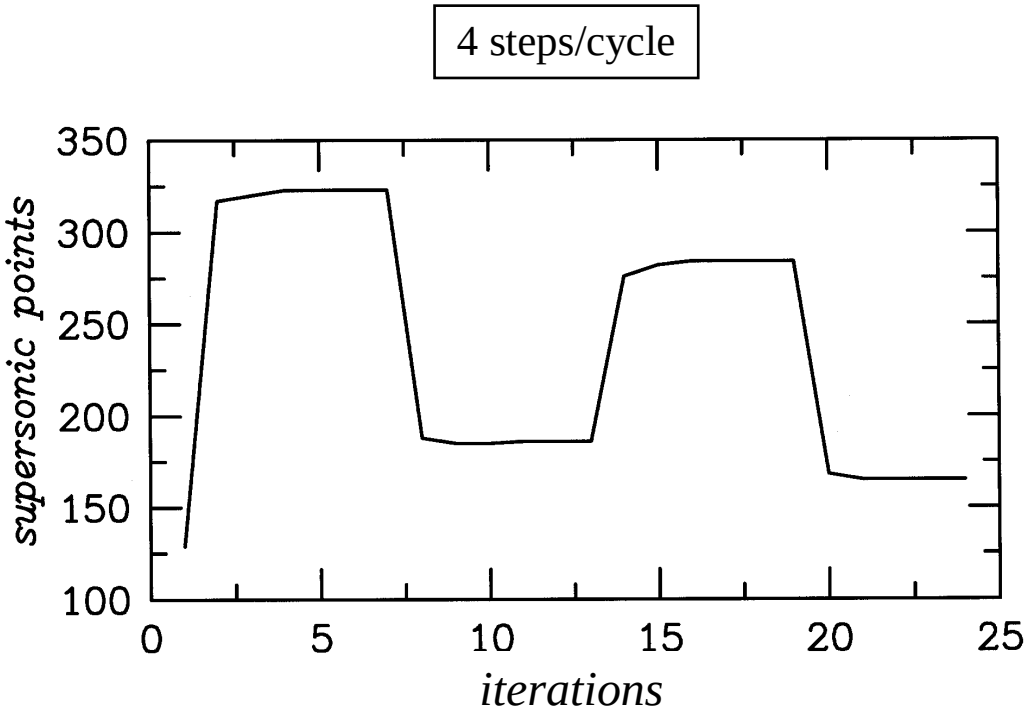

(d) Last cycle of the number of supersonic points.

Figure 5 – Concluded.

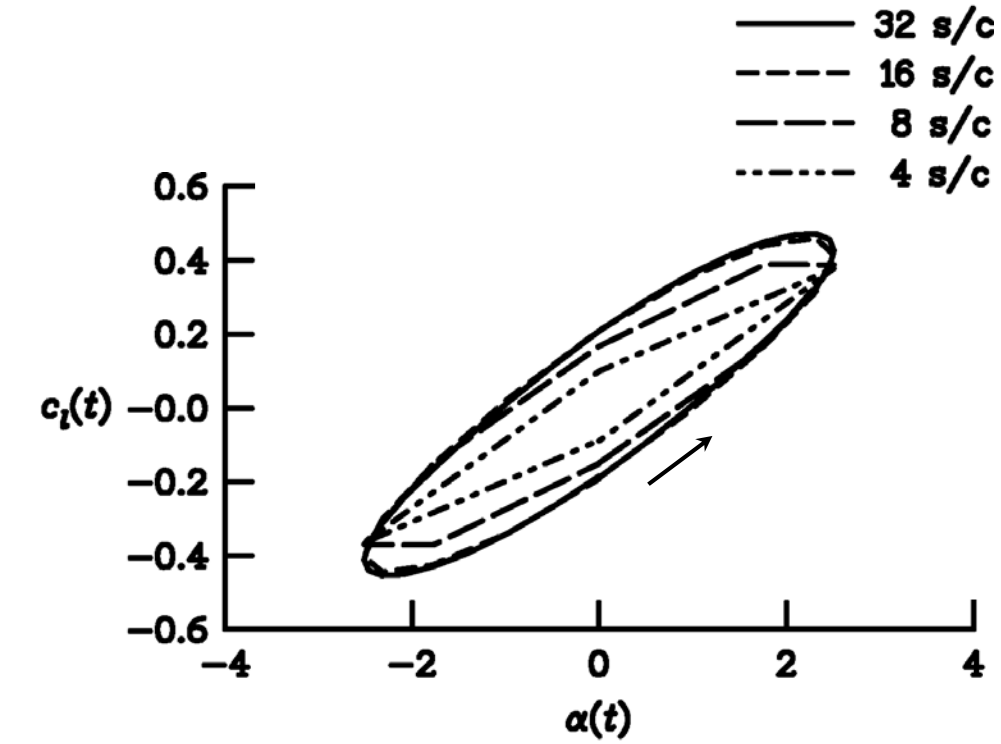

(a) Lift coefficient.

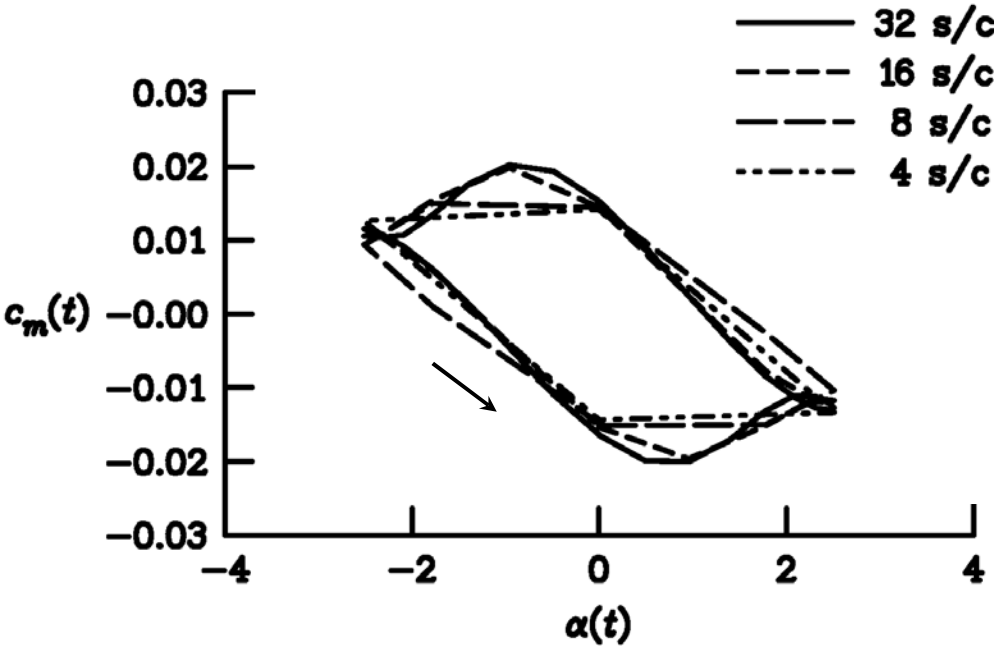

(b) Moment coefficient.

Figure 6 – Effects of step size on the lift and moment coefficient responses in the last (fourth) cycle of motion for the NACA 0012 airfoil oscillating harmonically in pitch about the quarter chord at M_∞ = 0.755, α_0 = 0.016°, α_1 = 2.51°, and k = 0.0814.

$$\delta(t) = 0.1\left[10 - 15\left(\frac{t}{15}\right) + 6\left(\frac{t}{15}\right)^2\right]\left(\frac{t}{15}\right)^3 \qquad for \quad 0 \le t \le 15$$

$$\delta(t) = 0.1\left[10 - 15\left(\frac{30-t}{15}\right) + 6\left(\frac{30-t}{15}\right)^2\right]\left(\frac{30-t}{15}\right)^3 \qquad for \quad 15 \le t \le 30$$

$$\delta(t) = 0 \qquad for \quad t \ge 30$$

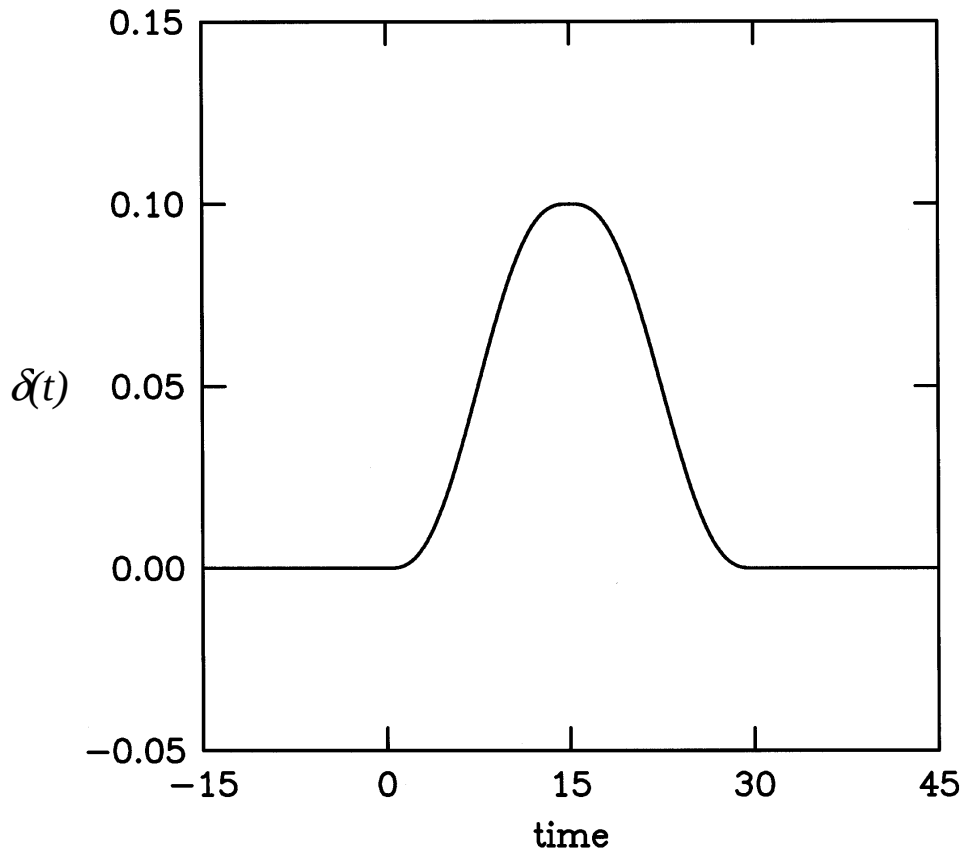

Figure 7 – Definition of midchord thickness as a function of time for the thickening-thinning parabolic arc airfoil.

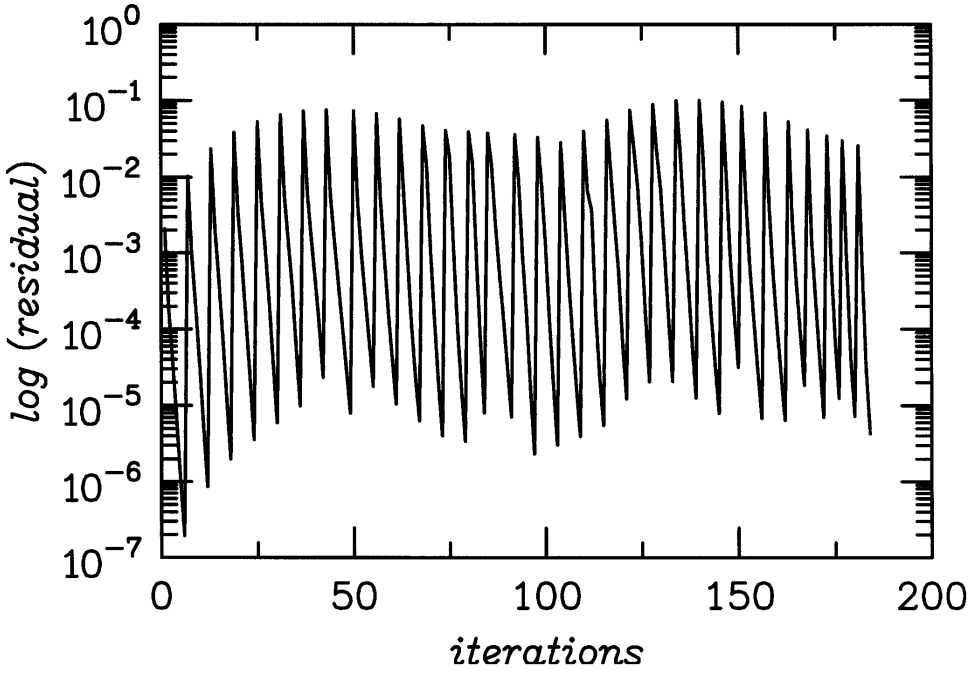

(a) Residual history.

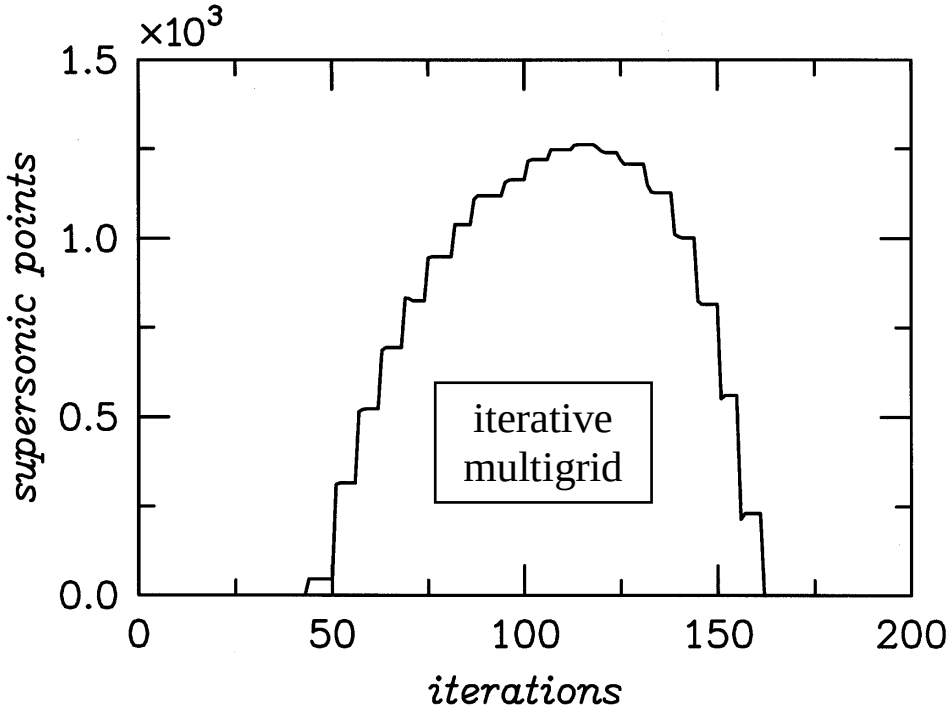

(b) Number of supersonic points.

Figure 8 – Iterative multigrid calculation for the thickening-thinning parabolic arc airfoil problem at M_∞ = 0.85 (32 total time steps).

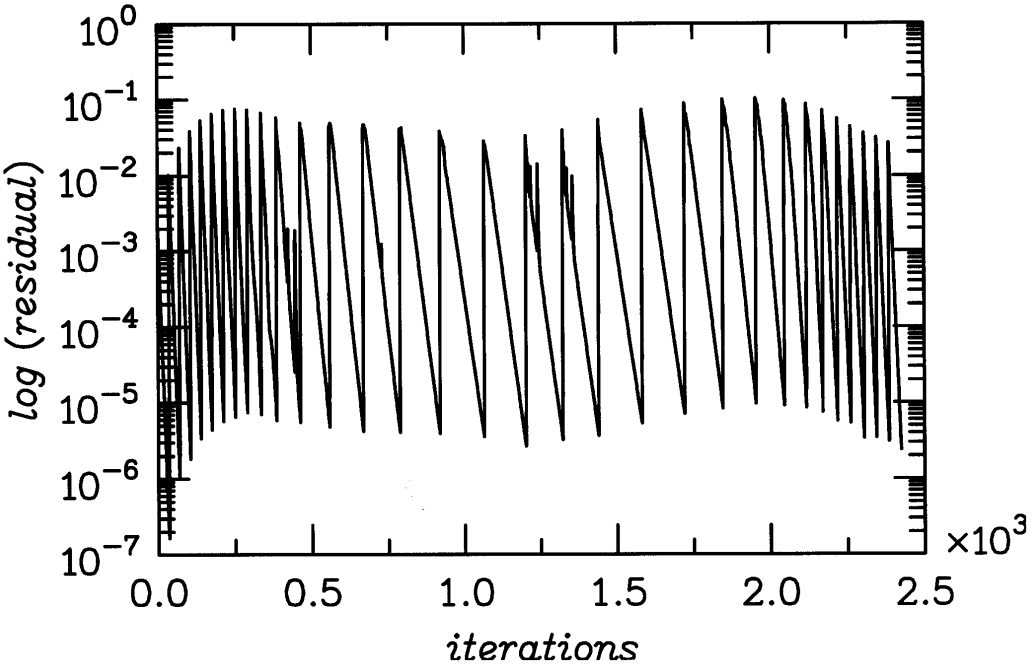

(a) Residual history.

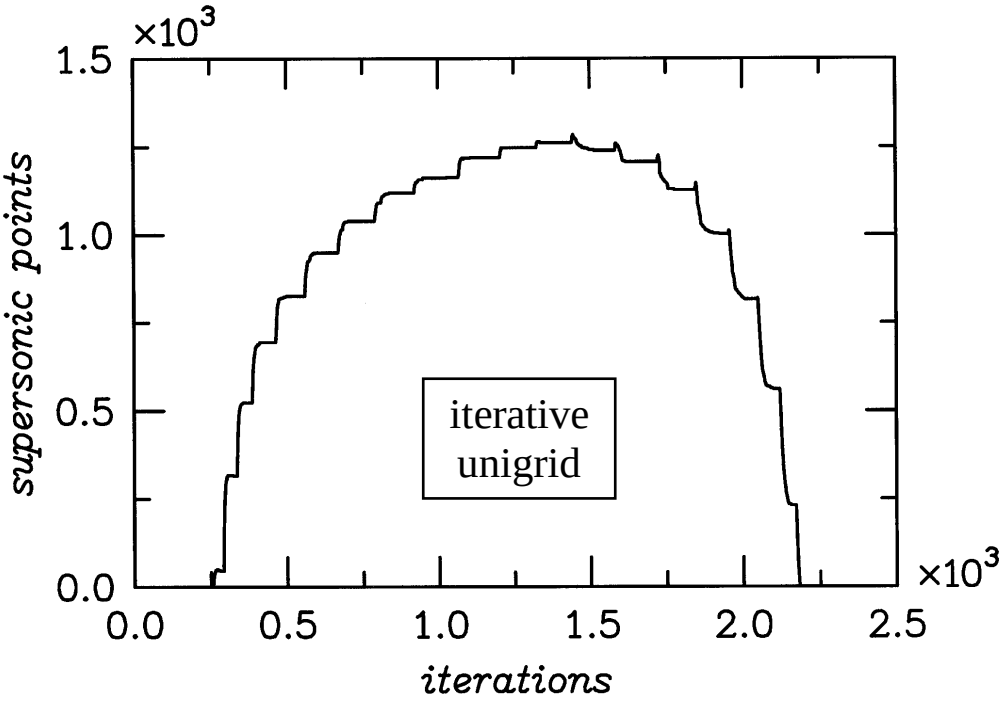

(b) Number of supersonic points.

Figure 9 – Iterative unigrid calculation for the thickening-thinning parabolic arc airfoil problem at M_∞ = 0.85 (32 total time steps).

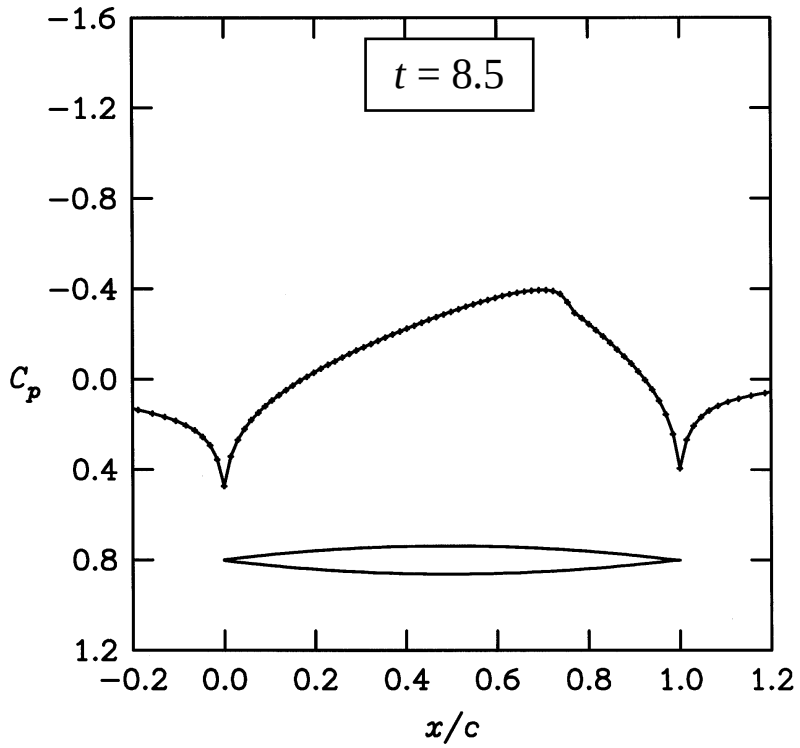

(a) Pressure coefficient distribution.

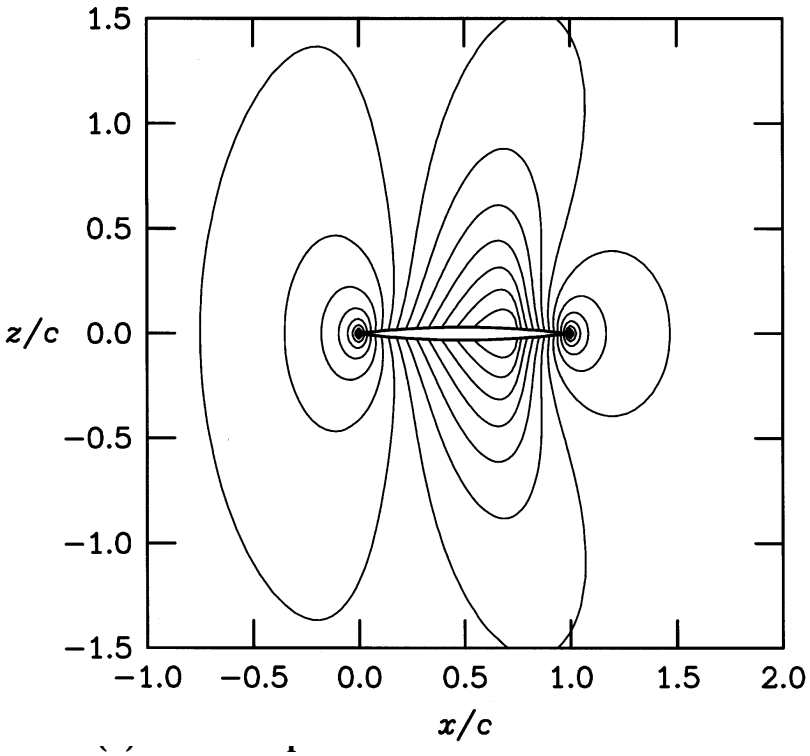

Figure 10 – Instantaneous results at t = 8.5 from the iterative multigrid calculation of the thickening-thinning parabolic arc airfoil at M_∞ = 0.85.

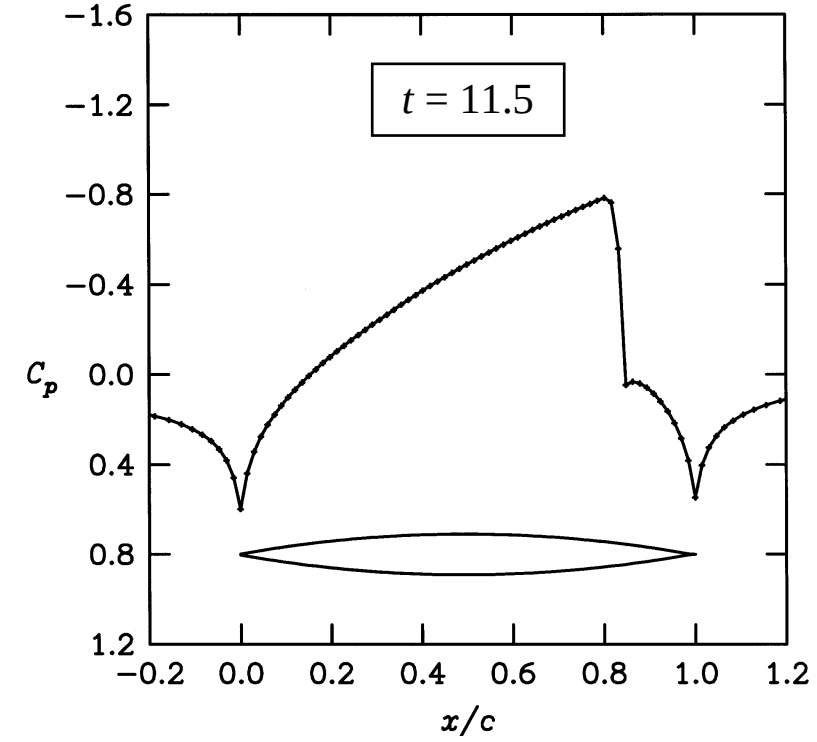

(a) Pressure coefficient distribution.

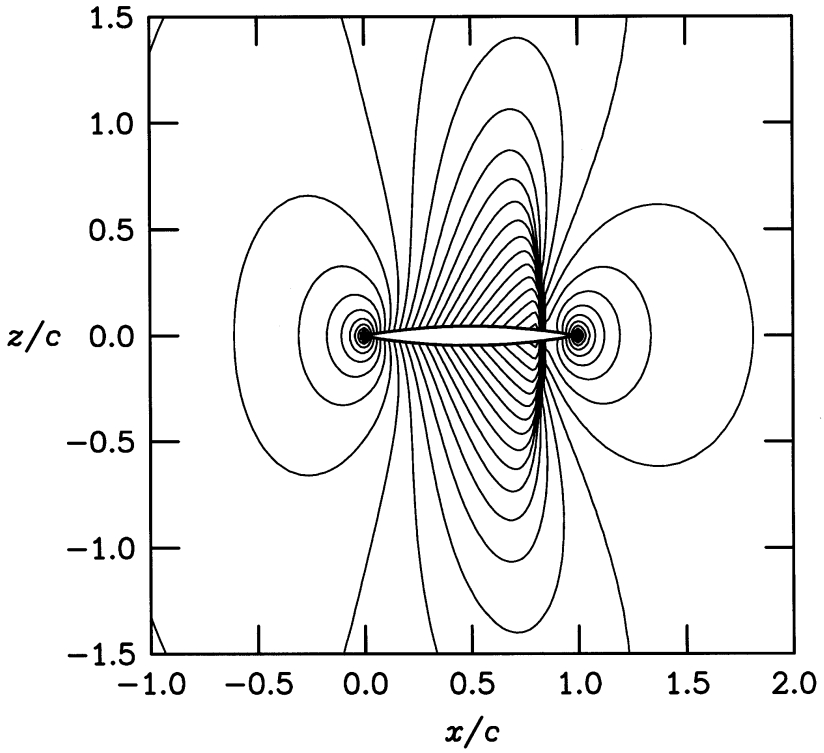

(b) Near field pressure coefficient contour lines.

Figure 11 – Instantaneous results at t = 11.5 from the iterative multigrid calculation of the thickening-thinning parabolic arc airfoil at M_∞ = 0.85.

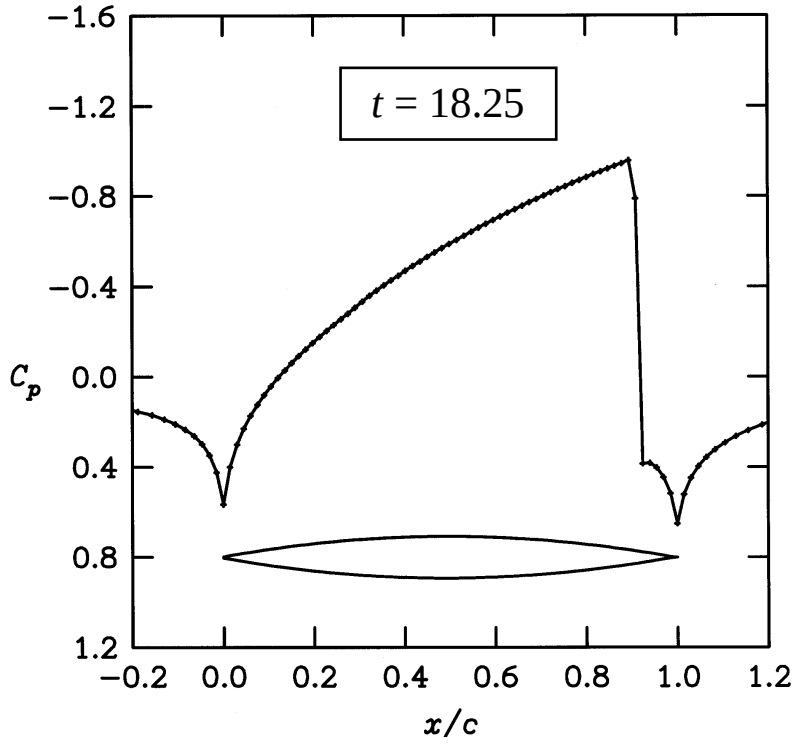

(a) Pressure coefficient distribution.

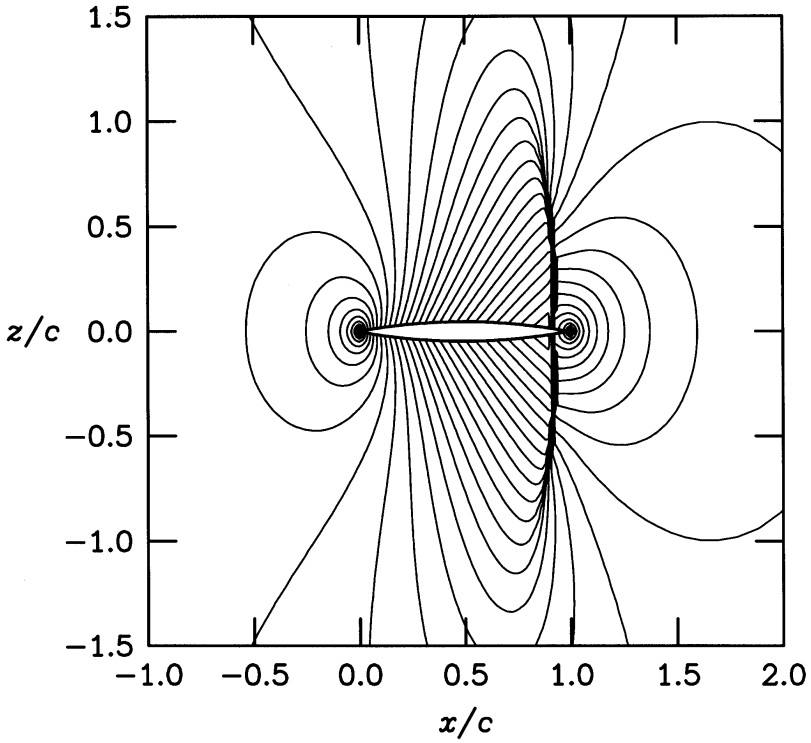

(b) Near field pressure coefficient contour lines.

Figure 12 – Instantaneous results at t = 18.25 from the iterative multigrid calculation of the thickening-thinning parabolic arc airfoil at M_∞ = 0.85.

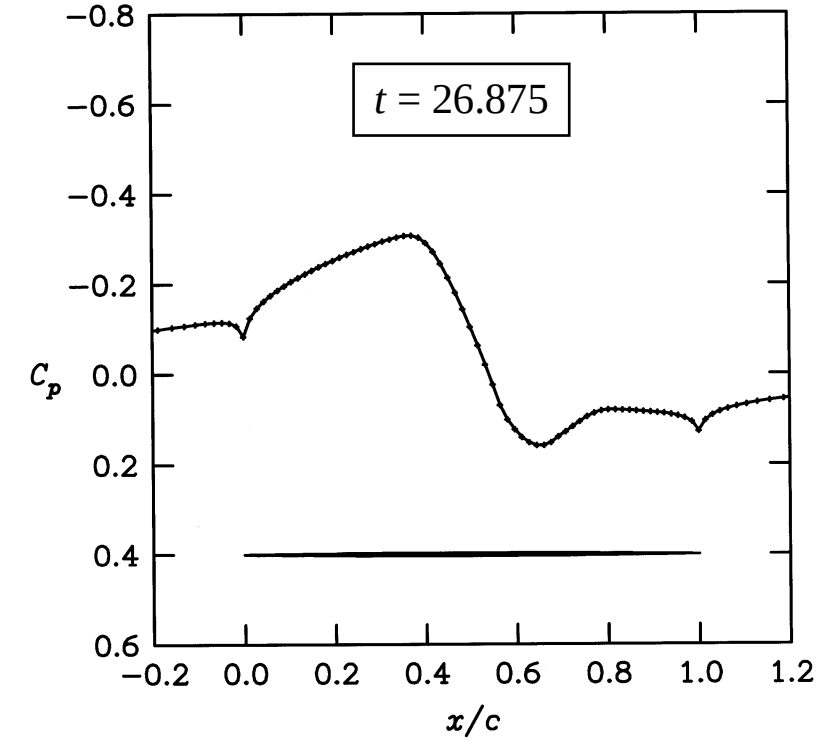

(a) Pressure coefficient distribution.

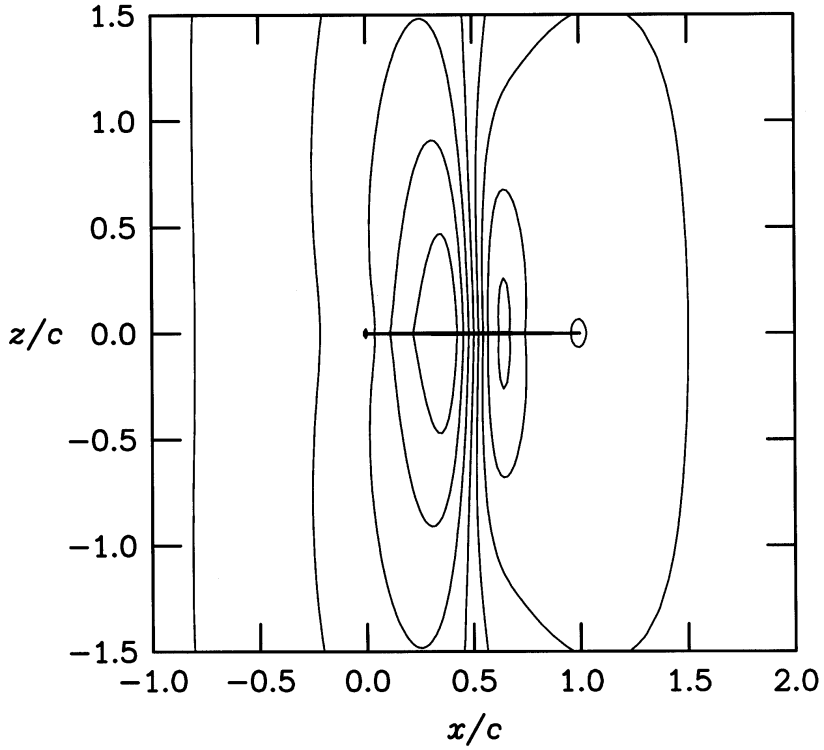

(b) Near field pressure coefficient contour lines.

Figure 13 – Instantaneous results at t = 26.875 from the iterative multigrid calculation of the thickening-thinning parabolic arc airfoil at M_∞ = 0.85.

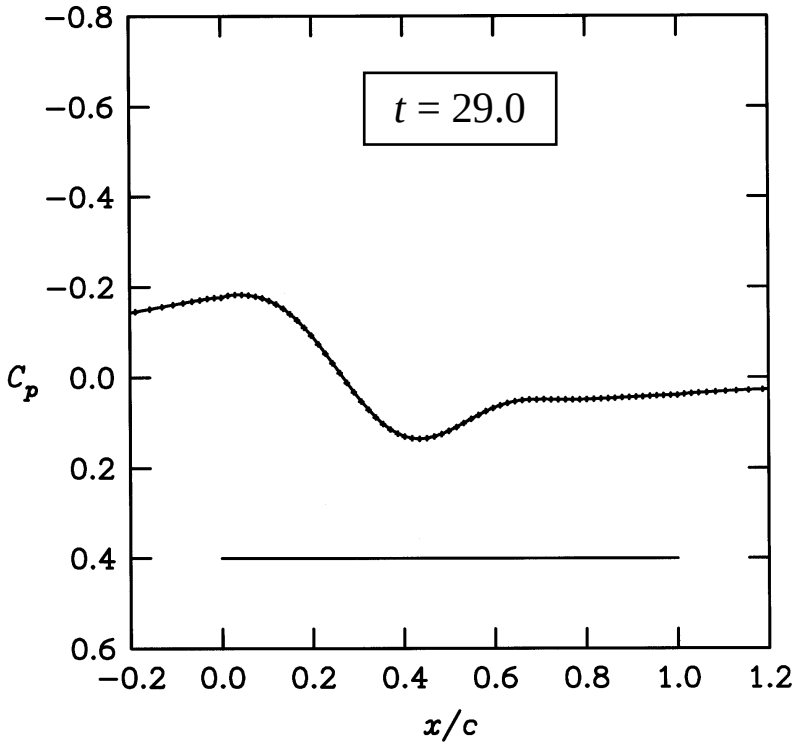

(a) Pressure coefficient distribution.

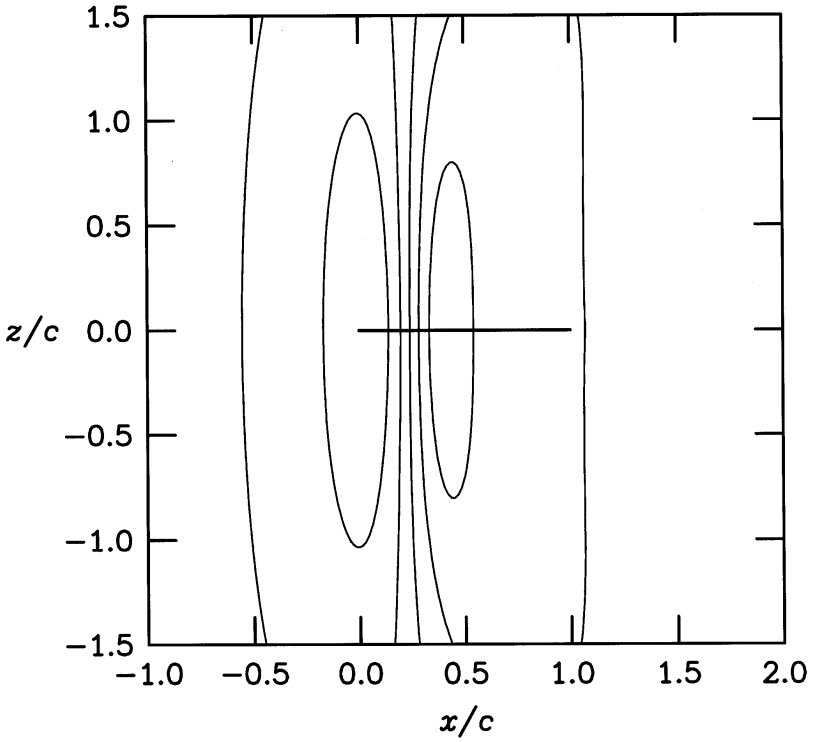

(b) Near field pressure coefficient contour lines.

Figure 14 – Instantaneous results at t = 29.0 from the iterative multigrid calculation of the thickening-thinning parabolic arc airfoil at M_∞ = 0.85.

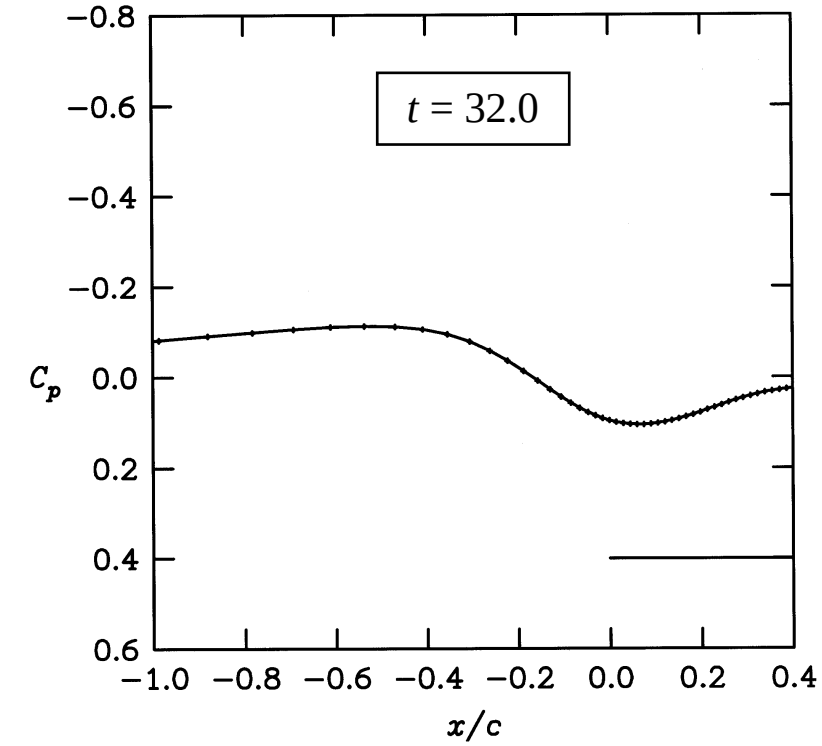

(a) Pressure coefficient distribution.

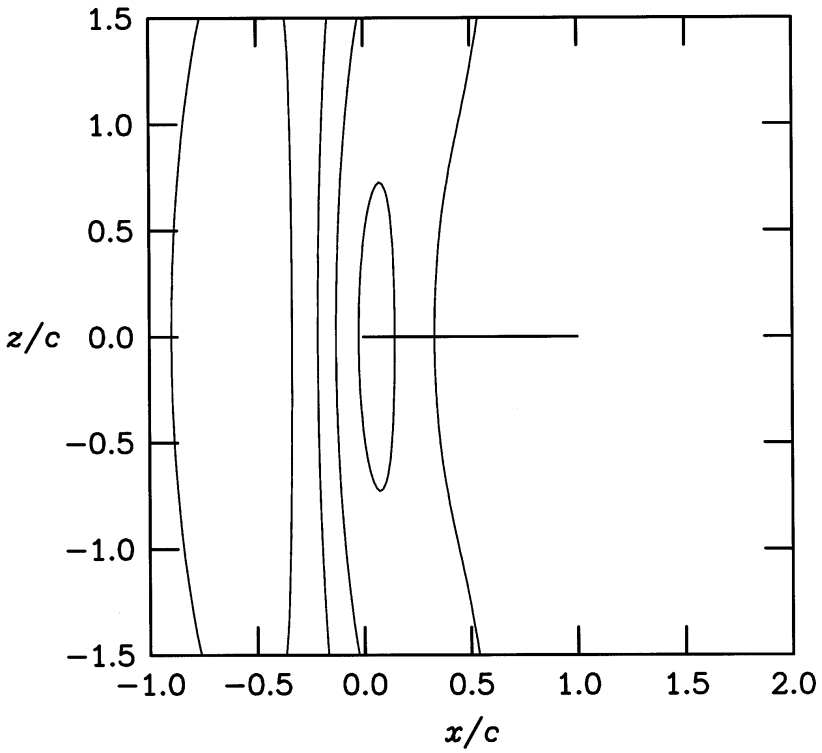

(b) Near field pressure coefficient contour lines.

Figure 15 – Instantaneous results at t = 32.0 from the iterative multigrid calculation of the thickening-thinning parabolic arc airfoil at M_∞ = 0.85.

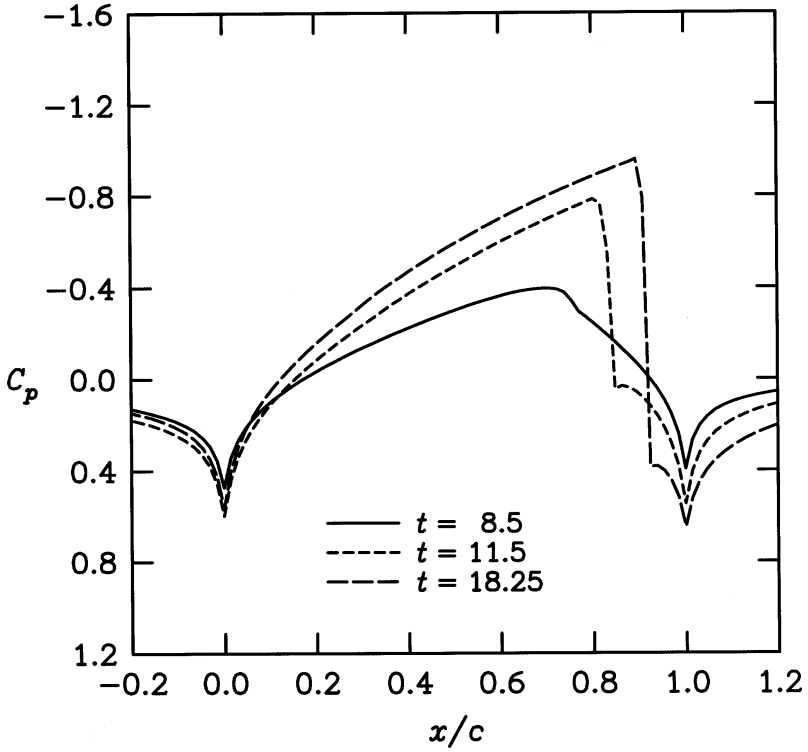

(a) ASP3D pressure coefficient distributions at t = 8.5, 11.5, and 18.25.

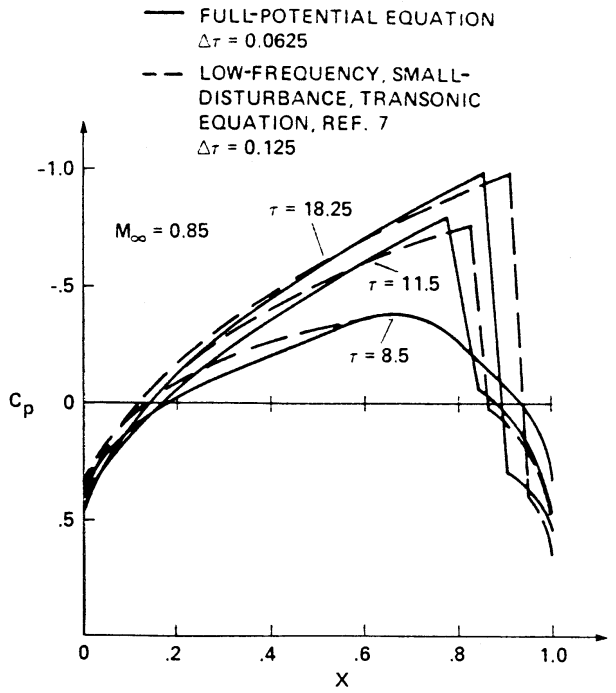

(b) Corresponding FP and TSD pressure coefficients reported by Goorjian.[35]

Figure 16 – Pressure coefficient comparisons for the thickening-thinning parabolic arc airfoil at M_∞ = 0.85.

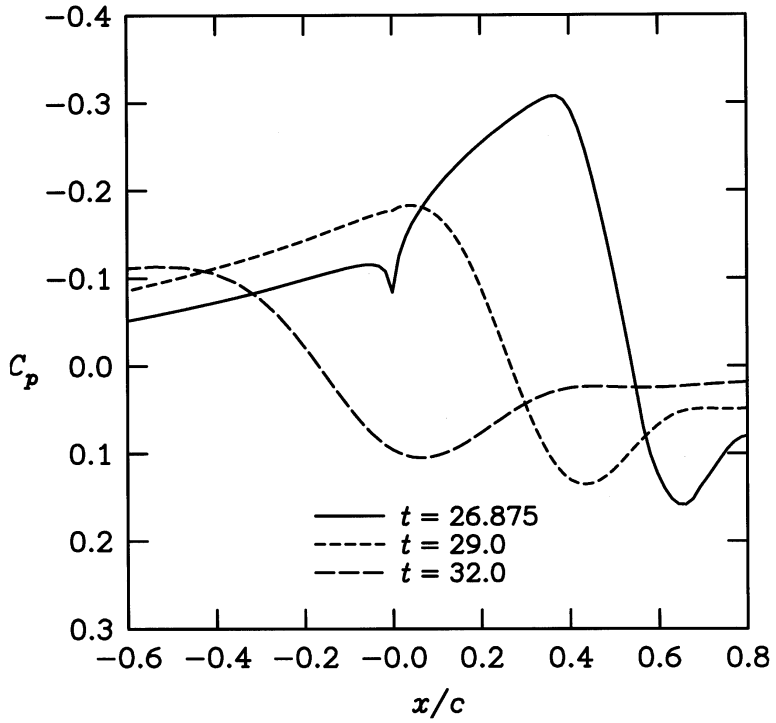

(c) ASP3D pressure coefficient distributions at t = 26.875, 29.0, and 32.0.

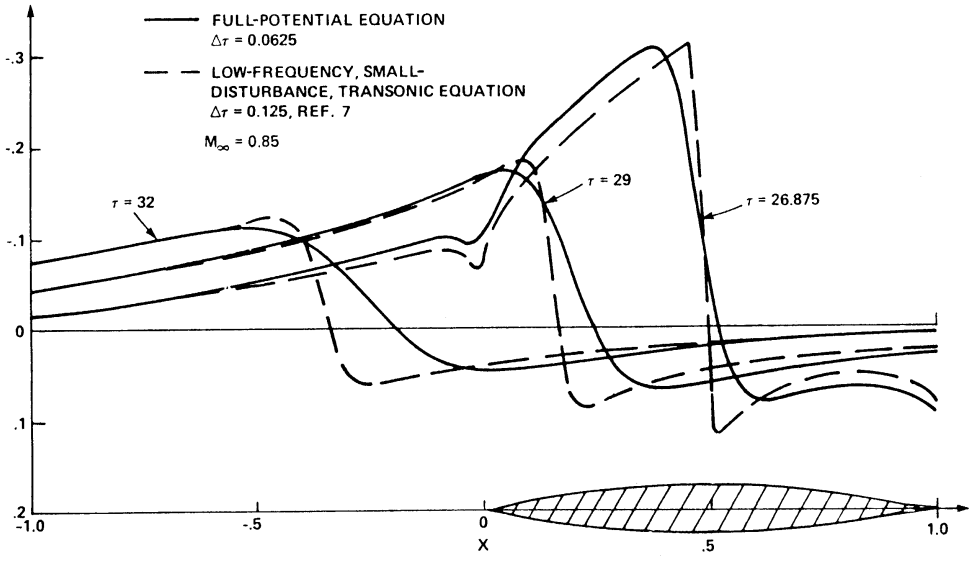

(d) Corresponding FP and TSD pressure coefficients reported by Goorjian.[35]

Figure 16 – Concluded.

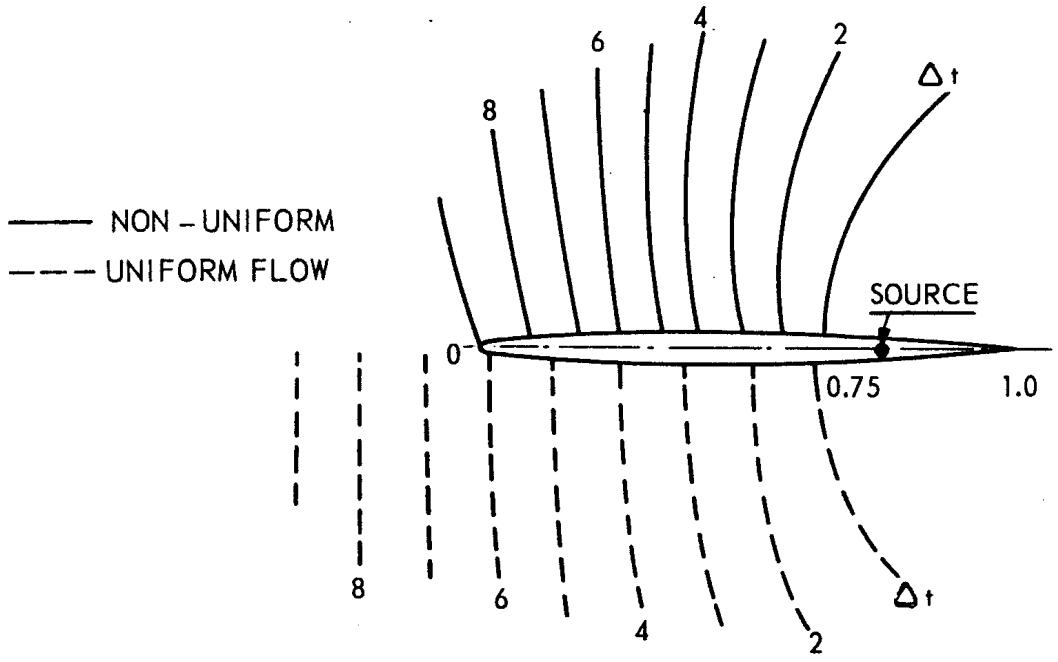

(a) Subsonic freestream Mach number of M_∞ = 0.8.

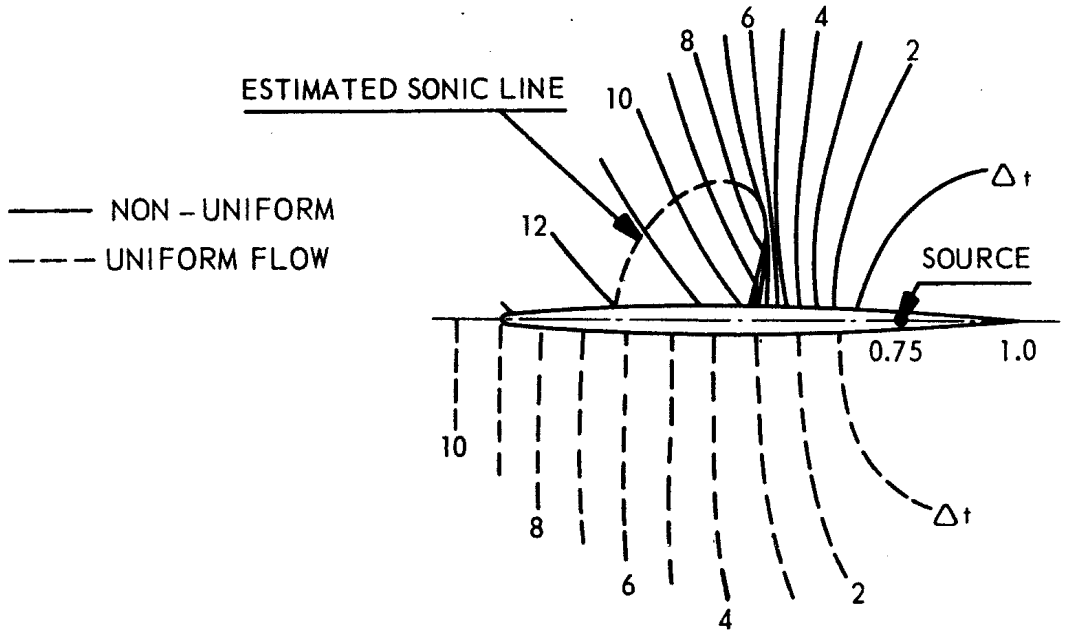

(b) Transonic freestream Mach number of M_∞ = 0.875.

Figure 17 – NLR diagrams[36] of upstream propagation of disturbance wave fronts generated by a source at the control surface hinge line.

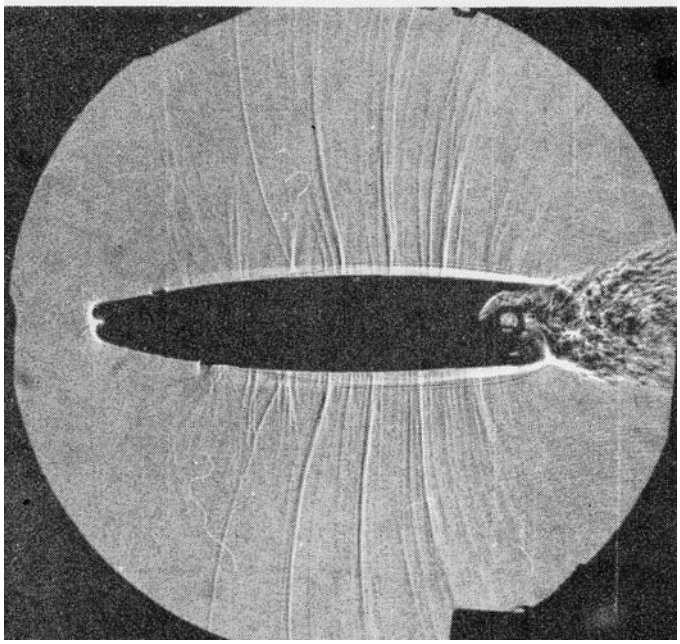

(a) Subsonic freestream Mach number of M_∞ = 0.8.

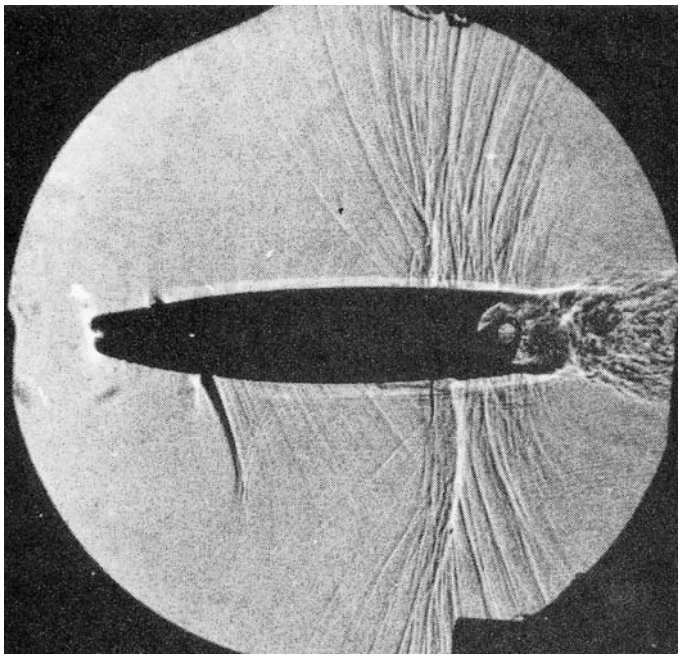

(b) Transonic freestream Mach number of M_∞ = 0.875.

Figure 18 – NLR shadowgraph (spark exposure) photographs[36] showing upstream wave propagation.

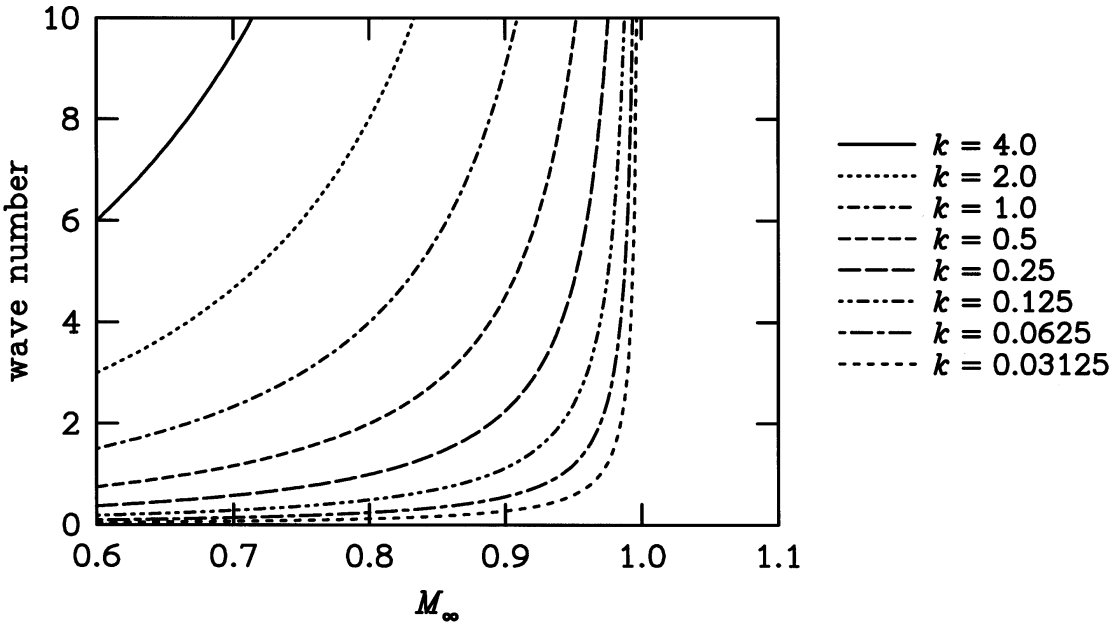

(a) Upstream propagation.

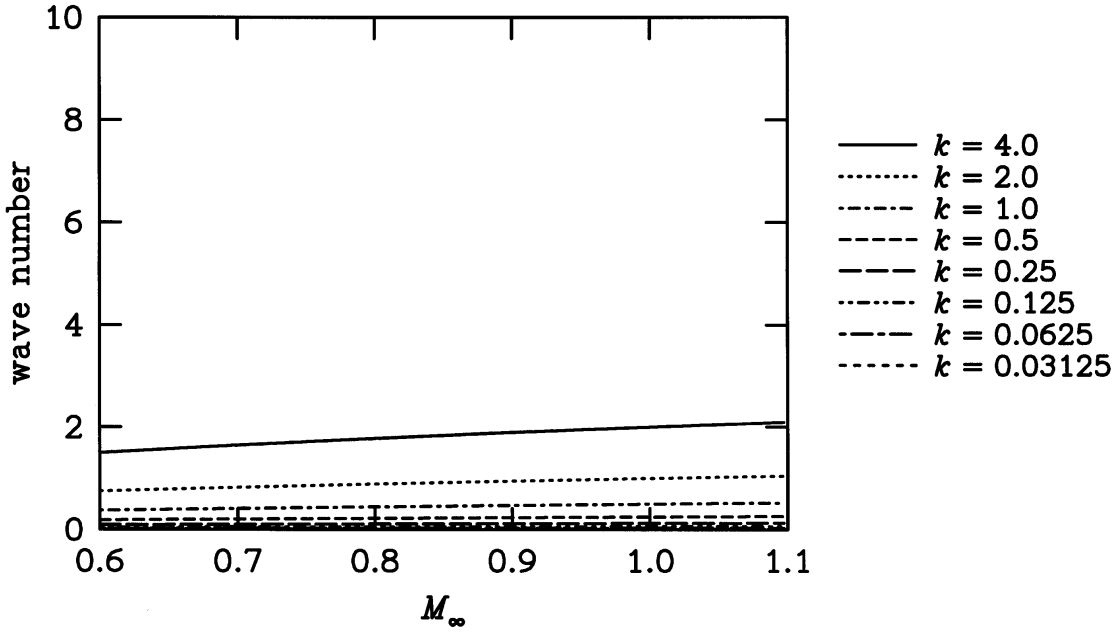

(b) Downstream propagation.

Figure 19 – Linear theory wave propagation characteristics as a function of Mach number for a range of values of reduced frequency *k*.

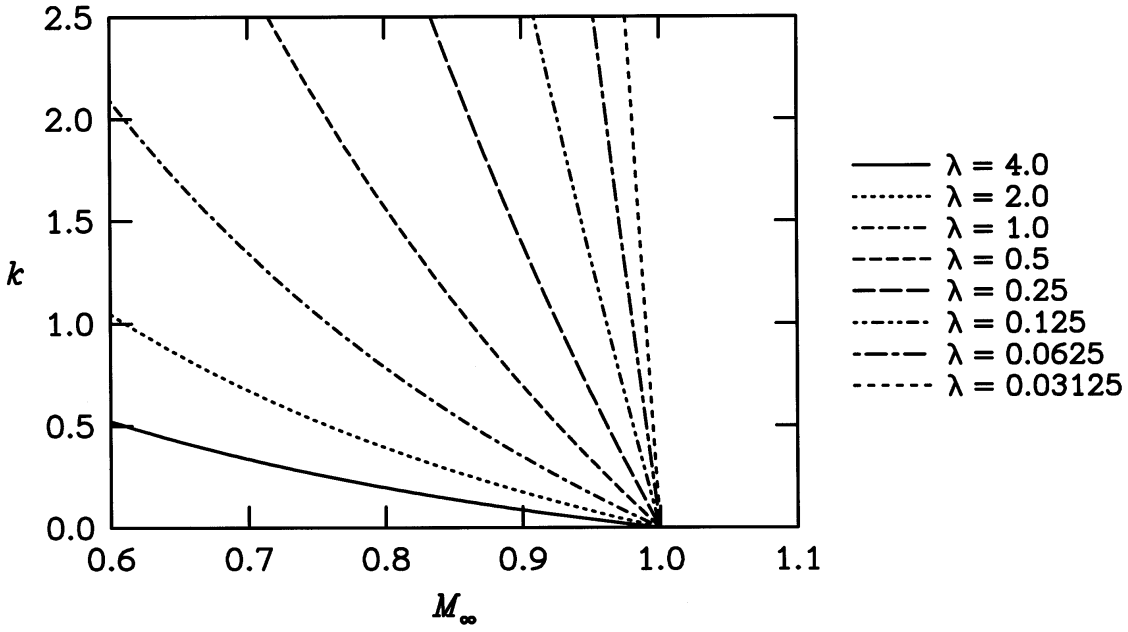

(a) Upstream propagation.

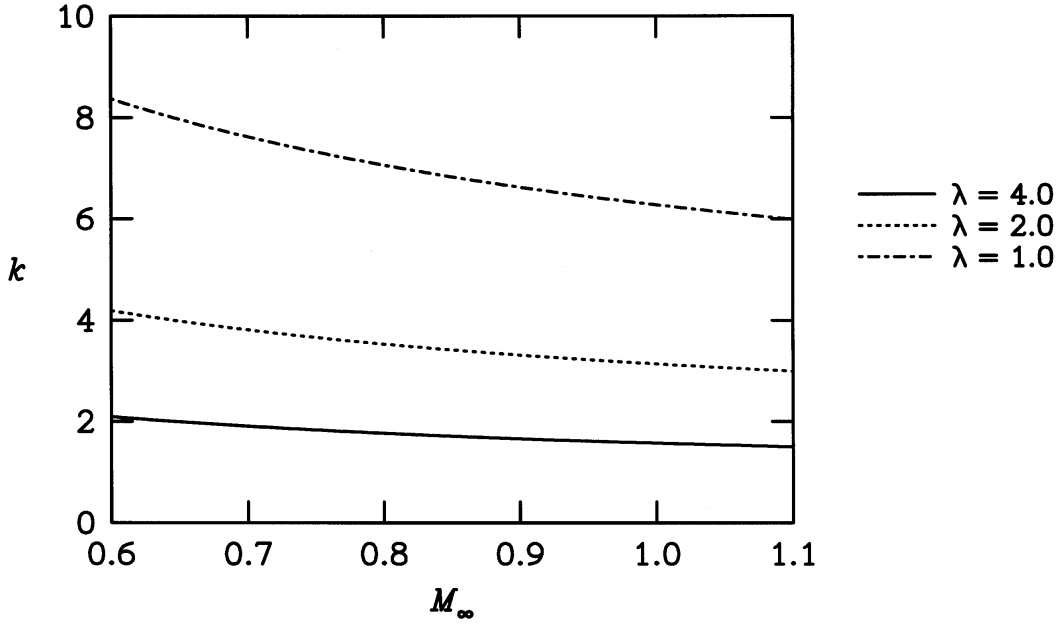

(b) Downstream propagation.

Figure 20 – Linear theory wave propagation characteristics as a function of Mach number for various values of wavelength λ.

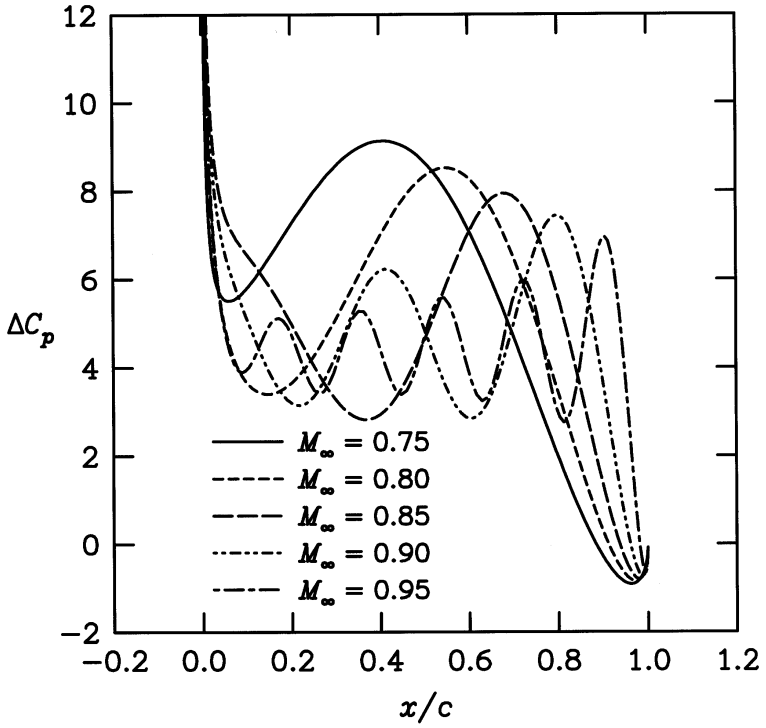

(a) Real part.

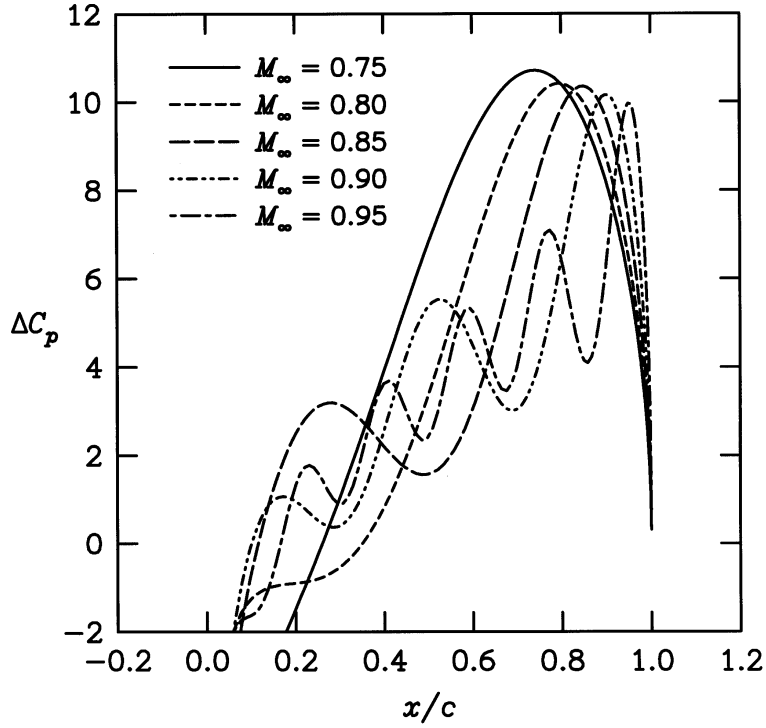

(b) Imaginary part.

Figure 21 - Effects of Mach number on linear theory lifting pressure coefficient distributions for a flat plate airfoil oscillating about the leading edge at *k* = 0.9.

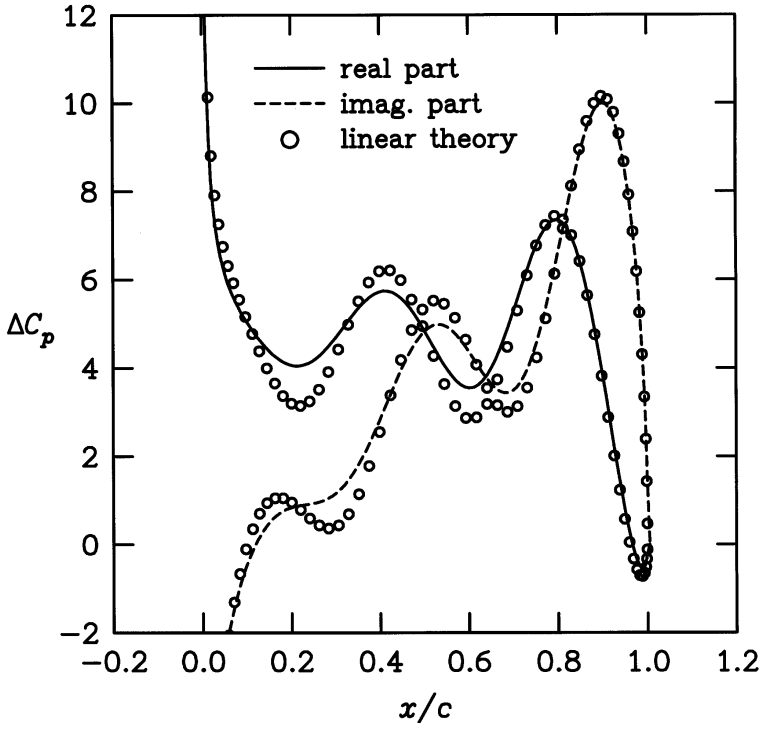

(a) First-order-accurate ϕ_{xt} term.

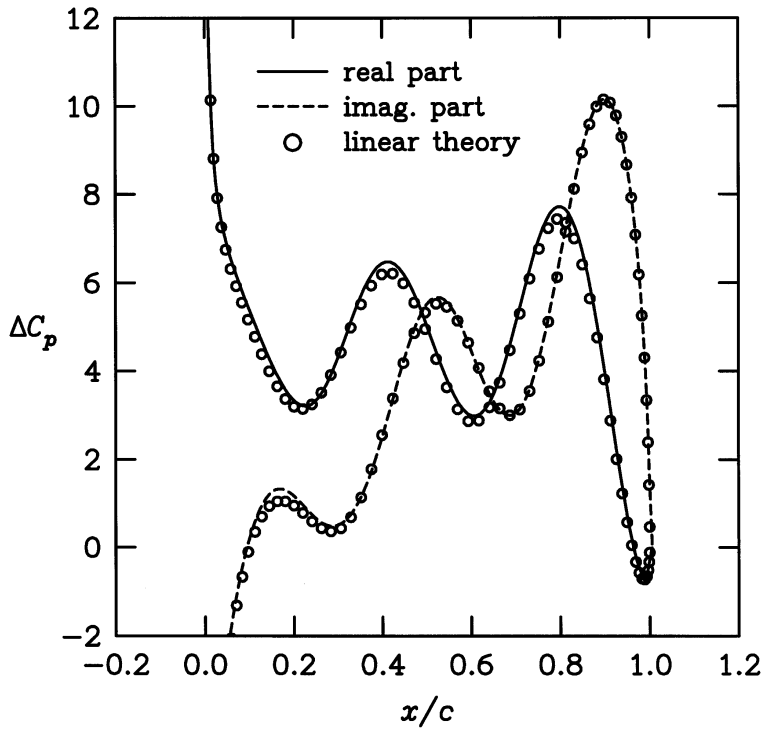

(b) Second-order-accurate ϕ_{xt} term.

Figure 22 – Effects of order of accuracy on ASP3D lifting pressure coefficient distributions for a flat plate airfoil oscillating about the l. e. at k = 0.9 and M_∞ = 0.9.

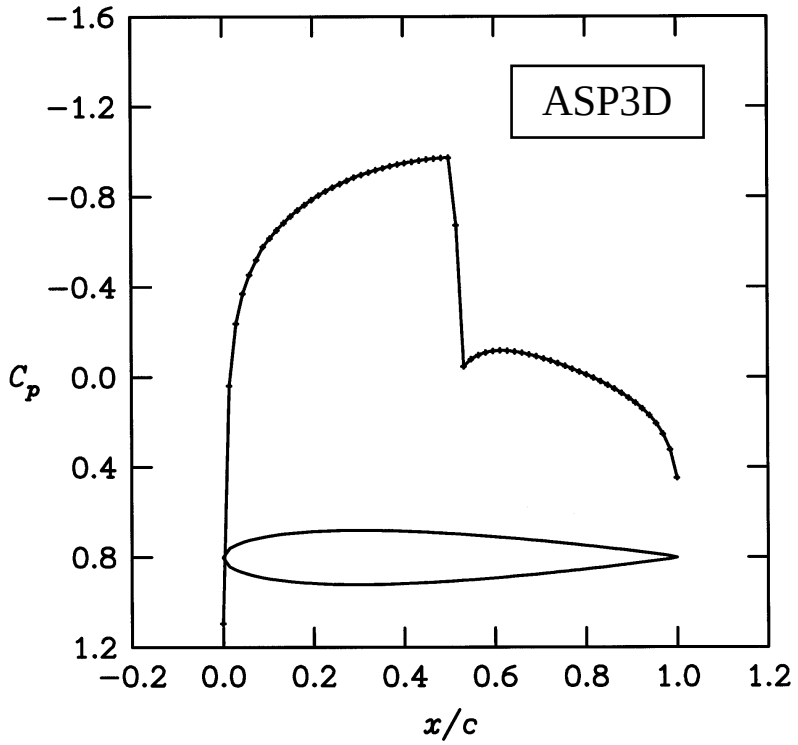

(a) ASP3D pressure distribution including entropy and vorticity effects.

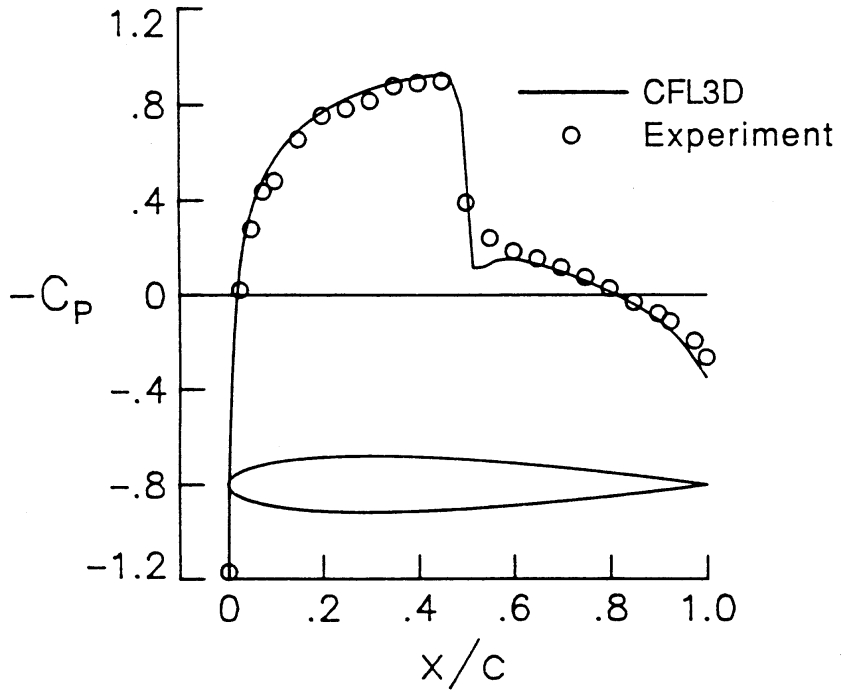

(b) Euler (CFL3D) pressure distribution computed by Robinson, et al.[38]

Figure 23 – Steady pressure coefficient distributions for the NACA 0012 airfoil at M_∞ = 0.8 and α_0 = 0°.

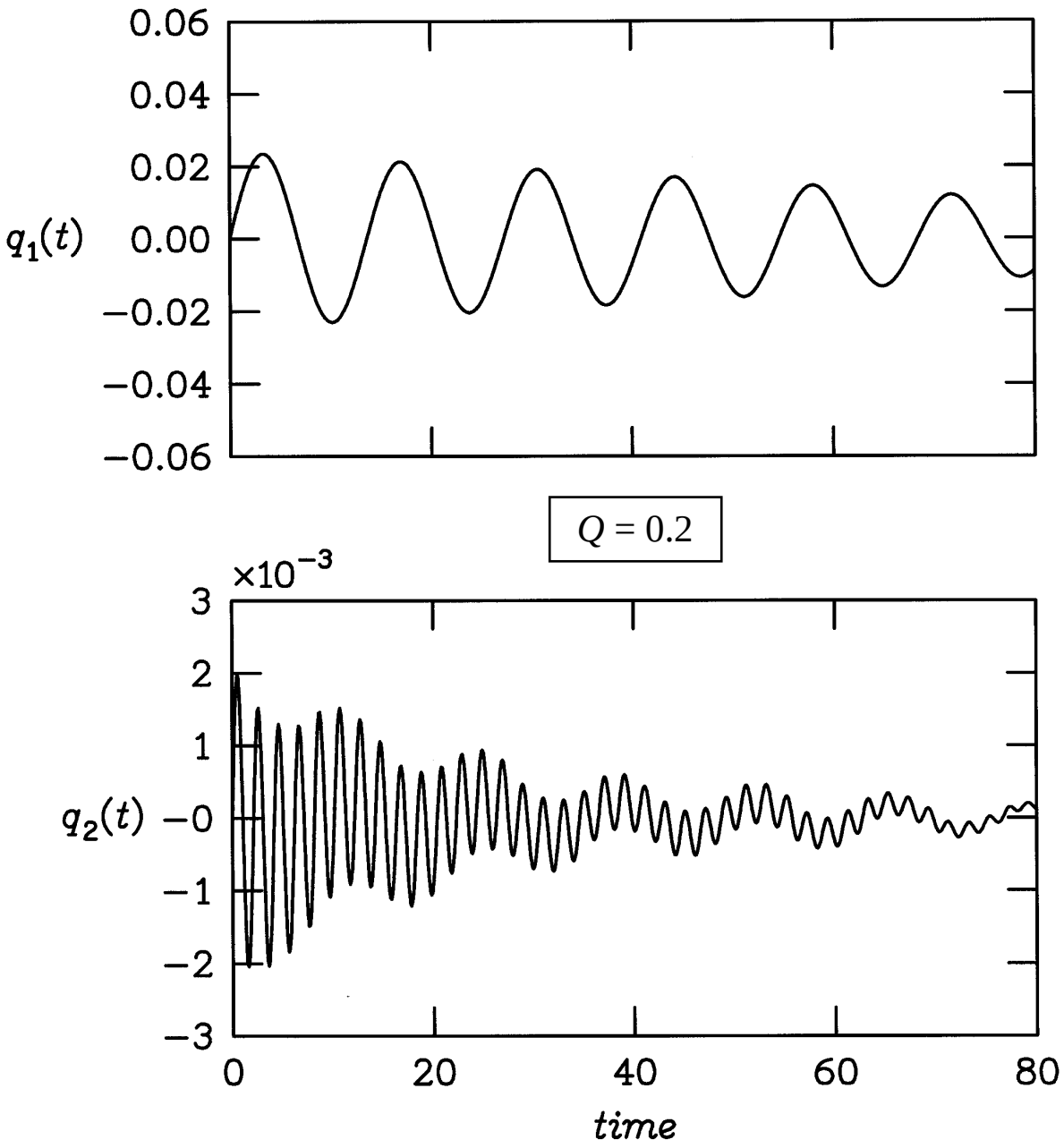

Figure 24 – Generalized displacements corresponding to stable (converging) aeroelastic motion for the NACA 0012 airfoil at $M_\infty = 0.8$, $\alpha_0 = 0°$, and $Q = 0.2$ for the structural parameter values of Isogai Case "A".

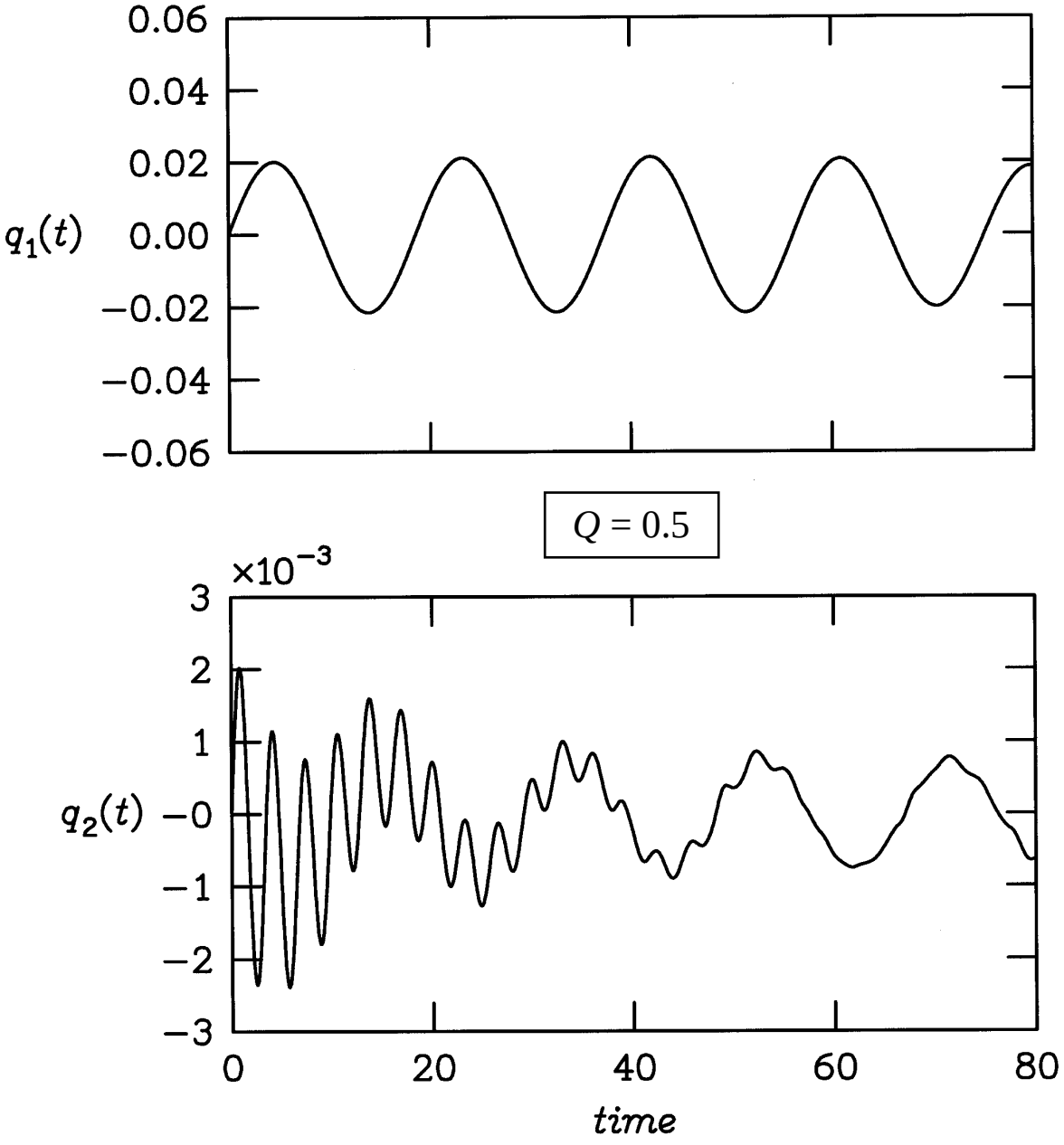

Figure 25 – Generalized displacements corresponding to near-neutrally stable (flutter) aeroelastic motion for the NACA 0012 airfoil at $M_\infty = 0.8$, $\alpha_0 = 0°$, and $Q = 0.5$ for the structural parameter values of Isogai Case "A".

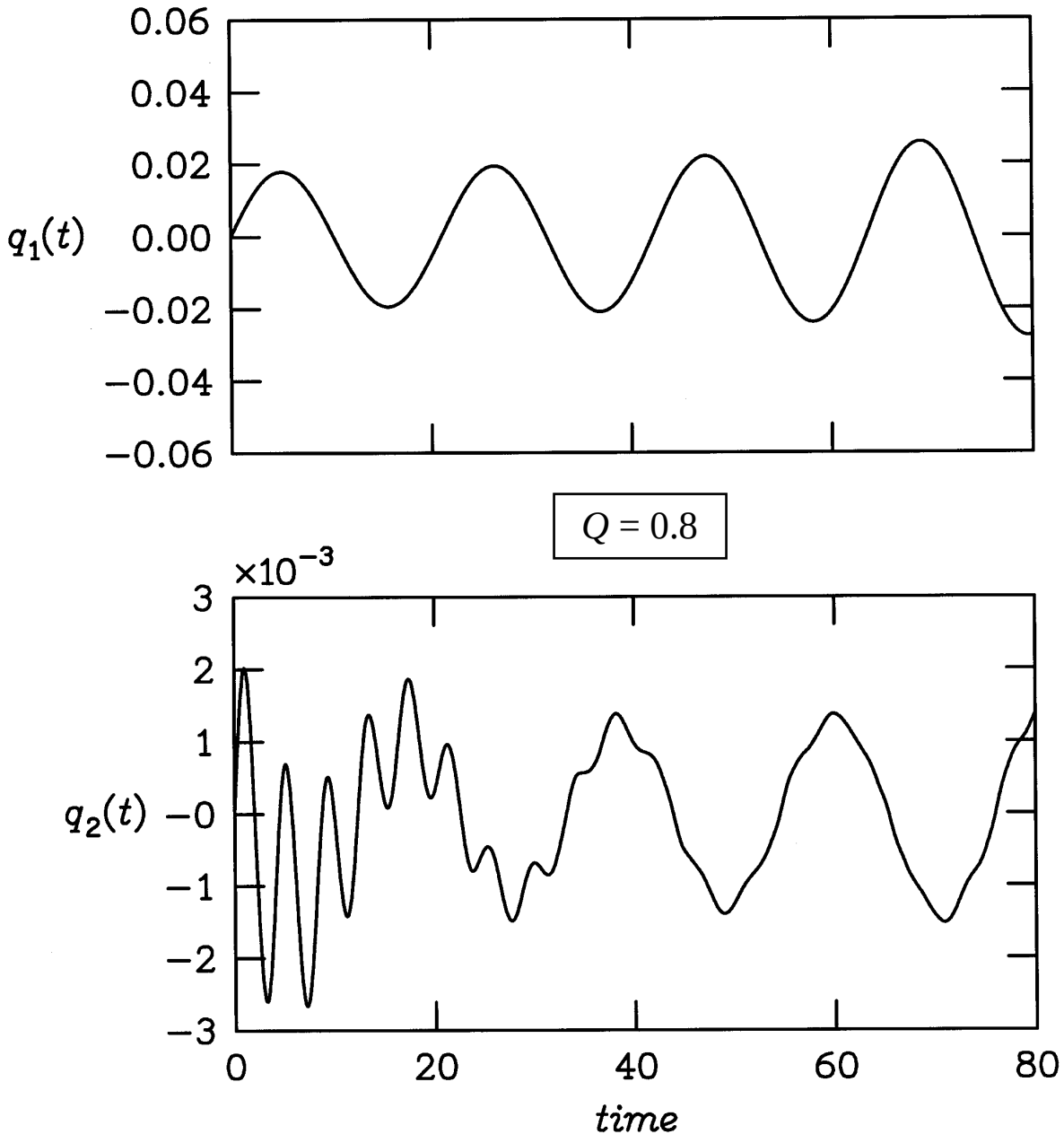

Figure 26 – Generalized displacements corresponding to unstable (diverging) aeroelastic motion for the NACA 0012 airfoil at $M_\infty = 0.8$, $\alpha_0 = 0°$, and $Q = 0.8$ for the structural parameter values of Isogai Case "A".

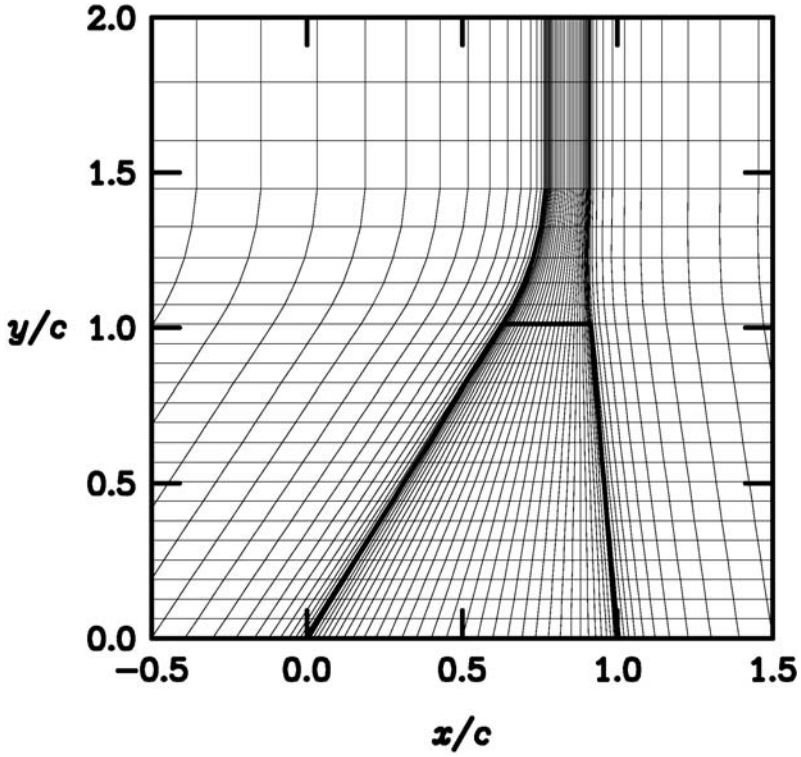

(a) Near field view of 97 x 25 planform mesh.

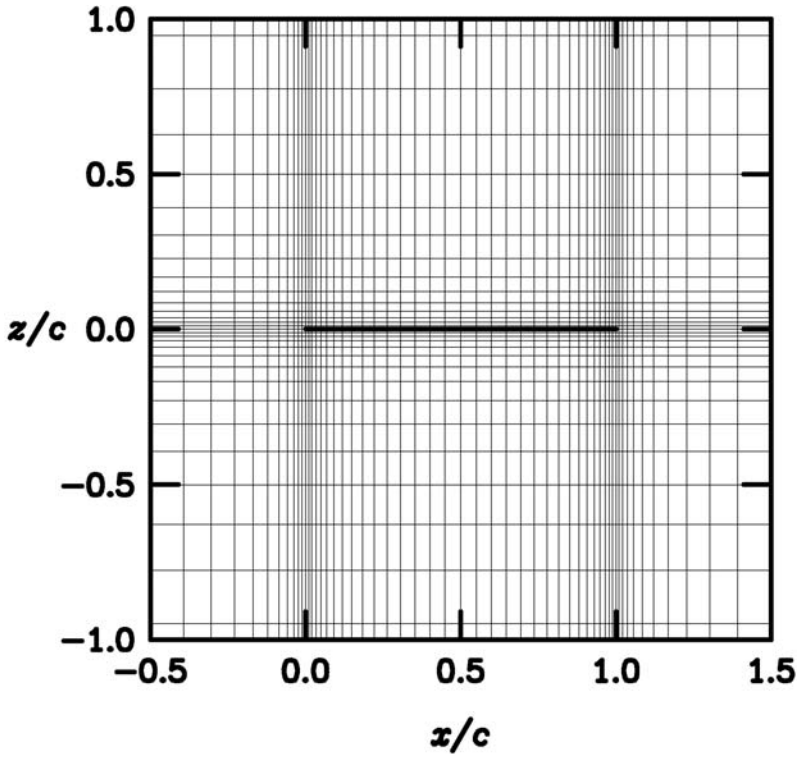

(b) Near field view of 97 x 65 root sectional mesh.

Figure 27 – Finite volume meshes for the F-5 fighter wing.

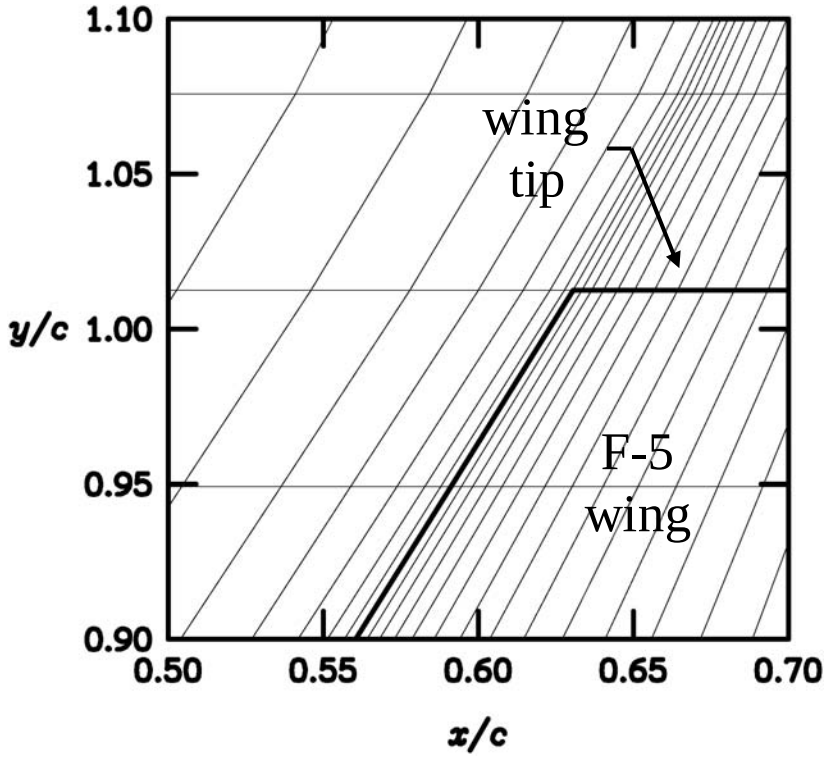

(a) Wing tip leading edge region.

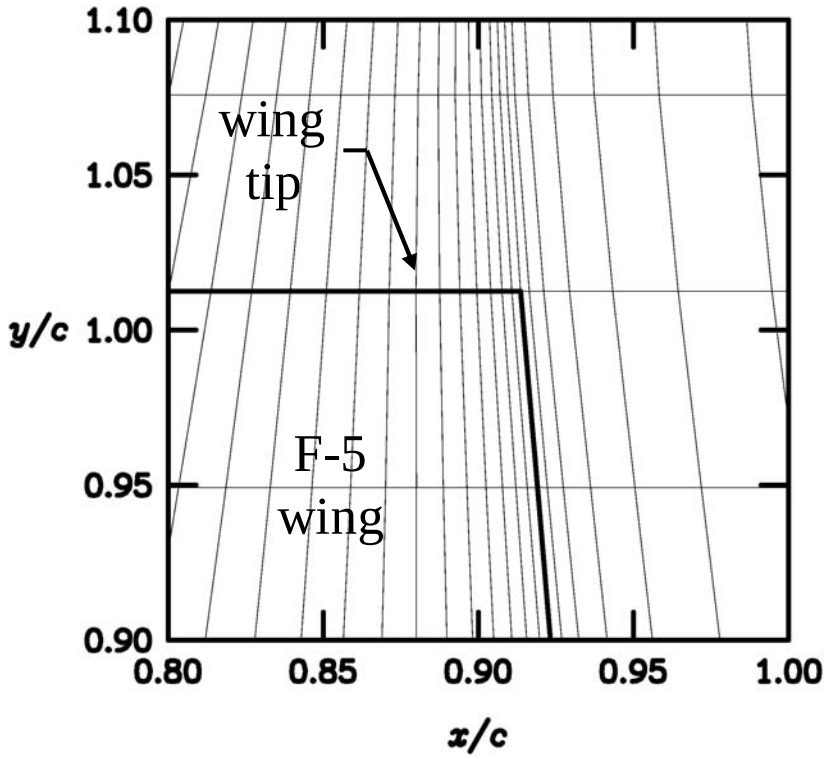

(b) Wing tip trailing edge region.

Figure 28 – Near field views of the planform mesh of the F-5 fighter wing.

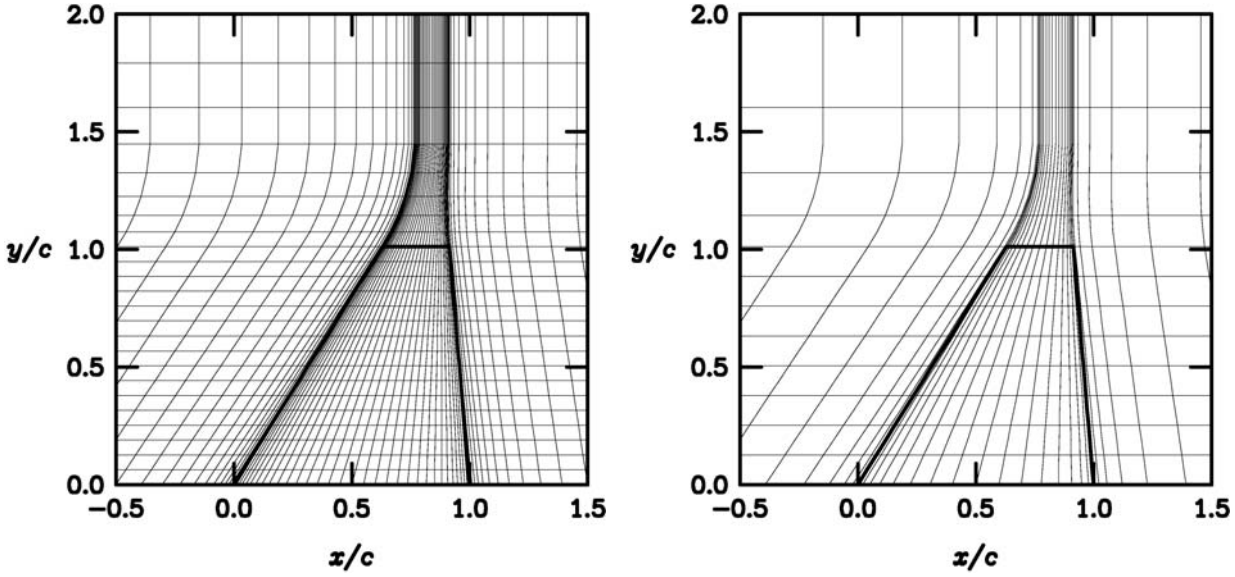

(a) Mesh 4 (97 x 25).

(b) Mesh 3 (49 x 13).

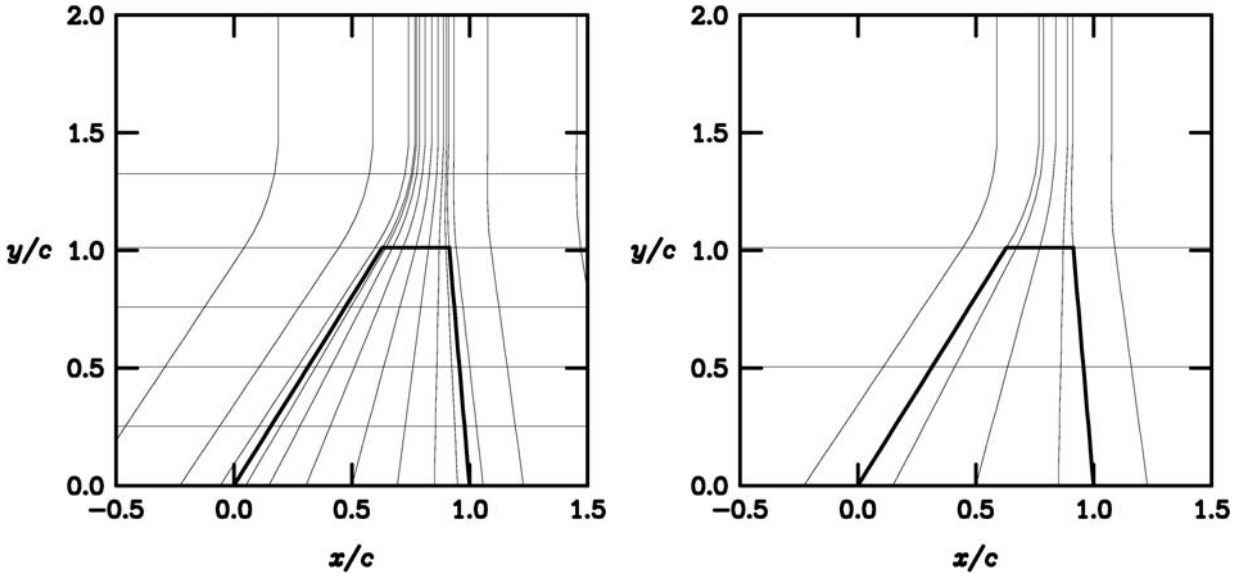

(c) Mesh 2 (25 x 7).

(d) Mesh 1 (13 x 4).

Figure 29 – Near field view of finite volume planform meshes for the F-5 fighter wing for ASP3D multigrid calculations.

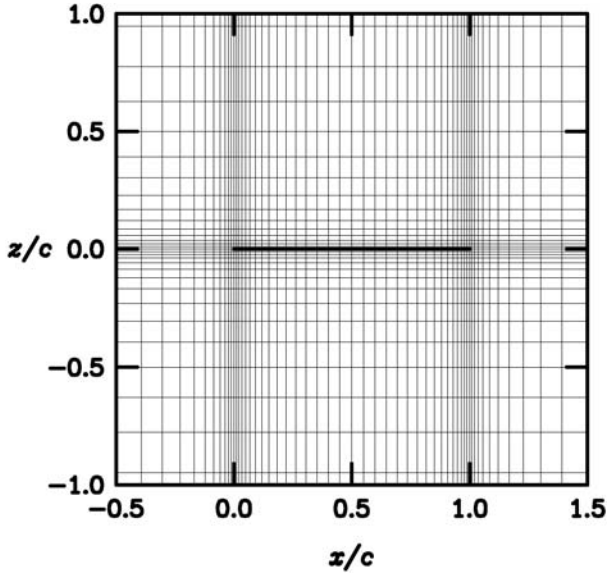

(a) Mesh 4 (97 x 65).

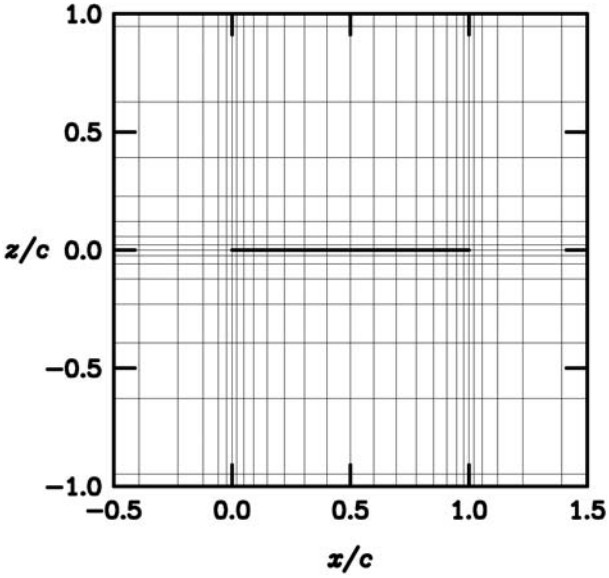

(b) Mesh 3 (49 x 33).

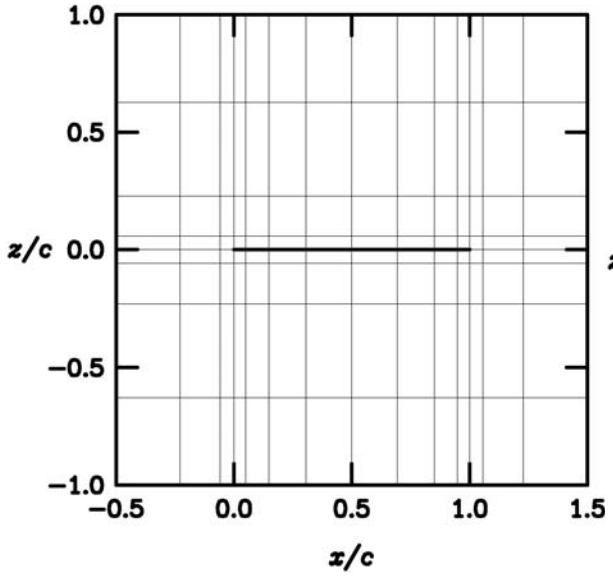

(c) Mesh 2 (25 x 17).

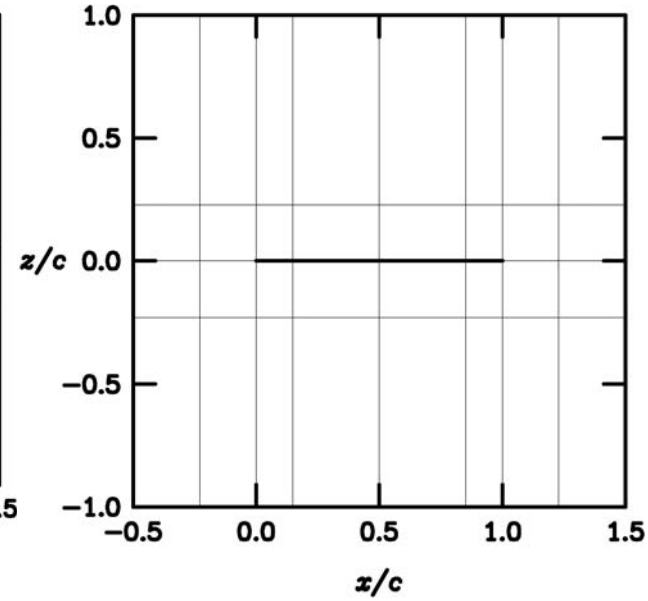

(d) Mesh 1 (13 x 9).

Figure 30 – Near field view of finite volume root sectional meshes for the F-5 fighter wing for ASP3D multigrid calculations.

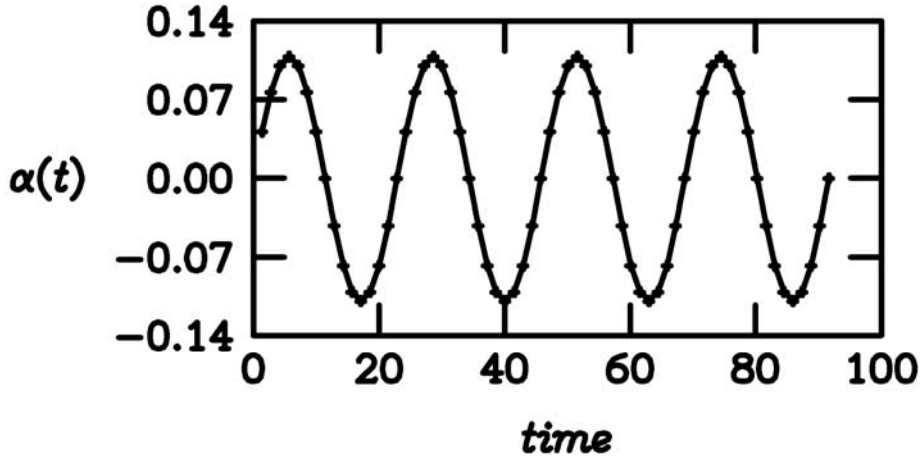

(a) Forced harmonic pitching for four cycles of motion.

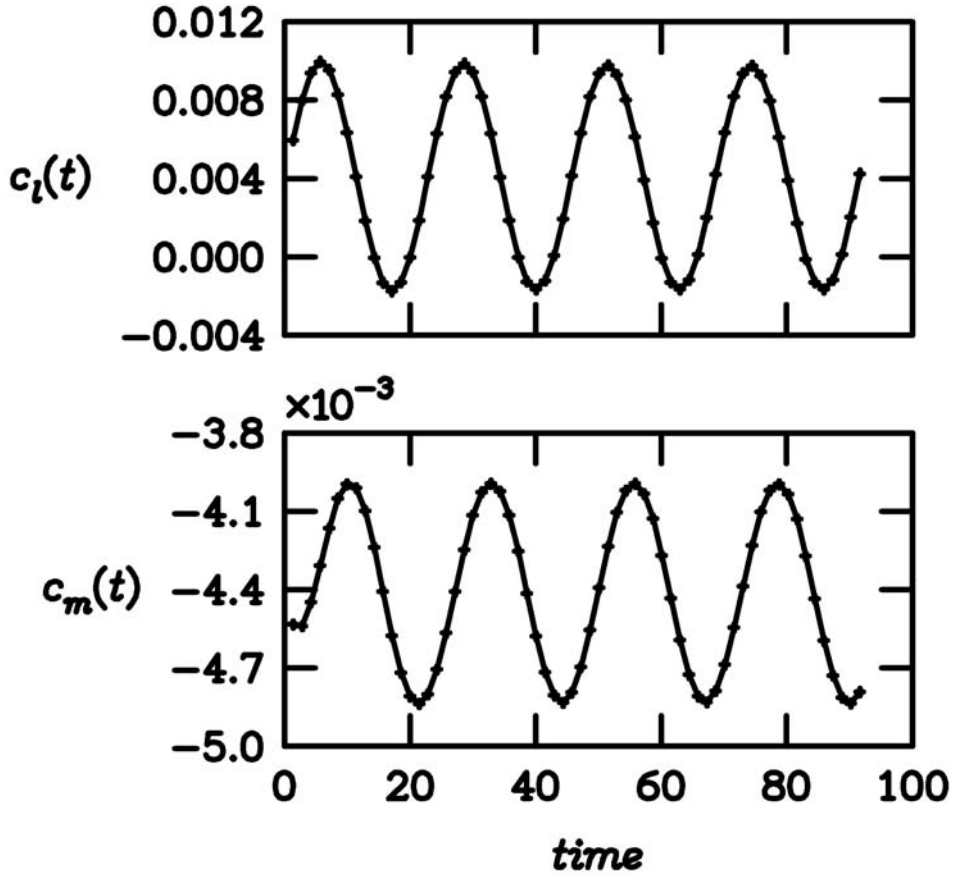

(b) Lift and moment coefficient responses.

Figure 31 – Iterative multigrid calculation using 16 steps per cycle of motion for the F-5 fighter wing pitching about the root midchord at M_∞ = 0.899, α_0 = -0.005°, α_1 = 0.109°, and k = 0.137.

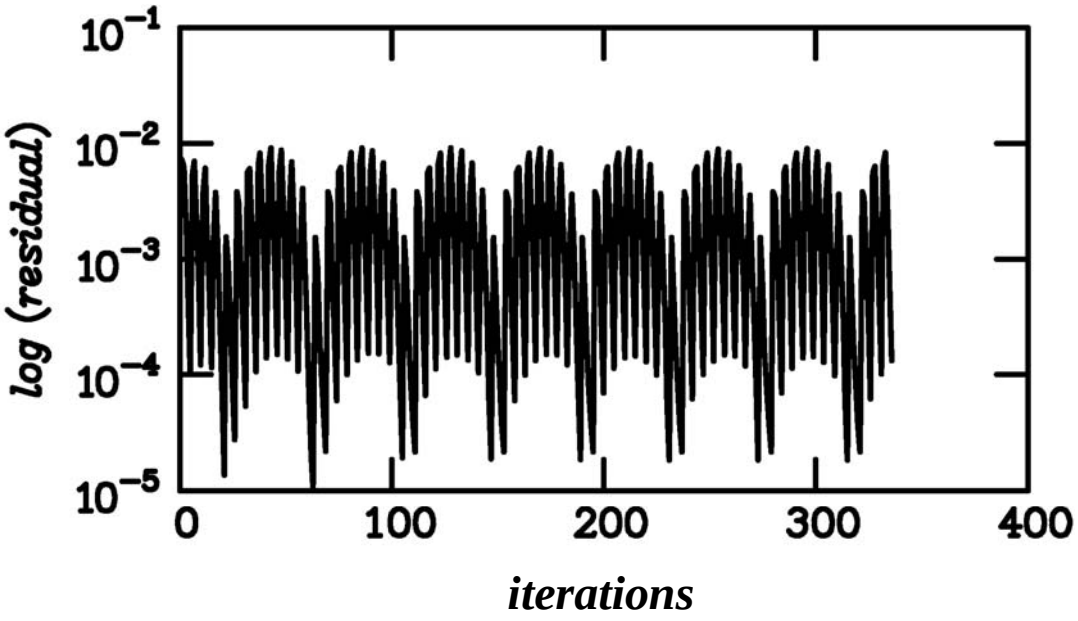

(c) Iterative multigrid residual history.

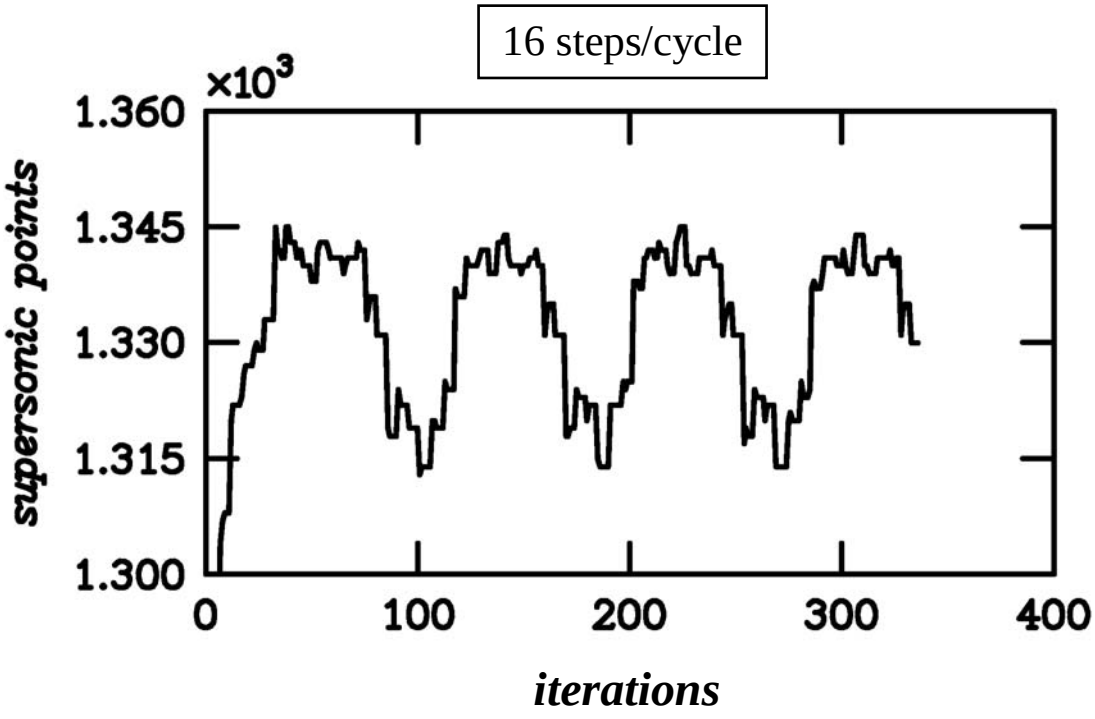

(d) Number of supersonic points.

Figure 31 – Concluded.

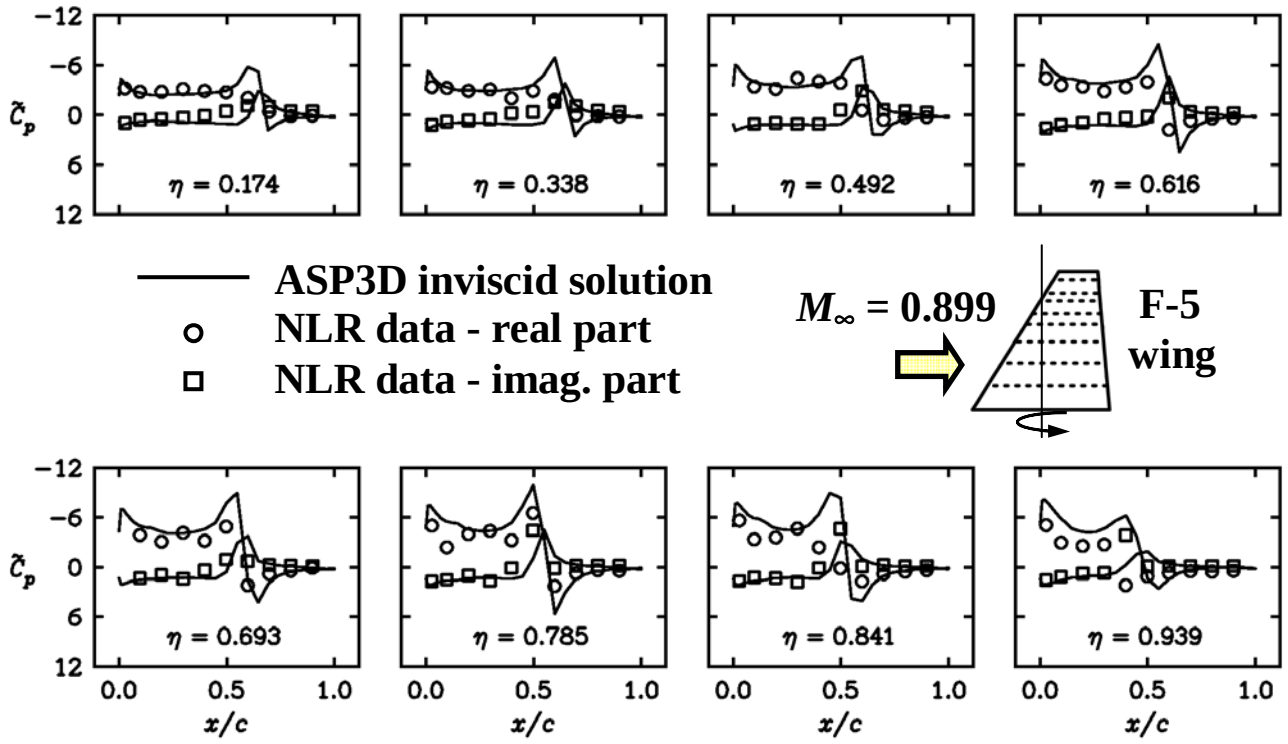

(a) Upper surface.

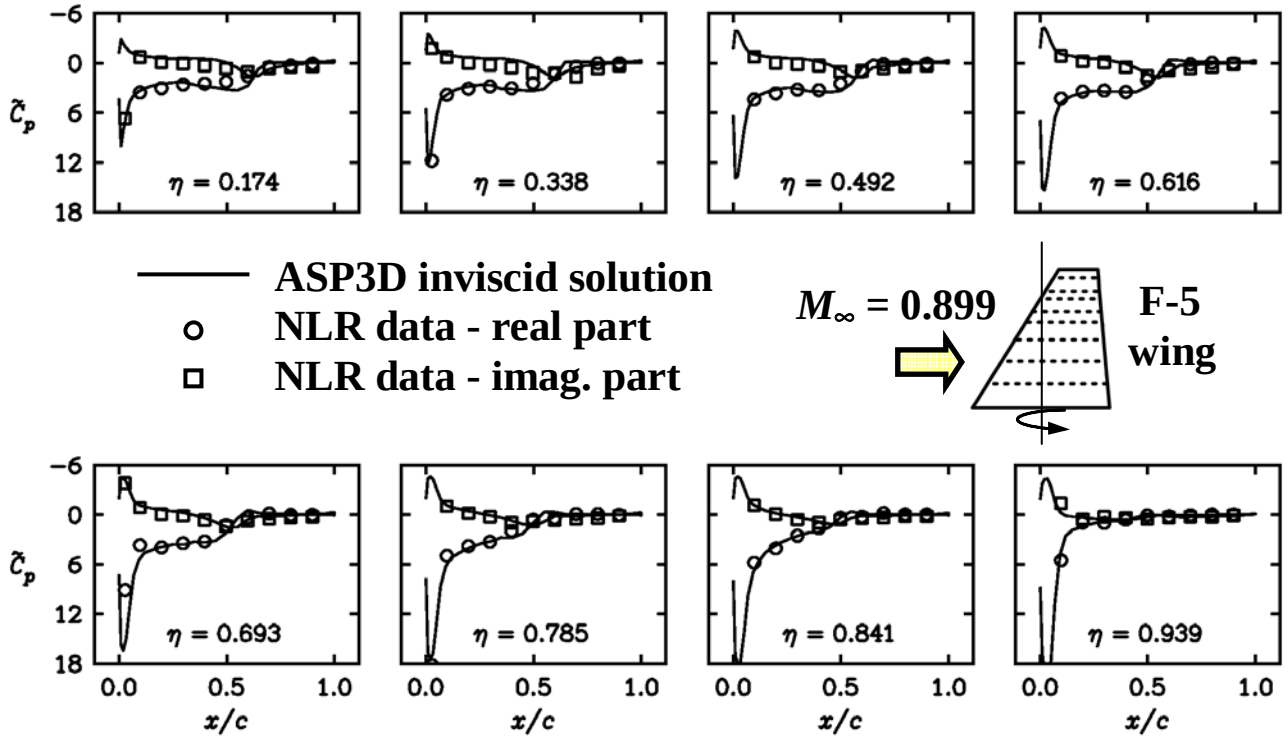

(b) Lower surface.

Figure 32 - ASP3D inviscid unsteady pressure coefficient comparisons with NLR experimental data[40] for the F-5 fighter wing pitching at M_∞ = 0.899, α_0 = -0.005°, α_1 = 0.109°, and k = 0.137.

REPORT DOCUMENTATION PAGE

Form Approved
OMB No. 0704-0188

1. REPORT DATE *(DD-MM-YYYY)*	2. REPORT TYPE	3. DATES COVERED *(From - To)*
01- 02 - 2006	Technical Memorandum	

4. TITLE AND SUBTITLE

Application of the ASP3D Computer Program to Unsteady Aerodynamic and Aeroelastic Analyses

5a. CONTRACT NUMBER

5b. GRANT NUMBER

5c. PROGRAM ELEMENT NUMBER

6. AUTHOR(S)

Batina, John T.

5d. PROJECT NUMBER

5e. TASK NUMBER

5f. WORK UNIT NUMBER

843515.02.02.29.07

7. PERFORMING ORGANIZATION NAME(S) AND ADDRESS(ES)

NASA Langley Research Center
Hampton, VA 23681-2199

8. PERFORMING ORGANIZATION REPORT NUMBER

L-19234

9. SPONSORING/MONITORING AGENCY NAME(S) AND ADDRESS(ES)

National Aeronautics and Space Administration
Washington, DC 20546-0001

10. SPONSOR/MONITOR'S ACRONYM(S)

NASA

11. SPONSOR/MONITOR'S REPORT NUMBER(S)

NASA/TM-2006-214277

12. DISTRIBUTION/AVAILABILITY STATEMENT

Unclassified - Unlimited
Subject Category 02
Availability: NASA CASI (301) 621-0390

13. SUPPLEMENTARY NOTES

An electronic version can be found at http://ntrs.nasa.gov

14. ABSTRACT

A new computer program has been developed called ASP3D (Advanced Small Perturbation - 3D), which solves the small perturbation potential flow equation in an advanced form including mass-consistent surface and trailing wake boundary conditions, and entropy, vorticity, and viscous effects. The purpose of the program is for unsteady aerodynamic and aeroelastic analyses, especially in the nonlinear transonic flight regime. The program exploits the simplicity of stationary Cartesian meshes with the movement or deformation of the configuration under consideration incorporated into the solution algorithm through a planar surface boundary condition. The paper presents unsteady aerodynamic and aeroelastic applications of ASP3D to assess the time dependent capability and demonstrate various features of the code.

15. SUBJECT TERMS

Aeroelasticity; Computational Fluid Dynamics; Unsteady Aerodynamics; Computer Programs

16. SECURITY CLASSIFICATION OF:			17. LIMITATION OF ABSTRACT	18. NUMBER OF PAGES	19a. NAME OF RESPONSIBLE PERSON
a. REPORT	b. ABSTRACT	c. THIS PAGE			STI Help Desk (email: help@sti.nasa.gov)
					19b. TELEPHONE NUMBER *(Include area code)*
U	U	U	UU	69	(301) 621-0390